

**ADAPTIVE SHADOW REMOVAL FOR VARIABLE ENVIRONMENTAL
CONDITIONS**

A Dissertation
Presented to
The Academic Faculty

By

Jay Danner

In Partial Fulfillment
of the Requirements for the Degree
Master of Electrical and Computer Engineering

Georgia Institute of Technology

May 2017

Copyright © Jay Danner 2017

ADAPTIVE SHADOW REMOVAL FOR VARIABLE ENVIRONMENTAL CONDITIONS

Approved by:

Dr. Linda Wills, Advisor
School of Electrical and Computer
Engineering
Georgia Institute of Technology

Dr. Lee Lerner, Advisor
Georgia Institute of Technology

Dr. Ayanna Howard
School of Electrical and Computer
Engineering
Georgia Institute of Technology

Dr. Patricio Vela
School of Electrical and Computer
Engineering
Georgia Institute of Technology

Dr. James Hamblen
School of Electrical and Computer
Engineering
Georgia Institute of Technology

Date Approved: April 28, 2017

ACKNOWLEDGEMENTS

I would like to express my deepest gratitude to my two advisors, Dr. Linda Wills and Dr. Lee W. Lerner, for their unwavering support and dedication to my success at Georgia Tech. Dr. Wills embodies the spirit of kindness, and I could not imagine a better mentor. I hope to carry a fraction of her patience, knowledge, and passion with me as I continue forward. Dr. Lerner has been a constant ally to my success over the years I have known him. I admire and respect both who he is and what he does, and I am honored to have had his support.

I would also like to thank Dr. Patricio Vela, Dr. Ayanna Howard, and Dr. James Hamblen for serving on my reading committee. I am grateful for your time, energy, and insight.

I cannot quantify the support my wife, Marcella, has provided. Her unflagging encouragement, warmth, and love through long nights and hard days cannot be matched. You are a blessing in my life, and I truly couldn't have done it without you.

TABLE OF CONTENTS

Acknowledgments	iii
List of Tables	vii
List of Figures	ix
Chapter 1: Introduction	1
1.1 The Problem	3
1.2 Objective and Contributions	6
Chapter 2: Approach	8
2.1 Evaluation Metrics	8
2.2 Background: Shadow Removal Methods	8
2.2.1 Chromacity	9
2.2.2 Physical	10
2.2.3 Geometry	11
2.2.4 Small-Region Texture	11
2.2.5 Large-Region Texture	11
2.3 Approach	12
Chapter 3: Methodology	14

3.1	Algorithm Assessment	14
3.1.1	Data Collection	15
3.1.2	Algorithm Selection Strategy	23
3.1.3	Selecting a Parameter of Physical Shadow Removal	30
3.2	Assessment of Environmental Properties	38
3.2.1	Previous Work - Large Region Texture Removal	38
3.2.2	Attenuation and Saturation	39
3.2.3	Non-linear Attenuation and Spectral Properties of Light	41
3.2.4	Brightness Models	45
3.2.5	Low-contrast SIFT Keypoints	48
3.3	Weak Detector Estimation - Creating a Model	52
Chapter 4:	Results	54
4.1	Correlation of Parameters	54
4.1.1	<i>coneRI*</i> and Average Attenuation	55
4.1.2	Correlation Improvements	59
4.2	Parameter Model Results	70
4.2.1	Analysis	73
Chapter 5:	Conclusion and Future Work	78
5.1	Future Work	79
5.1.1	Modeling Low-contrast SIFT Keypoints	79
5.1.2	Rapid Illumination Change Compensation	80
5.1.3	Classifying Indoor/Outdoor Scenes	80

Appendix A: Default Detection and Discrimination	82
Appendix B: Parameter Evaluation	92
Appendix C: Results	103
References	119

LIST OF TABLES

3.1 Dataset information.	16
4.1 Datasets and their α_{dB} correlations to $coneRI^*$	55
4.2 Datasets and their $\alpha_{\% \Delta}$ correlations to $coneRI^*$	55
4.3 Datasets and their <i>SIFT</i> correlations to $coneRI^*$	58
4.4 Correlation shifts ($\rho_{\% \Delta}$) when $SIFT_{fg/bg}$ is multiplied against observed attenuation $\alpha_{\% \Delta}$	61
4.5 Datasets and their correlations to $coneRI^*$ (α_{dB}) against Brightness models. Outdoor (top) and Indoor (bottom) scenes are grouped appropriately. . .	64
4.6 Red-green bias for each dataset. β^{RG} represents the average of the β_f^{RG} for each frame in a dataset. Outdoor (top) and Indoor (bottom) scenes are grouped together.	66
4.7 Datasets and their correlations to $coneRI^*$ ($\alpha_{\% \Delta}$) against Brightness models. Outdoor (top) and Indoor (bottom) scenes are grouped appropriately. . .	67
4.8 Average detection (η) calculated from the adapted $coneRI'$ (left). η is compared against original naive detection ($coneRI = 0.3$). The difference (right) is represented as a percentage.	73
4.9 Average discrimination (ξ) calculated from the adapted $coneRI'$ (left). ξ is compared against original naive discrimination ($coneRI = 0.3$). The difference (right) is represented as a percentage.	76
A.1 PETS1	83
A.2 PETS2	84

A.3 aton_highway1	85
A.4 aton_highway3	86
A.5 aton_room	87
A.6 aton_campus (pt. 1 of 2)	88
A.7 aton_campus (pt. 2 of 2)	89
A.8 aton_hallway	90
A.9 aton_lab	91
C.1 PETS1	110
C.2 PETS2	110
C.3 aton_highway1	111
C.4 aton_highway3	111
C.5 aton_room	112
C.6 aton_campus	113
C.7 aton_hallway	114
C.8 aton_lab	114

LIST OF FIGURES

1.1	The need for shadow removal: (a) Original frame from the aton_room dataset [5]. (b) Result of foreground extraction, with shadows incorrectly being detected as moving objects rather than as background. (c) Research goal: proper segmentation into shadow regions and true foreground. (d) Proper identification of foreground with the removal of shadows.	2
1.2	<i>coneRI</i> set to 0.2. (a) Detection: 87.8, Discrimination: 59.84. (b) Detection: 99.9, Discrimination: 32.2	4
1.3	<i>coneRI</i> shifted from ‘0.2’ to ‘0.68.’ (a) Detection: 10.59, Discrimination: 87.97. (b) Detection: 84.9, Discrimination: 85.4. No parameter value provides consistent accuracy across datasets.	5
1.4	<i>gWeight</i> shifted from ’70’ to ’0.’ (a) Detection: 79.05, Discrimination: 86.74. (b) Detection: 71.13, Discrimination: 90.21	5
3.1	PETS2 experiencing both high illumination (a) and low illumination (b) (due to cloud cover).	16
3.2	Datasets collected for ATON: (a) aton_highway1, (b) aton_lab, and (c) aton_hallway.	17
3.3	An example SimpleINI file. Parameters taken from this file are used to adjust values in real-time.	18
3.4	GUI tools created using OpenCV, displaying Geometry shadow removal.	19
3.5	The GUI takes user input through sliders, updates values in a .ini file, which are used to produce a new output image indicating shadow versus foreground pixels with the corresponding detection and discrimination rates. The GUI then visualizes this output.	19
3.6	For one frame, a parameter is systematically iterated to provide detection/discrimination results for each possible parameter value.	21

3.7 (a) Detection (blue) and Discrimination (orange) rates are charted against the iterated parameter value pr (x-axis). For each parameter value, detection and discrimination are summed to produce a removal efficacy score $\Xi(pr)$. The global maximum of this value is the optimal parameter value (pr^*).	22
3.8 Shadow detection (η)(orange) for each algorithm, run on the PETS1 dataset during an illumination change. Overall brightness of a scene is shown in gray.	24
3.9 (a) depicts a sensitive parameter, while (b) represents a typical parameter.	25
3.10 (a) and (b) showcase erratic shadow detection run on the dataset aton_campus, which experiences no significant illumination change.	27
3.11 (a) Run on aton_hallway, LRT shows consistent shadow removal accuracy, with occasional dips. (b) Run on aton_campus, LRT performs erratically.	28
3.12 The LRT parameter $avgAttenThresh$ is highly sensitive, demonstrating a narrow range for which LRT removal accuracy is affected. LRT's removal accuracy response is shown, using the aton_highway1 dataset.	29
3.13 Chromacity and Physical shadow removal demonstrate similar shadow detection results run on aton_hallway.	29
3.14 Detection (blue) and discrimination (orange) rates are calculated as the value of $coneR1$ is varied from [0.0 .. 1.0]. Full results found in appendices.	33
3.15 Example score (Ξ) of a frame for each dataset. Full results found in appendices.	34
3.16 Parameter value responses for $coneR2$ for three datasets (aton_campus, aton_highway1, and aton_room). Full results found in appendices.	36
3.17 (a) Shadow removal reponse (detection and discrimination) for $coneAngle$, for aton_highway1. (b) Shadow removal score for aton_highway1. $coneAngle^*$ is the maximum of the score.	37
3.18 (a) Shadow pixel SD is attenuated linearly from background pixel BG . (b) SD is attenuated non-linearly.	41

3.19	Outdoor datasets demonstrate consistently greater deviations in the red and green channels. During illumination changes (evident in PETS1 and PETS2), the red and green channels shift disproportionate to that of the blue channel, indicating scattered blue light is a primary component of the shadows' spectral illuminant ratio.	43
3.20	Indoor datasets demonstrate closer grouping of each channel's color shift. aton_hallway behaves most erratically of the indoor datasets. This is due to color-bleed from nearby objects, making aton_hallway the most diverse spectral ratio of the indoor sets. aton_lab behaves linearly, as expected. . . .	44
3.21	The limited structural effects of cast shadows in the saturation channel (d). .	49
3.22	Detecting low-contrast SIFT keypoints in the saturation channel more effectively captures structural changes than in the intensity channel, due to cast shadows.	51
3.23	Regression performed on RGB shift found per frame, vs. required magnitude shift to optimal.	53
4.1	Correlation of α_{dB} (orange) and $coneRI^*$ (blue) is observed across all datasets. Three are shown here. (All results can be found in the appendix)	56
4.2	Likewise, correlation of $\alpha\%_\Delta$ (orange) and $coneRI^*$ (blue) is observed across all datasets with three shown here. (All results can be found in the appendix)	57
4.3	$SIFT_{fg/bg}$ multiplication's effect on correlation for the dataset aton_highway1. The observed attenuation $\alpha\%_\Delta$ (orange), is multiplied by the calculated $SIFT_{fg/bg}$ on a per frame basis. The resultant (α_{SIFT}), shown in green, represents a closer fit to $coneRI^*$ (blue).	60
4.4	Original correlations, $\rho\%_\Delta$, (orange) are plotted against newly calculated correlations ρ_{SIFT} (green).	60
4.5	Example contrasting correlation improvements of the HSP model (green) against HSV (orange) and $coneRI^*$ (blue).	62
4.6	Datasets and their correlations (y-axis)to $coneRI^*$ (α_{dB}) against Brightness models (x-axis).	63
4.7	Outdoor datasets (a) share a common response to varying brightness models. In contrast, indoor datasets (b) share a insensitivity to varying brightness models	65

4.8	aton_highway1's response to various brightness models behaves opposite to other outdoor datasets.	67
4.9	Datasets and their correlations (y-axis) to $coneRI^*$ ($\alpha_{\%}\Delta$) against Brightness models (x-axis).	68
4.10	(a) Outdoor datasets. (b) Indoor datasets.	69
4.11	For each brightness model, Δ RGB is plotted against $shift_{req.}$. The general model for each brightness calculation is formed through a best-fit logarithm.	71
4.12	Adaptively tuned $coneRI'$ parameter (green) charted against $coneRI^*$ (blue) and average attenuation ($\alpha_{\%}\Delta$) (orange). All results can be found in the appendix.	72
4.13	Average detection (a) and average discrimination (b) calculated using the adaptive parameter model, for each dataset.	74
4.14	Qualitative shadow removal improvement. (a - c) feature the aton_campus dataset, and (d - f) feature the aton_room datasets.	75
4.15	For PETS2, the adapted parameter $coneRI'$ (green) is erroneously shifted downwards. The originally observed attenuation ($\alpha_{\%}\Delta$) is shown in orange.	77
B.1	Detection (blue) and discrimination (orange) rates are calculated as the value of $coneR2$ is varied from [0.0 .. 1.0]. (pt. 1 of 4)	93
B.2	Detection (blue) and discrimination (orange) rates are calculated as the value of $coneR2$ is varied from [0.0 .. 1.0]. (pt. 2 of 4)	94
B.3	Detection (blue) and discrimination (orange) rates are calculated as the value of $coneR2$ is varied from [0.0 .. 1.0]. (pt. 3 of 4)	95
B.4	Detection (blue) and discrimination (orange) rates are calculated as the value of $coneR2$ is varied from [0.0 .. 1.0]. (pt. 4 of 4)	96
B.5	Detection (blue) and discrimination (orange) rates are calculated as the value of $coneAngle$ is varied from [0.0 .. 1.0]. (pt. 1 of 4)	97
B.6	Detection (blue) and discrimination (orange) rates are calculated as the value of $coneAngle$ is varied from [0.0 .. 1.0]. (pt. 2 of 4)	98
B.7	Detection (blue) and discrimination (orange) rates are calculated as the value of $coneAngle$ is varied from [0.0 .. 1.0]. (pt. 3 of 4)	99

B.8	Detection (blue) and discrimination (orange) rates are calculated as the value of <i>coneAngle</i> is varied from [0.0 .. 1.0]. (pt. 4 of 4)	100
B.9	Attenuation (α_{dB} model) plotted against <i>coneRI*</i> . (pt. 1 of 2)	101
B.10	Attenuation (α_{dB} model) plotted against <i>coneRI*</i> . (pt. 2 of 2)	102
C.1	Attenuation ($\alpha_{\% \Delta}$ model) plotted against <i>coneRI*</i> . (pt. 1 of 2)	104
C.2	Attenuation ($\alpha_{\% \Delta}$ model) plotted against <i>coneRI*</i> . (pt. 2 of 2)	105
C.3	α_{SIFT} (green) is plotted against <i>coneRI*</i> and $\alpha_{\% \Delta}$. (pt. 1 of 2)	106
C.4	<i>coneRI'</i> (green) is plotted against <i>coneRI*</i> and $\alpha_{\% \Delta}$. (pt. 2 of 2)	107
C.5	α_{SIFT} (green) is plotted against <i>coneRI*</i> and $\alpha_{\% \Delta}$. (pt. 1 of 2)	108
C.6	<i>coneRI'</i> (green) is plotted against <i>coneRI*</i> and $\alpha_{\% \Delta}$. (pt. 2 of 2)	109

SUMMARY

The motivation for this research is to provide a quantitative model for improving shadow detection in arbitrary environments. Many computer vision applications extract foreground pixels to capture moving objects in a scene. However, since shadows share movement patterns with foreground objects (and have a similar magnitude of intensity change compared to a background model), they tend to be extracted with the desired object pixels. Shadows generally contribute to inaccurate object classifications and impede proper tracking of foreground objects. Contemporary shadow removal algorithms have made great strides in discriminating between object pixels and shadow pixels, but lack scene-independence. In order to perform optimally, these leading methods require assumptions to be made about key factors of a scene, including illumination constancy, color content, and shadow intensity. As a result, no leading shadow removal method is robust enough to compensate for environmental change over time, nor are they suitable for deployment into a particular environment without a priori tuning of parameters.

This research evaluates popular shadow removal methods, extracts corresponding algorithmic parameters that affect shadow removal, correlates these parameters with salient environmental aspects, and finally leverages this correlation to improve shadow removal efficacy across diverse environments. Data collection and validation were performed using a collection of widely-used computer vision datasets. Parameters, both algorithmic and environmental in nature, are identified, correlated, and evaluated using analytic tools. Using the average attenuation of dark foreground pixels, an adaptive model improves shadow detection by up to 10% and improves shadow-object discrimination by up to 28%. Additional indirect environmental factors are found to increase the effectiveness of this attenuation model. Brightness calculation methods are shown to improve attenuation correlation by 7% to 20%. Identifying low-contrast feature keypoints in a scene is also found to improve attenuation-correlation in some environments by up to 12%.

CHAPTER 1

INTRODUCTION

The need for accurate video analytics has emerged in many application areas, including surveillance, transportation management, and smart-city sensing infrastructure. Many of these applications, e.g., pedestrian and traffic counting [1], perform classification and analysis on moving objects. In order to detect and extract moving objects in an environment, foreground pixels are differentiated from those of the background through the use of statistical techniques, including Mixture of Gaussians, and Multi-Modal Mean [2, 3]. These strategies establish a model of the background of a scene, which changes gradually over time. This background model is then compared directly to a frame. By finding the difference between an image frame and its background model, a mask containing the foreground pixels is created. Foreground pixels are then grouped together and segmented as a moving object, which is analyzed according to the needs of the application.

Applications that analyze moving objects rely on the accuracy of the foreground extraction of foreground pixels. These applications are disadvantaged by the fact that shadows are often mischaracterized as foreground objects, and are included as part of a moving object. This is often because shadows possess similar movement patterns and brightness compared to non-shadow foreground objects [4]. Figure 1.1 illustrates the effect shadows have on the segmentation of foreground objects.

The inclusion of shadows in foreground objects may hamper detection and tracking in several ways. Prominent issues, noted by Sanin et al. [6], include the distortion of an object's appearance model (required to properly track an object), and the erroneous joining of multiple objects into one labeled connected-component. Additional details regarding a shadow's effect on tracking can be found in [4, 7]. The removal of shadows from foreground objects is thus a vital step in accurately segmenting moving foreground objects.

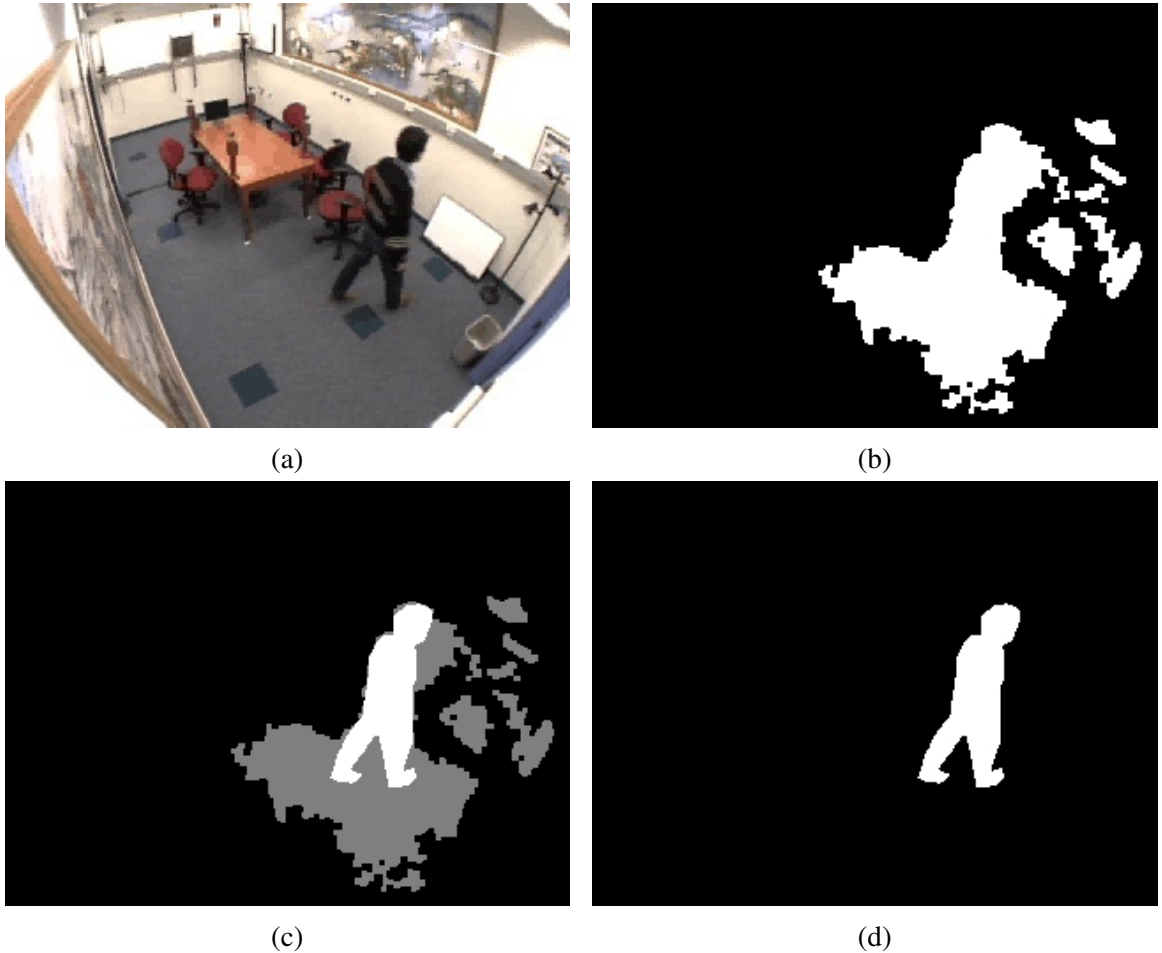
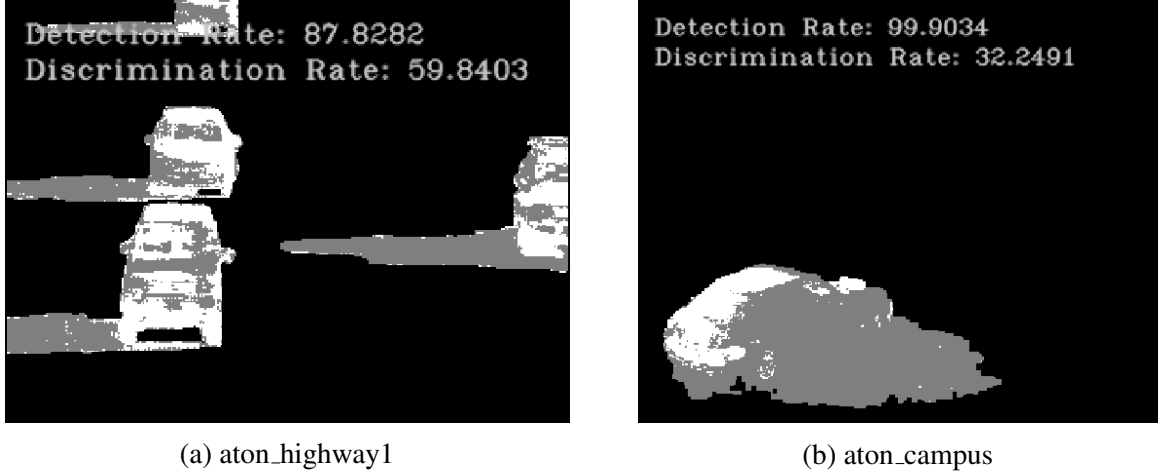


Figure 1.1: The need for shadow removal: (a) Original frame from the aton_room dataset [5]. (b) Result of foreground extraction, with shadows incorrectly being detected as moving objects rather than as background. (c) Research goal: proper segmentation into shadow regions and true foreground. (d) Proper identification of foreground with the removal of shadows.

Classifying shadow pixels within moving foreground objects has been approached in numerous ways, including color-based attenuation models [8, 9, 10, 11, 12], geometric projective models [13, 14, 15, 16, 17], and texture-matching models [18, 19, 20, 21, 22, 23]. Machine-learning has also been employed to attempt to learn the appearance of cast shadows in an unsupervised manner [24, 25, 26, 27]. A taxonomy of shadow removal methods produced by Prati et al. summarizes and evaluates four contemporary method classes: Statistical Nonparametric, Statistical Parametric, Deterministic Nonmodel-based and Deterministic Nonmodel-based [28]. The study concluded that the simpler methods were more suited for general practice, but “to detect shadows efficiently in one specific environment, [adding] more assumptions yields better results.” A second algorithm survey conducted by Sanin et al. in [6] evaluated more modern methods (catalogued as Chromacity, Geometry, Physical, Small Region Texture, and their own contribution, Large Region Texture) on the same datasets as above, yielding similar results concerning the generalization of shadow removal to an arbitrary scene. Mitra et al. provides a survey of threshold selection strategies for identifying shadows in moving foreground objects [7].

1.1 The Problem

These surveys indicate that existing shadow removal algorithms fail to optimally adapt to varying environmental properties; these methods quantifiably benefit from assumptions made about key factors of a scene, including illumination constancy, color content, and shadow intensity. In order to facilitate optimization, shadow removal methods possess algorithm parameters that are manually tuned to an environment. The reliance on environmental assumptions affects shadow removal in two ways: firstly, shadow removal performs suboptimally when deployed in an arbitrary environment, and secondly, even when manually calibrated, shadow removal fails to adapt to environmental parameters that change over time. From an application context, a surveillance system that monitors a sun-lit environment throughout an entire day will possess a wide range of shadow qualities when



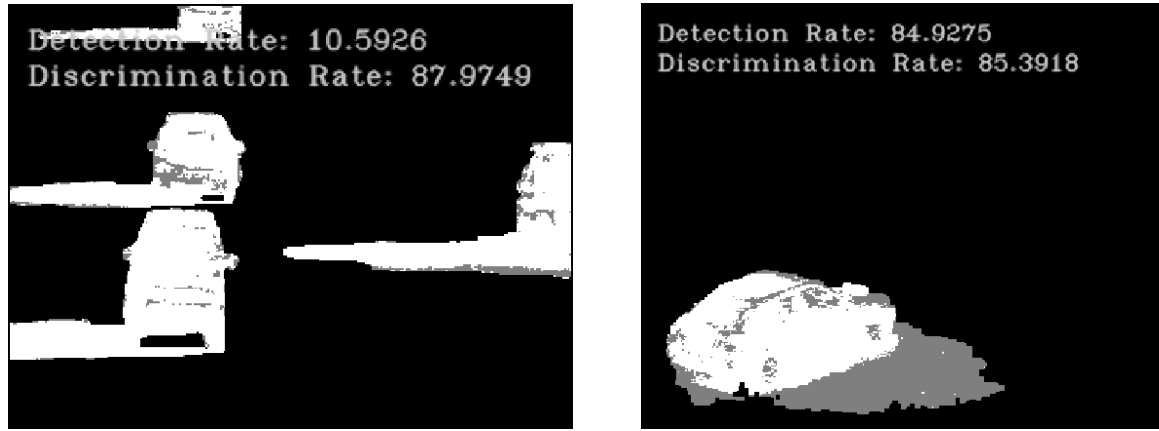
(a) aton_highway1

(b) aton_campus

Figure 1.2: *coneRI* set to 0.2. (a) Detection: 87.8, Discrimination: 59.84. (b) Detection: 99.9, Discrimination: 32.2

comparing shadows cast at dawn to shadows cast in the evening. Shadows cast in the same location may vary in darkness, size, orientation, and shape depending on the time of day. Therefore shadow removal must adapt not only to diverse environments, but continually adapt as environmental properties vary over time.

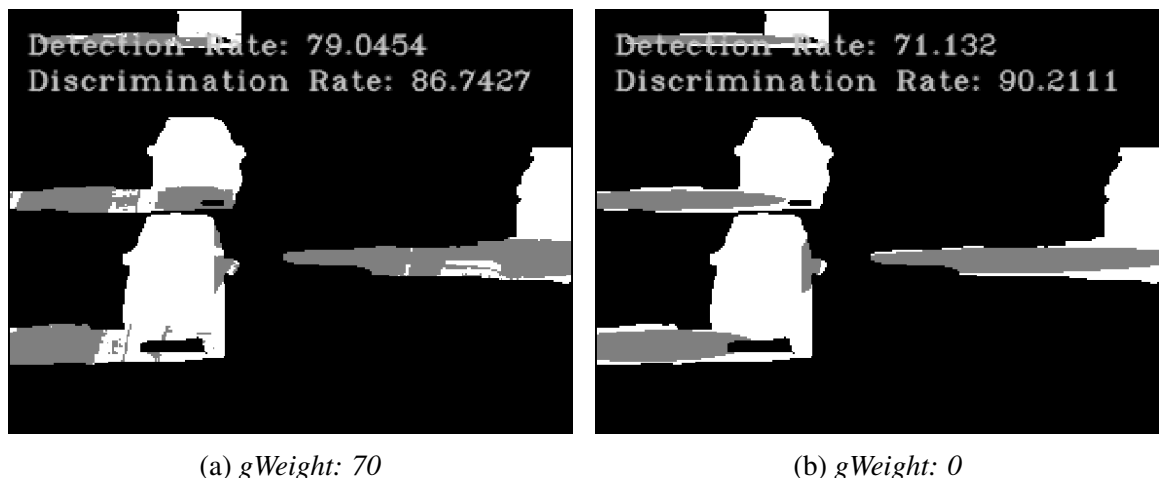
We quantitatively demonstrate several cases that indicate the need for adaptation. Shadow removal is judged by its detection rate and its discrimination rate, further detailed in section 2.1. Detection rate indicates the number of shadow pixels correctly identified, while discrimination rate indicates the number of foreground object pixels that are correctly identified. Figure 1.2 modifies a parameter belonging to Physical shadow removal, which controls the chromacity range in which a shadow can lie. The parameter (*coneRI*) causes Physical shadow removal to perform optimally in the aton_highway1 frame at a value of 0.2. Similarly, the same algorithm performs poorly in the included dataset aton_campus with the same parameter value. However, if *coneRI* is modified from 0.2 to 0.68, aton_highway1 experiences a 77% loss of detection, while aton_campus gains 53% discrimination in exchange for a 15% loss of detection (1.3). Geometry shadow removal was found to also showcase different results on the same scene, but with differing parameters (Figure 1.4).



(a) aton_highway1

(b) aton_campus

Figure 1.3: *coneR1* shifted from ‘0.2’ to ‘0.68.’ (a) Detection: 10.59, Discrimination: 87.97. (b) Detection: 84.9, Discrimination: 85.4. No parameter value provides consistent accuracy across datasets.



(a) *gWeight*: 70

(b) *gWeight*: 0

Figure 1.4: *gWeight* shifted from ’70’ to ’0.’ (a) Detection: 79.05, Discrimination: 86.74. (b) Detection: 71.13, Discrimination: 90.21

1.2 Objective and Contributions

Our research seeks to establish an understanding of environmental properties that affect shadow removal, and use that understanding to optimize shadow removal in an arbitrary environment. This is achieved by automatically calibrating an algorithm’s parameters based on observed environmental properties. Furthermore, we seek to create an understanding of how these environmental properties change over time, in order to continuously adapt shadow removal algorithms. These objectives require the creation of an adaptive model that automatically configures a shadow removal method to optimally perform given the observed environmental properties.

Our research makes the following contributions. We perform a qualitative assessment of each algorithm’s performance in various environments. We construct and utilize an interactive framework for evaluating the sensitivity of an algorithm with respect to its mutable parameters. We identify and quantify observed environmental properties, and correlate them to sensitive algorithm parameters. Finally, we demonstrate the construction of an adaptive model, capable of leveraging correlated environmental properties to automatically tune an algorithm’s parameters. The demonstration is completed by constructing a proof-of-concept model for Physical shadow removal.

Our proof-of-concept adaptive model draws upon the correlation between brightness attenuation in shadow regions and one of the Physical algorithm’s parameters, *coneR1*. It improves shadow detection by up to 10% and shadow discrimination by up to 28% on a range of standard datasets from ATON and PETS [5, 29]. Additional indirect environmental factors are found to modify the effectiveness of the adaptive model. Various brightness calculation methods are shown to influence attenuation correlation by 7% to 20%. A study of low-contrast feature keypoints in a scene was shown to improve attenuation-correlation by up to 12% in some environments.

The outline of this thesis is as follows. In Chapter 2, we detail the shadow removal

algorithms utilized in this study, and outline the steps taken to produce an adaptive model. Chapter 3 assesses the shadow removal algorithms for their performance in diverse environments, as well as their sensitivity to parametric change. These assessments culminate in the construction of a proof-of-concept adaptive model for Physical shadow removal, using its *coneR1* parameter. Chapter 3 also explores indirect environmental properties and their potential impacts on the performance of the adaptive model. Chapter 4 quantifies and discusses the results of the adaptive model, and the indirect environmental properties' effects on the model. Chapter 5 summarizes conclusions and future work.

CHAPTER 2

APPROACH

This chapter details evaluation metrics, provides background on the surveyed shadow removal algorithms, and outlines our research methodology. In section 2.1, we quantify the metrics used to evaluate the accuracy of shadow removal. Section 2.2 provides background on the shadow removal algorithms examined in this study. Finally, our research approach is outlined in section 2.3.

2.1 Evaluation Metrics

The efficacy of a shadow removal algorithm on a given frame is evaluated with the popular metrics *Detection* (η) and *Discrimination* (ξ) (Eqn. 2.1, Eqn. 2.2) [28]. These measure how many shadow pixels are correctly identified, and how many foreground object pixels are correctly preserved, respectively. The metrics are calculated using true positives (TP) and false negatives (FN) of both foreground pixels and shadow pixels. Subscripts signify identifications on shadow pixels (S) or foreground pixels (F).

$$\eta = \frac{TP_S}{TP_S + FN_S} \quad (2.1)$$

$$\xi = \frac{TP_F}{TP_F + FN_F} \quad (2.2)$$

2.2 Background: Shadow Removal Methods

We select five popular shadow removal algorithms for this study, named Chromacity, Physical, Geometry, Small-Region Texture, and Large-Region Texture. These shadow removal methods use differing techniques for identifying foreground shadow pixels. These tech-

niques are color information (Chromacity), brightness attenuation (Physical), shadow shape (Geometry), and texture information (Small-Region Texture, Large-Region Texture). We used standardized implementations of the shadow removal methods, licensed under GPL v3+ and written in C++ [30].

2.2.1 Chromacity

Chromacity, or *hue*, represents the base color of a pixel, and is separable from brightness and saturation. Chromacity-based shadow removal methods maintain that a pixel, when covered by a shadow, loses luminosity (or brightness), while retaining its chromacity. This assumption is referred to as color constancy, or linear attenuation. This study implements one such algorithm from Cucchiara et al. [8], implemented using the Hue-Saturation-Value (HSV) color representation.

Cucchiara et al. observe a shadowed pixel in the foreground (fg_p) retains its hue when compared to the corresponding background pixel (bg_p), while losing saturation and intensity (value). In order to be considered a shadow, the hue, saturation, and value of fg_p must fall within the pre-determined thresholds τ_H , τ_S , and $[\beta_1, \beta_2]$ (Eqn. 2.3, 2.4, 2.5).

$$|fg_p(H) - bg_p(H)| \leq \tau_H \quad (2.3)$$

$$fg_p(S) - bg_p(S) \leq \tau_S \quad (2.4)$$

$$\beta_1 \leq \frac{fg_p(V)}{bg_p(V)} \leq \beta_2 \quad (2.5)$$

The thresholds are optimized for the environment of the algorithm's intended application. Due to its reliance on curated thresholds, Chromacity shadow removal is sensitive to strong illumination changes. Furthermore, the assumed linear attenuation model performs worse with dark shadows.

2.2.2 Physical

For a shadow pixel to attenuate linearly, the light source casting the shadow must consist of primarily white light. Many environments experience multiple light sources, whether they are the sun, surface reflections, or blue light refracted from the sky. The presence of non-white light sources causes non-linear attenuation from a foreground shadow pixel to its background pixel.

This study uses an implementation of Cheng et al.'s Physical shadow removal, which attempts to learn the attenuation model of a shadow using a Gaussian Mixture Model (GMM) [27]. Three features are used to learn the attenuation model of a pixel (p): illumination attenuation (α_p), red-green direction (θ_p), and blue direction (ϕ_p). θ_p and ϕ_p are spherical coordinates, derived from the representation of the pixel p as a vector \vec{v}_p in the RGB coordinate plane. \vec{bg}_p represents the pixel vector associated with the corresponding background model. Eqn. 2.6, Eqn. 2.7, and Eqn. 2.8 describe the calculation of these features.

$$\alpha_p = \frac{||\vec{v}_p||}{||\vec{bg}_p||} \quad (2.6)$$

$$\theta_p = \arctan\left(\frac{\vec{v}_p(G)}{\vec{v}_p(R)}\right) \quad (2.7)$$

$$\phi_p = \arccos\left(\frac{\vec{v}_p(B)}{||\vec{v}_p||}\right) \quad (2.8)$$

Physical shadow removal first uses a weak detector to identify candidate shadow pixels, calculates the appropriate color features, and uses them to update the GMM. The GMM learns the attenuation model of a shadow over time, and is used to discriminate between foreground object pixels and shadow pixels.

2.2.3 Geometry

Widely-used Geometry-based shadow removal methods attempt to identify shadow regions in a foreground object using projective geometry [13, 14, 15, 16, 17]. The implementation evaluated in this study, proposed by Hsieh et al. [13], characterizes the geometric moments of foreground blobs in an attempt to identify the vertical peak and center of gravity of the objects. Using this information, the foreground object is split into an object region and a shadow region.

Geometric removal methods often require that a shadow and an object retain a clear orientation in regard to one another. Geometric removal is best deployed in environments with distinct, upright objects with a strong directional source of light.

2.2.4 Small-Region Texture

Texture-based shadow removal attempts to match shadow pixels based on the underlying background texture, i.e., structural patterns observed in both the background model and the foreground. If similar structural patterns are observed, it is concluded that the foreground region does not occlude the background, and is therefore more likely to be a cast shadow.

Small-Region Texture (SRT) shadow removal, proposed by Leone et al. [20], utilizes a set of Gabor functions with various bandwidths, orientations, and phases. A set of candidate shadow pixels, determined by a weak detector similar to that of Physical removal, is projected onto the set of Gabor filters. After analyzing both foreground and background, the texture correlation is found by computing the Euclidean distance.

2.2.5 Large-Region Texture

Large-Region Texture (LRT) shadow removal recognizes that the small regions analyzed using SRT may fail to contain enough structural information to match foreground to background. LRT takes advantage of Chromacity removal to produce regions of probable shadow candidates, and correlates the gradient information of both the foreground and

background regions. LRT removal proves most effective in environments characterized by strong textural features and large contiguous shadow regions.

2.3 Approach

Our approach is divided into two components: algorithm assessment in the context of shadow removal in diverse environments, and the creation of the adaptive model for Physical shadow removal.

We first assess the previously catalogued algorithms (Chromacity, Physical, Geometry, SRT, and LRT removal) for sensitivity to both environmental and parametric change. We perform the analysis by applying each shadow removal method to each environment represented by our datasets. The detection and discrimination rates of each method’s shadow removal are plotted over time. Each method is judged based on its (detection/discrimination) response to the different environments of the datasets, and its response over time within each dataset.

We then perform a similar sensitivity analysis upon the parameters utilized by the algorithms. An algorithm is first explored through the use of interactive graphical tools, which enable exploration of a parameter’s effect upon an algorithm. Parameter value ranges are also methodically swept to reveal the sensitivity of an algorithm’s detection and discrimination rates to a give parameter’s value.

From the sensitivity assessments, we demonstrate the creation of an adaptive model for Physical shadow removal’s *coneR1* parameter. We create this adaptive model as a proof-of-concept, demonstrating the capability of correlating environmental properties to an algorithm’s parameter, and automatically calibrating the algorithm for improved shadow removal. The adaptive model is created in five steps:

1. Determine optimal value of parameter (per frame): In accordance with our sensitivity analysis, each frame of a dataset has an optimal value for the selected parameter,

i.e., there is an optimal value for which shadow removal is maximized. The process for extracting these optimal values is detailed in section 3.1.1.

2. Quantify environmental properties: Observed environmental properties are the most influential factor for creating an adaptive model. Section 3.2 details identifying and quantifying salient environmental properties.
3. Correlate optimal parameter value and environmental properties: For each dataset, optimal parameter values and environmental properties are recorded for each frame. By analyzing the correlation between the two sets, we receive a quantitative understanding of how well that environmental parameter would serve as the basis for an adaptive model. For example, if our optimal parameter value increases by $x\%$ from frame 1 to frame 2, and our environmental property also increases by $x\%$ from frame 1 to frame 2, that environmental property may be used to predict an appropriate value of our algorithm parameter. Consistent correlations are sought across each dataset to eliminate false positives.
4. Improve/evaluate correlations: Many environmental properties exist that may not display direct correlation with a parameter's optimal value. We instead utilize these indirect properties as modulators to improve correlation observed with a primary environmental property. Multiple contributing environmental properties are combined to improve correlation and thereby shadow removal. Indirect properties are evaluated in sections 3.2.3, 3.2.4, and 3.2.5.
5. Create general model for selected parameter: Incorporating direct and indirect correlative environmental properties, we construct an adaptive model capable of calculating a new value for the algorithm parameter that improves shadow removal. This model is independent of dataset, and is calculated per frame, rather than applied to every frame in a dataset. Methodology for building this model is found in section 3.3.

CHAPTER 3

METHODOLOGY

This chapter contains the research methodology employed while implementing a proof-of-concept of an adaptive shadow removal model. Our methodology is divided into two components: algorithm assessment in the context of shadow removal in diverse environments, and the creation of the adaptive model for Physical shadow removal, one of the previously assessed algorithms.

We first assess the previously catalogued algorithms (Chromacity, Physical, Geometry, SRT, and LRT removal) for sensitivity to both environmental and parametric change. We then perform a similar sensitivity analysis upon the parameters utilized by the algorithms. These assessments are performed qualitatively to determine the feasibility of an adaptive model being created for each algorithm.

From the sensitivity assessments, we demonstrate the creation of an adaptive model for physical shadow removal's *coneR1* parameter, which bounds the brightness deviation used to distinguish shadow pixels from foreground. We consider various environmental properties and evaluate their correlations to the selected algorithm parameter. Potential indirect correlative factors are detailed in sections 3.2.4 and 3.2.5. Finally, methodology concerning assembling the adaptive model follows in section 3.3.

3.1 Algorithm Assessment

We qualitatively assess several leading shadow removal algorithms (Chromacity, Physical, Geometry, SRT, and LRT removal) for their sensitivity to different environmental properties. Environmental properties are identified across diverse datasets, examples including shadow darkness, shadow directionality, and color saturation. Environmental property shifts, such as illumination changes, are also observed in multiple datasets.

In addition to analyzing the algorithms’ sensitivity to environmental change, we similarly assess the algorithms’ sensitivity to parametric shift, i.e., algorithm performance is qualitatively assessed according to the algorithm’s dependence on one or more curated parameter values. Analysis and assessment of the previously presented shadow removal algorithms is conducted using a series of graphical tools in conjunction with ground truths identifying shadow regions across eight different datasets with seven unique environments.

3.1.1 Data Collection

This section details the datasets used to conduct our assessment, as well as tools developed for analyzing the sensitivity of algorithms and parameters. The tools and techniques covered allow for both qualitative and quantitative assessment.

Datasets

A total of eight datasets were chosen for this assessment, and are summarized in Table 3.1. Datasets 2 - 8 (denoted by the prefix “aton_”) are provided under the Computer Vision and Robotics Research Laboratory (CVRR) in association with the University of San Diego [31]. The datasets were cataloged with the Autonomous Agents for On-Scene Networked Incident Management (ATON) project [5]. These datasets represent diverse environments, including both indoor and outdoor scenes, a range of shadow intensity, and images of varying saturation.

In addition, two datasets were included from the Performance Evaluation of Tracking and Surveillance (PETS) project [29]. In contrast to the ATON datasets, these sequences were explicitly chosen because they possess subsequences featuring rapid illumination changes, due to a shift in weather conditions and cloud cover. These environmental changes darken, lighten, and blend shadows in accordance with a background model. Figure 3.1 demonstrates the illumination changes within the PETS datasets.

All eight datasets were manually segmented to form ground truths that identify shadow

Table 3.1: Dataset information.

Name	Resolution	Sequence Length	# GT Frames
PETS1	768x576	175	12
PETS2	768x576	192	11
aton_highway1	320x240	440	8
aton_highway3	320x240	2227	7
aton_room	320x240	300	22
aton_campus	320x240	1179	53
aton_hallway	320x240	1800	13
aton_lab	320x240	887	14



Figure 3.1: PETS2 experiencing both high illumination (a) and low illumination (b) (due to cloud cover).

regions (gray) within foreground objects (white). Figure 3.2 illustrates the ground truths of dataset frames.

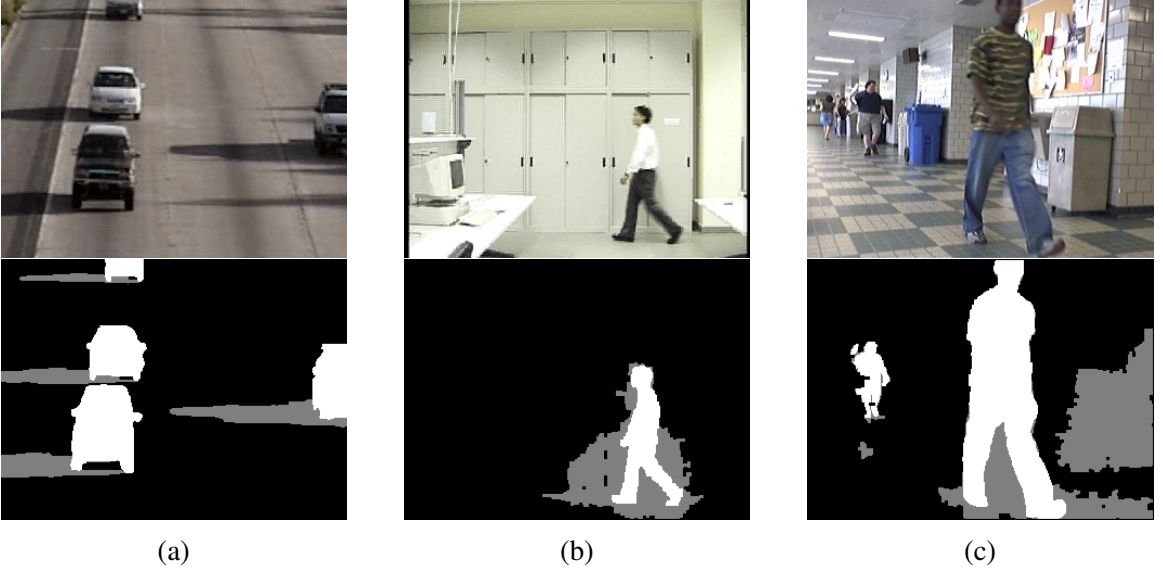


Figure 3.2: Datasets collected for ATON: (a) `aton_highway1`, (b) `aton_lab`, and (c) `aton_hallway`.

Assessment Tools

The first stage of our methodology is an exploration of the sensitivity of shadow removal algorithms to environmental and parametric change. We developed tools to assist intuition regarding an algorithm’s performance, capable of allowing a user to manually tune an algorithm parameter, and observe its effect on performance.

To better understand an algorithm’s dependence on a parameter, a framework was required to rapidly modify the parameter in question. The initial implementation of the shadow removal methods, courtesy of Sanin et al. [30], contained relevant parameters hard-coded into the algorithms. Each algorithm therefore required re-compilation to bring any modifications to fruition. This shortcoming was rectified by extracting each parameter and organizing them into an `.ini` file. By utilizing username *brofield*’s SimpleINI architecture, hosted on Github [32], parameters can be either set ex temporaneously or altered by an external script. An example SimpleIni `.ini` file is shown in Figure 3.3.

Graphical tools (GUI) were then developed to rapidly assess and visualize a parameter’s affect on shadow removal. Each shadow removal method was modified to accept

```
56 [PhysicalShadRemParams]
57 coneAngle = 0.15707963267
58 coneR1 = 0.3
59 coneR2 = 1.0
60 weightSmoothTerm = 4
61 learnBorders = 1
62 gmmGaussians = 5
63 gmmInitVar = 30
64 gmmMinVar = 1
65 gmmStdThreshold = 2
66 gmmWinnerTakesAll = 0
67 gmmLearningRate = 0.1
68
```

Figure 3.3: An example SimpleINI file. Parameters taken from this file are used to adjust values in real-time.

arbitrary parameter values in real-time from the .ini file. These parameters were then tied to graphical sliders (from OpenCV’s highgui library [33]) dictating their range and value. Any numerical parameter that has the potential to modify the Detection or Discrimination rates of a shadow removal method is included in the GUI. An example of the GUI is seen in Figure 3.4. The process in which the GUI modifies and displays parameters is illustrated in Figure 3.5.

The display is updated in real-time with both a visual representation of detected shadow pixels (in gray), and a quantified display of both the exact detection and discrimination rates, computed based on the ground truth. Leveraging human perception, the graphical tools enabled rapid evaluation of the sensitivity of an algorithm to changes in parameter values within specific scenes.

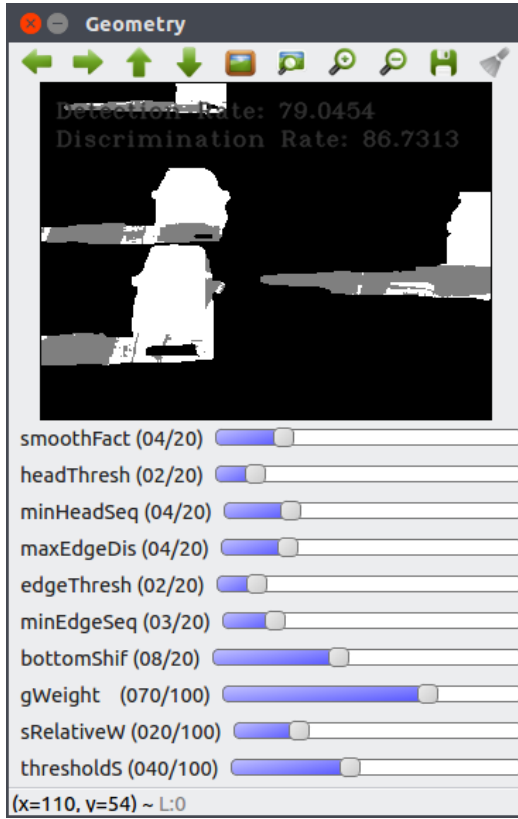


Figure 3.4: GUI tools created using OpenCV, displaying Geometry shadow removal.

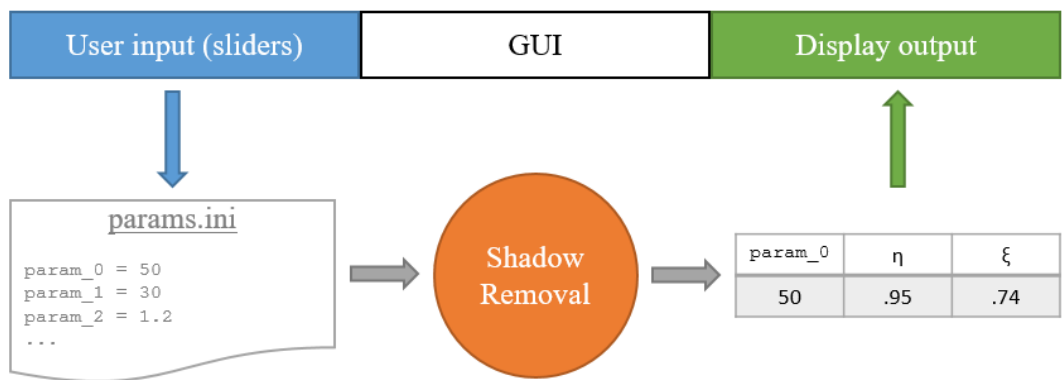


Figure 3.5: The GUI takes user input through sliders, updates values in a .ini file, which are used to produce a new output image indicating shadow versus foreground pixels with the corresponding detection and discrimination rates. The GUI then visualizes this output.

Determining Optimal Parameter Values

Modifying the algorithms to accept arbitrary parameter value settings at each frame enables us to create batch jobs to systematically vary parameter values across multiple runs. This allows us to meticulously sweep a given parameter (pr) through a specified range and record its corresponding affect upon detection and discrimination rates. Figure 3.6 illustrates the data collection process. The calculated detection and discrimination responses to change in pr are recorded as the functions $\eta(pr)$ and $\xi(pr)$, respectively. Both $\eta(pr)$ and $\xi(pr)$ are determined for one frame. Figure 3.7(a) demonstrates an example of these responses.

We also utilize the iterative process to determine the optimal value of pr for each frame in a dataset, i.e., which pr value yields the greatest improvements in detection and discrimination. This optimal value is denoted as pr^* . The detection and discrimination rates are summed, resulting in a shadow removal score $\Xi(pr)$ (Eqn. 3.1), which quantifies the efficacy of the shadow removal algorithm given a certain pr value. Figure 3.7(b) illustrates the score calculated using the responses found in Figure 3.7(a). We define the optimal value pr^* as the global maximum of $\Xi(pr)$ (Eqn. 3.2).

$$\Xi(pr) = \eta(pr) + \xi(pr) \quad (3.1)$$

$$pr^* = \max(\Xi(pr)) \quad (3.2)$$

To assess the performance of algorithms throughout a dataset, pr^* is calculated for each frame. The pr^* values are used to determine degrees of correlation for an environment, and set the foundation for a general model of arbitrary shadow removal improvement.

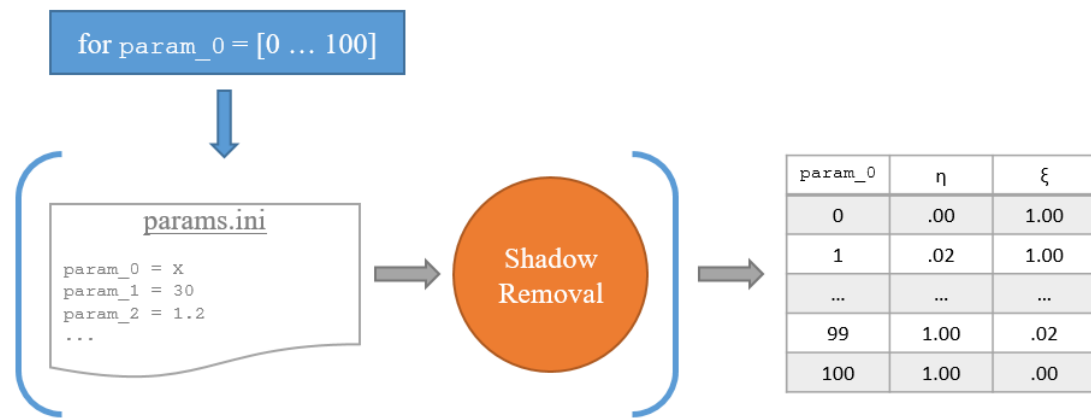
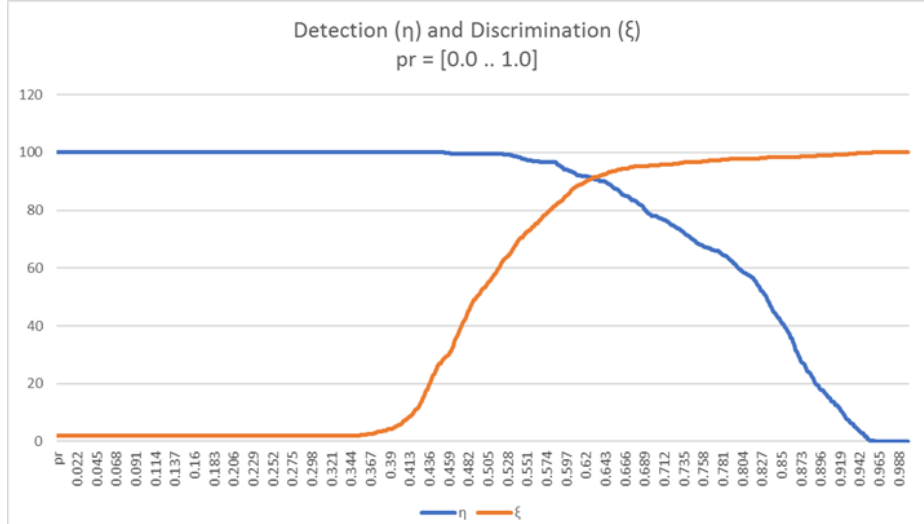
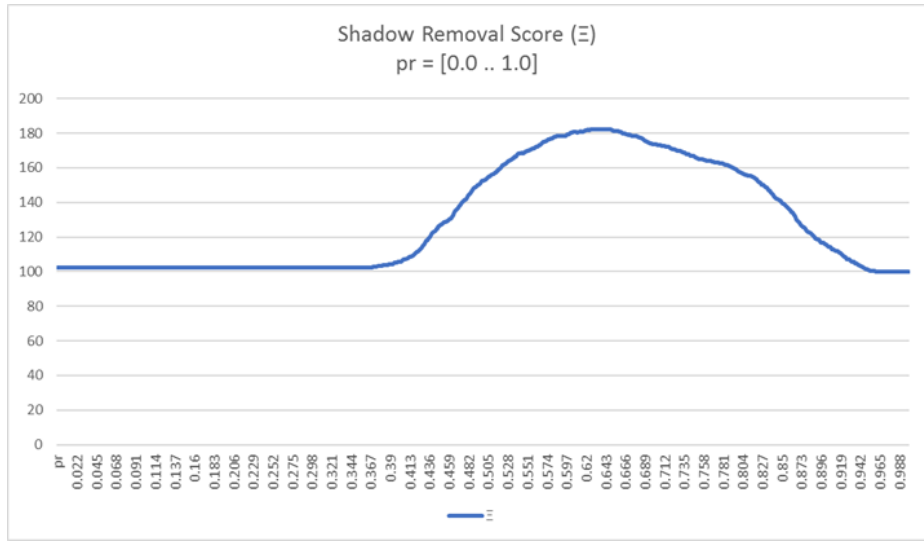


Figure 3.6: For one frame, a parameter is systematically iterated to provide detection/discrimination results for each possible parameter value.



(a)



(b)

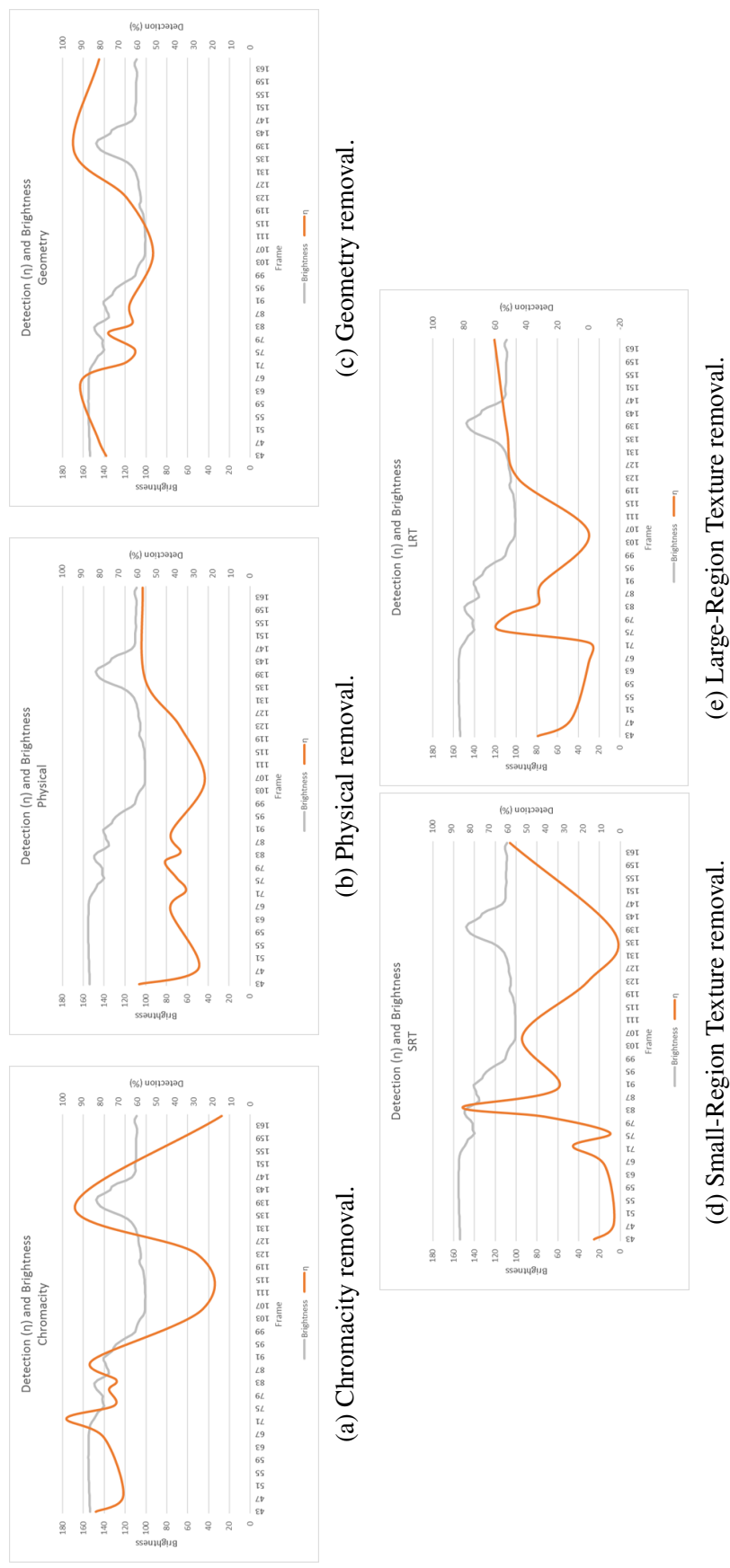
Figure 3.7: (a) Detection (blue) and Discrimination (orange) rates are charted against the iterated parameter value pr (x-axis). For each parameter value, detection and discrimination are summed to produce a removal efficacy score $\Xi(pr)$. The global maximum of this value is the optimal parameter value (pr^*).

3.1.2 Algorithm Selection Strategy

Using the tools detailed in section 3.1.1, we perform a brief qualitative assessment of the shadow removal algorithms’ sensitivity. Given the diversity of shadow removal methods, a wide array of environmental factors may potentially influence an even wider array of algorithmic parameters. The scope of this research has therefore been focused on identifying a suitable algorithm to assess, linking a parameter (intrinsic to this algorithm) to unique environmental properties or changes, and developing a model for real-time parameter adaptation based on correlations found.

Candidate shadow removal algorithms are evaluated according to the correlation between their efficacy (in terms of detection and discrimination rates) over time, and qualitative observations attributed to a dataset; e.g., the PETS1 dataset experiences a large illumination change midway through its sampling, which is taken into account when searching for trends among the accuracy of a candidate method. Figure 3.8 demonstrates shadow detection rates using the PETS1 dataset, for each shadow removal algorithm.

Figure 3.8: Shadow detection (η) (orange) for each algorithm, run on the PETS1 dataset during an illumination change. Overall brightness of a scene is shown in gray.



Evaluation of Methods

We evaluate popular shadow removal methods introduced in section 2.2: Chromacity, Physical, Geometry, SRT, and LRT. This section describes our rationale for using Physical shadow removal as part of our proof-of-concept, implemented starting in section 3.1.3. Our evaluation considers the tunable parameters of an algorithm, dependence on environmental properties and content, and sensitivity of relevant parameters.

A parameter’s sensitivity is evaluated by viewing its detection and discrimination responses ($\eta(pr)$, $\xi(pr)$). Figure 3.9 illustrates what is considered a sensitive parameter. A parameter is considered sensitive when a narrow range of parameter values affect detection and discrimination rates disproportionately. This sensitivity causes problems for an adaptive model, as the range of potential optimal parameter values (pr^*) is too small to correlate with environmental properties.

Both Geometry removal and SRT removal were shown to behave highly erratically from frame to frame even within an environmentally consistent dataset, demonstrated in Figure 3.10. Geometry-based removal remains dependent on the shape and consistency of processed foreground objects, and therefore dependent on the consistency of whichever foreground extractor is used for a scene. Furthermore, the algorithmic parameters associated with Geometry removal apply only to scenes in which the previous dependency is already fulfilled, i.e., the tunable parameters are relevant only to the geometric shapes nec-

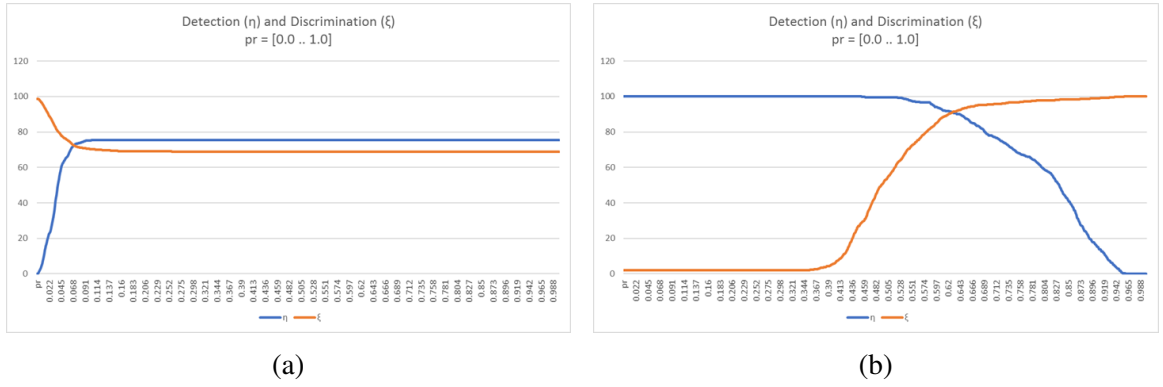


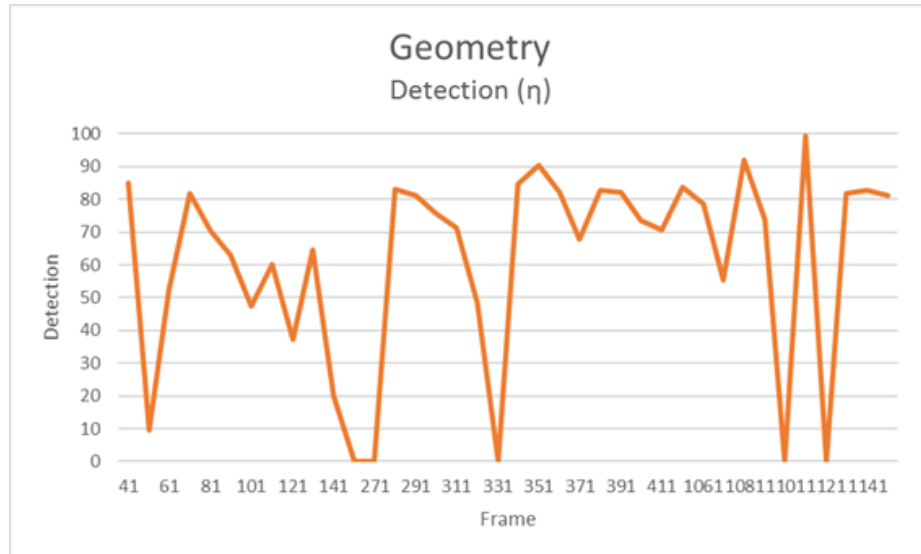
Figure 3.9: (a) depicts a sensitive parameter, while (b) represents a typical parameter.

essary to enable Geometry removal. These dependencies are not related to the properties of shadows within an environment, therefore we do not pursue further analysis with Geometry removal. SRT removal is based upon a series of Gabor filters used to characterize textural patches found in shadows, and match them to a corresponding background model. This technique requires that shadows cover textural portions of the background model large enough to perform meaningful analysis. Manual tuning of SRT’s algorithmic parameters provides no benefit to the algorithms detection or discrimination rates. This dependence on a shadow’s area, coupled with the lack of parameters suitable to improve shadow removal, eliminated SRT removal from candidacy.

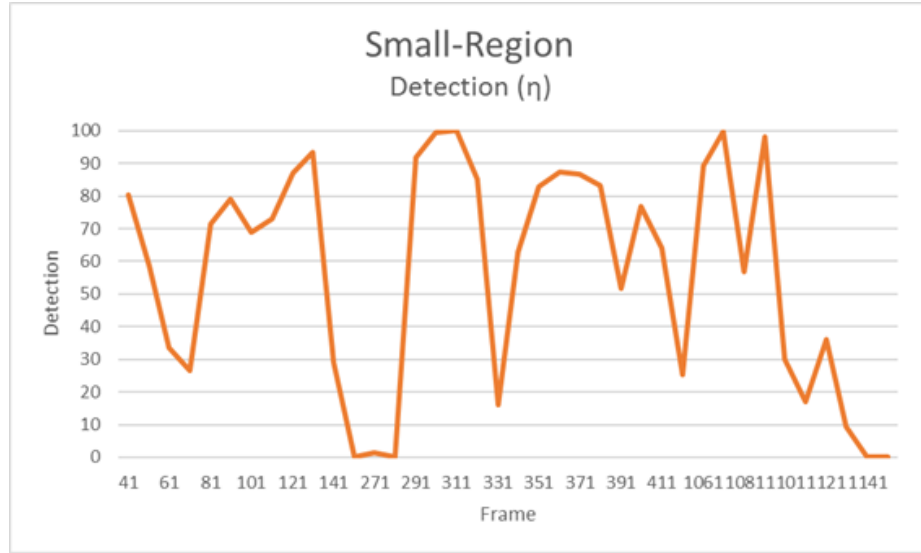
Sanin et al.’s Large-Region Texture algorithm was also eliminated from the assessment due to its inconsistent shadow removal, similar to Geometry and SRT removal (Figure 3.11). Some environments, such as the roadways of aton_highway1, yielded null detections for all frames. The Large-Region Texture algorithm recognizes the pitfalls of the Small-Region approach, such as restrictive texture regions, and attempts to correct them using hard-coded parameters. The algorithm primarily displays a sensitivity to environment, as identical parameter values produce vastly disparate shadow removal performances (Figure 3.11).

LRT also demonstrates varying levels of parametric sensitivity, also dependent on the deployment environment. For example, the parameter *avgAttenThresh* is highly sensitive, shown in Figure 3.12, and has only one value per frame that affects detection and discrimination. Furthermore, shadow removal is affected disproportionately to *avgAttenThresh*, with shadow detection rates often dropping to zero when affected. LRT has several parameters that behave in similar ways, demonstrating a lack of scalability for changing environmental properties.

Chromacity and Physical shadow removal provide tunable parameters that lie within acceptable ranges of sensitivity. An example of an acceptable range of sensitivity is seen in Figure 3.9(b). The shadow removal algorithms often respond similarly to the diversity

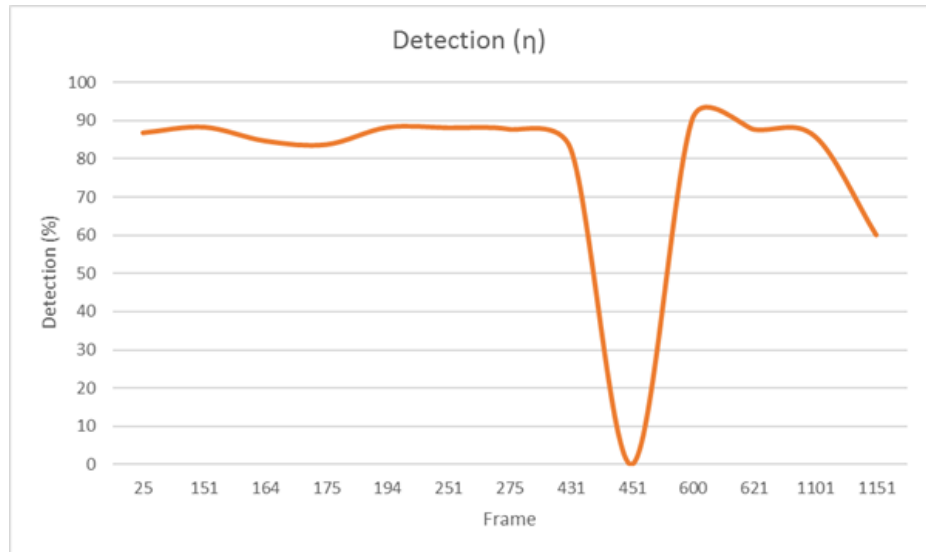


(a) Geometry

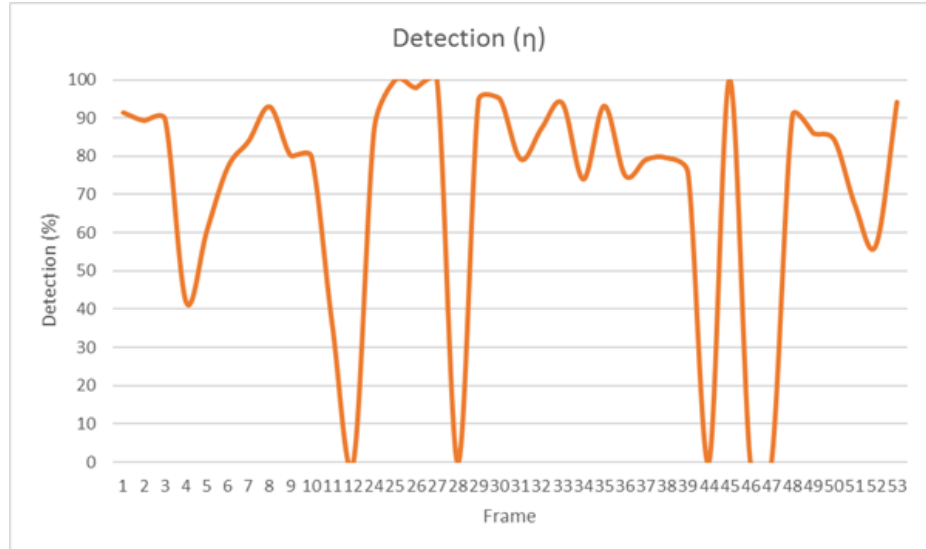


(b) Small-Region Texture

Figure 3.10: (a) and (b) showcase erratic shadow detection run on the dataset aton_campus, which experiences no significant illumination change.



(a)



(b)

Figure 3.11: (a) Run on aton_hallway, LRT shows consistent shadow removal accuracy, with occasional dips. (b) Run on aton_campus, LRT performs erratically.

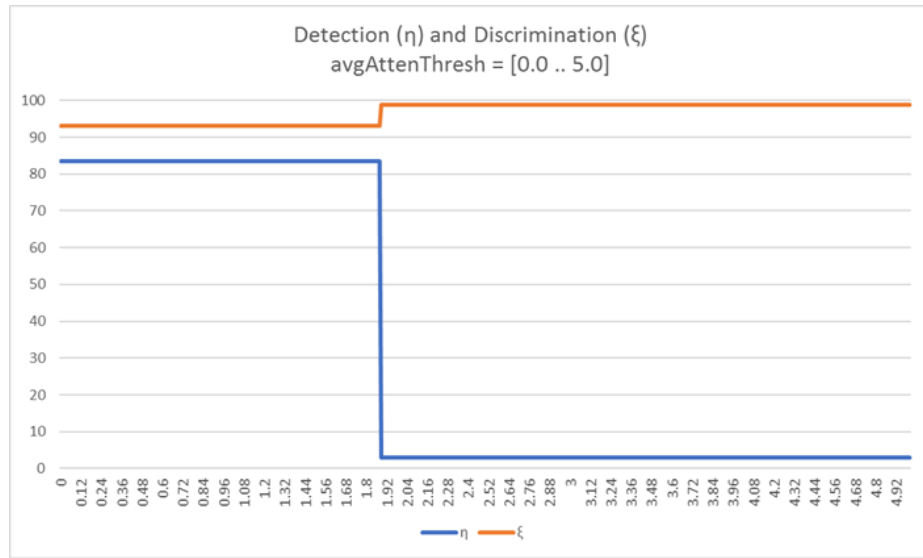


Figure 3.12: The LRT parameter *avgAttenThresh* is highly sensitive, demonstrating a narrow range for which LRT removal accuracy is affected. LRT's removal accuracy response is shown, using the *aton_highway1* dataset.

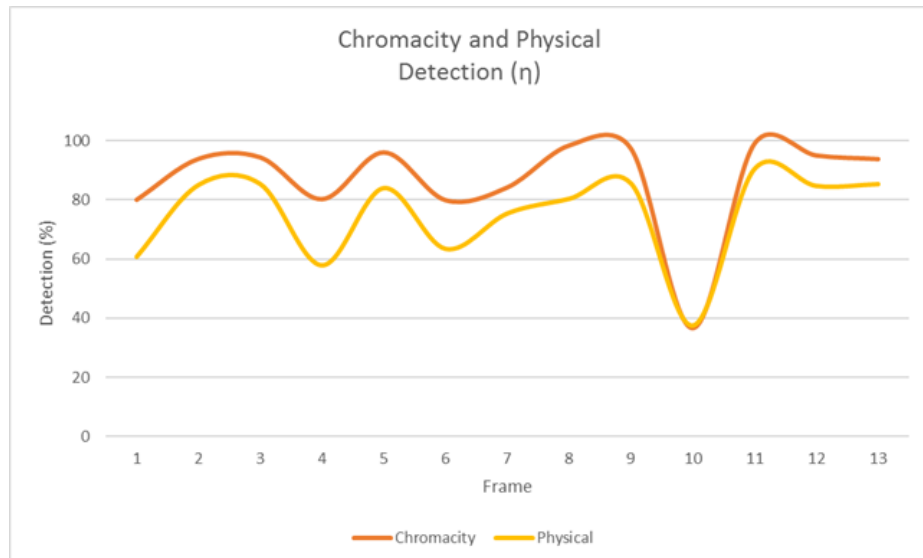


Figure 3.13: Chromacity and Physical shadow removal demonstrate similar shadow detection results run on *aton_hallway*.

of environments in this study; for example, Figure 3.13 illustrates comparable detection rates for the aton_hallway dataset. Chromacity and Physical shadow removal also display consistency between datasets, i.e., none of the datasets provide particularly poor results that are not linked to an environmental property change, such as illumination change. The Chromacity removal algorithm succeeds due to the tendency of shadows (within a dataset) to remain a consistent darkness when compared to the corresponding background model. However, this simple approach can prove problematic when illumination changes occur within a dataset. Physical shadow removal utilizes a similar system of gauging a shadow's darkness compared to a background model - what is referred to as a weak detector [8, 23, 27] - and implicitly suffers similar breakdowns of detection when presented with significant illumination flux within a dataset. Although they both suffer, Physical shadow removal employs a strong detector to increase detection and discrimination at the cost of processing time. In the end, Physical shadow removal was selected as the main experimental framework for this study, in part due to Physical shadow removal's more sophisticated model.

3.1.3 Selecting a Parameter of Physical Shadow Removal

Physical shadow removal operates in two stages: the weak detector, and the strong detector. The weak detector typically identifies candidate shadow pixels simply by eliminating impossible pixels, i.e., pixels that are brighter than the background model. The remaining foreground pixels are then provided as candidate pixels to the strong detector, which characterizes these pixels as either shadow or foreground. Our assessment of algorithmic parameters explores parameters in both of these detector spaces. Before we can illustrate which parameters were considered for experimentation, we must first understand each parameter's place within the algorithm.

Weak Detector - Physical Shadow Removal

The purpose of the weak detector is to prevent impossible pixels from being fed to the strong detector. The weak detector in Physical shadow removal functions similarly to the Chromacity shadow removal process; the candidate pixel is evaluated by its distance from a corresponding background pixel and sorted accordingly. The weak detector is visually, and technically, a cone projected in an RGB plane indicating the range in which a normalized shadow pixel may lie with respect to a background model. Normalizing the shadow pixel's position relative to the background model is accomplished by computing the angular distance between the RGB vector of the foreground and the RGB vector of the background. The resultant represents the color-space deviation from foreground to background. This threshold parameter is named *coneAngle* within the Physical shadow removal algorithm. The cone represents two dimensions: color deviation (θ), and intensity (or brightness) deviation. A foreground pixel is considered a possible shadow if the normalized ratio of foreground to background brightness (scaled by a function of the color deviation ($\cos(\theta)$)), is within a pre-defined brightness range. The tolerable brightness range, delimited by parameters named *coneR1* (minimum) and *coneR2* (maximum), is hard-coded within the original algorithm to be 0.3 to 1.0.

The main components of the weak detector are parameterized within the algorithm to fit a general model; $coneR1 < x < coneR2$ as an intensity range works reasonably well for many scenes, but there exists an optimal range for any given environment. Similarly, the optimal color angle (θ) between foreground and background vectors is dependent on environmental parameters. These parameters, *coneR1*, *coneR2*, and *coneAngle* are therefore considered when looking for correlations with environmental conditions.

Strong Detector - Physical Shadow Removal

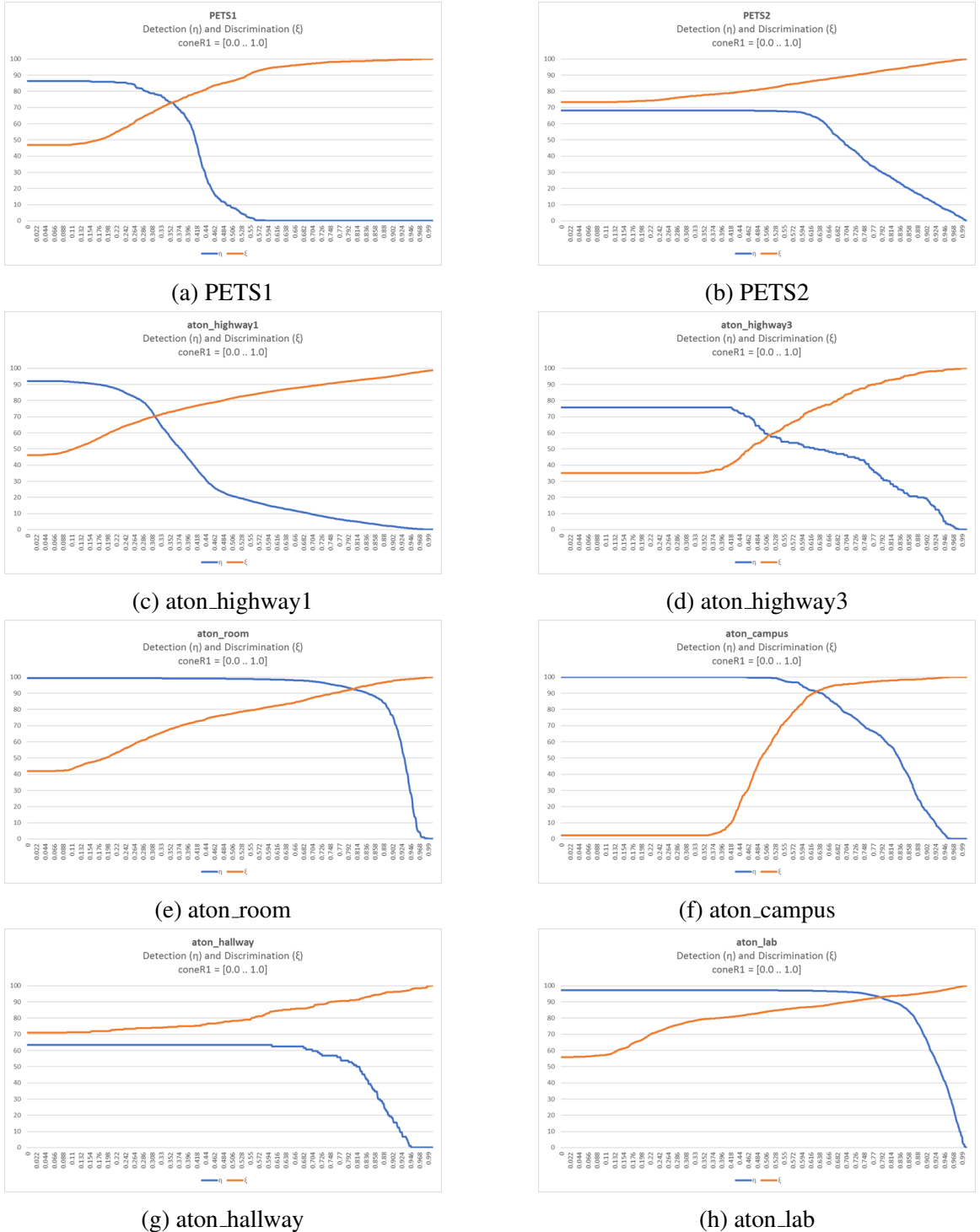
After the weak detector removes impossible candidates for shadow pixels, a Gaussian Mixture Model (GMM) is used to learn the color features of shadow pixels when compared to

background pixels. Using the remaining pixels, the GMM estimates the normalized spectral ratio for shadows in a scene, i.e., the ratio of spectral illuminants [27, 34, 35]. More information on spectral illuminants can be found in section 3.2.3. The GMM is a framework based upon Expectation Maximization and learning over time; therefore, the initial parameters presented in the algorithm have little influence over the efficacy of shadow removal. Shadow removal displayed sensitivity to only one significant parameter, *postThresh*, the parameter controlling the posterior threshold. The posterior threshold is the threshold governing shadow/foreground assignment after the posterior probability of a pixel is determined via the GMM. Since the GMM adapts to its environment, modifying the posterior threshold invalidates any learning the GMM has achieved. Therefore, correlating *postThresh* to environmental properties is not performed in this study.

Evaluation of Parameters

Due to their integral nature to both the weak and strong detectors, the parameters *coneR1* and *coneAngle* are evaluated for their effect on shadow removal. Each parameter is shown to have a pronounced effect on shadow removal.

Figure 3.14 demonstrates *coneR1*'s contribution to detection/discrimination across datasets. *coneR1*'s effect on shadow removal remains consistent and scalable. The parameter is exercised through a large range, with an equally large range of resultant detection and discrimination rates. Figure 3.15 shows that each dataset demonstrates an unambiguous maximum score, *coneR1**. The wider range and relatively coarse-grained nature of the parameter facilitates identifying trends and correlations with the iterations.



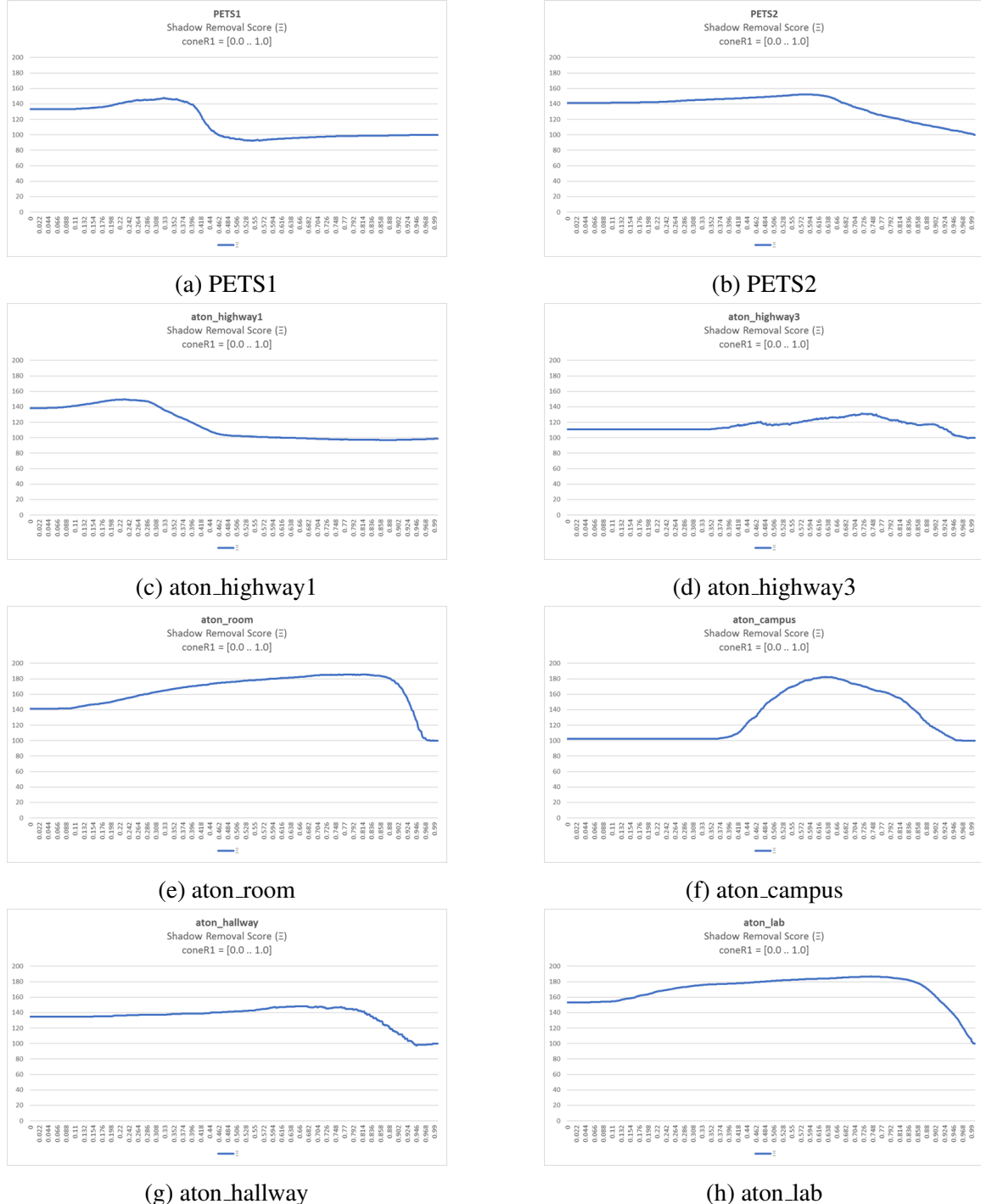


Figure 3.15: Example score (Ξ) of a frame for each dataset. Full results found in appendices.

$coneR2$ represents the upper limit of the cone describing a shadow pixel's color representation. While it serves a similar function as $coneR1$, upon sensitivity testing, $coneR2$ was never found to contribute to higher detection and discrimination rates. Its default value (1.0) is also its optimal value ($coneR2^*$). Figure 3.16 shows that the maximum of $\Xi(coneR2, coneR2^*)$, is 1.0 across multiple datasets.

$coneAngle$ inhabits too narrow a range of sensitivity to properly exploit (see results included in the appendices). Figure 3.17 illustrates the sensitivity of the parameter. Within the frames of a dataset, the calculated $coneAngle^*$ values are within millionths of one another. Furthermore, $coneAngle^*$ does not provide as large an improvement in shadow removal as $coneR1^*$ does. The minimal removal improvement and narrow range of sensitive values makes further examination of $coneAngle$ difficult. For the duration of this study, environmental feature correlations were sought only in relation to $coneR1$.

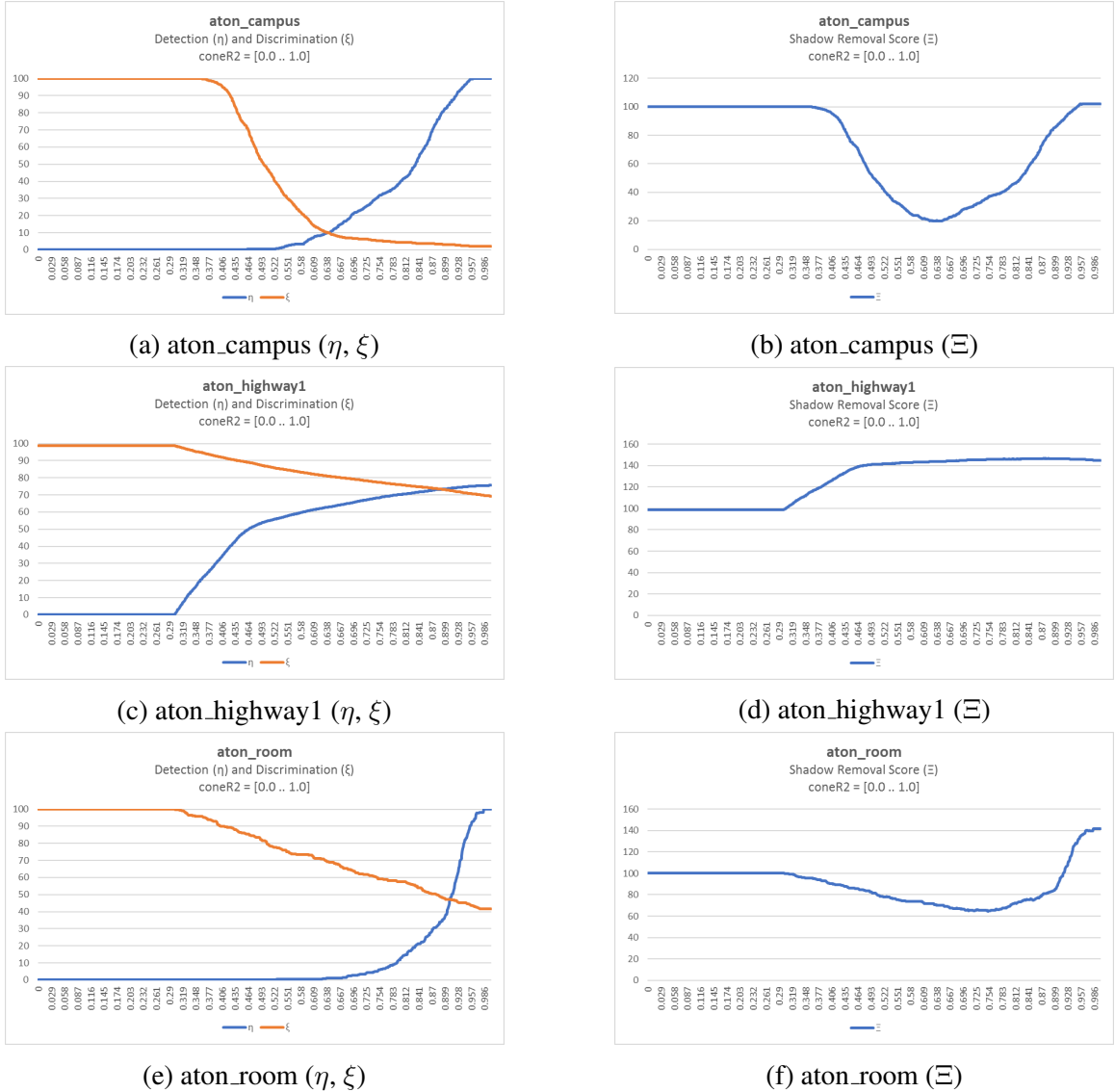
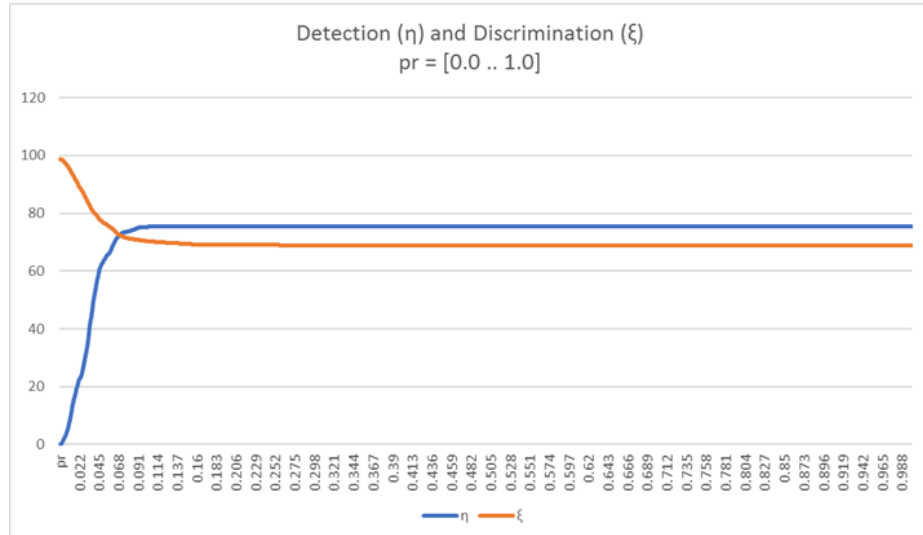
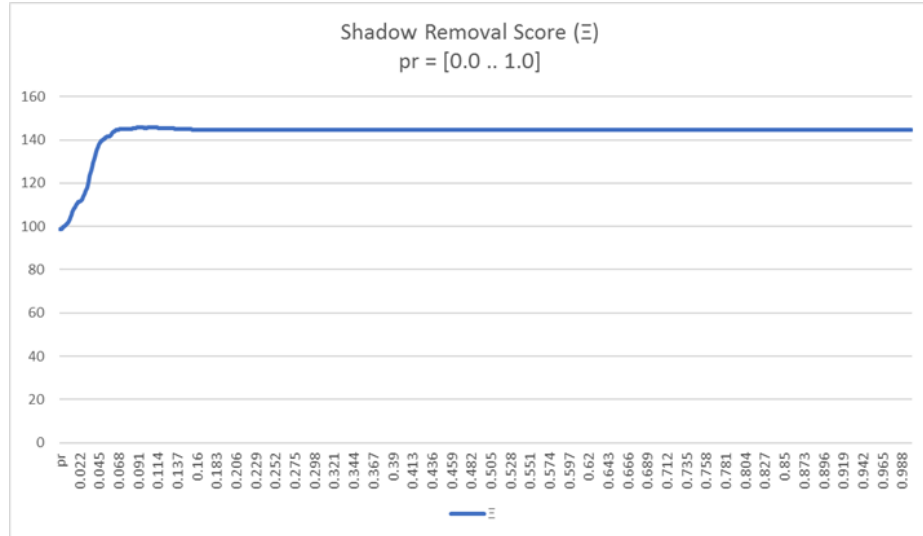


Figure 3.16: Parameter value responses for $coneR2$ for three datasets (aton_campus, aton_highway1, and aton_room). Full results found in appendices.



(a)



(b)

Figure 3.17: (a) Shadow removal response (detection and discrimination) for *coneAngle*, for aton_highway1. (b) Shadow removal score for aton_highway1. *coneAngle** is the maximum of the score.

3.2 Assessment of Environmental Properties

We now create a proof-of-concept of our adaptive model, by correlating environmental properties with a previously assessed parameter *coneRI*. We explore observed environmental properties within the datasets: attenuation and saturation. We also perform sensitivity analysis on multiple environmental properties (brightness functions, SIFT parameters) to explore their possible influence on correlation between *coneRI** and attenuation (α). A model is given for using the observed environmental properties to calculate a new variable *coneRI'*, which represents the adaptation of the *coneRI* parameter to more closely match the curated *coneRI** ideal value.

3.2.1 Previous Work - Large Region Texture Removal

Of all the leading shadow removal algorithms we evaluated, only one attempts to adapt its parameters to its current environment. In Sanin et al.'s LRT shadow removal [23], there are three examples of ambient environment properties taken into account: average saturation (of foreground pixels), average attenuation (from foreground to background), and average perimeter size of foreground objects. These three global properties govern the value of certain algorithm parameters.

LRT removal checks the average perimeter of foreground objects in a frame against a predetermined threshold. Average perimeter is linked to three additional algorithm parameters that control the size of the texture region being matched to identify shadows. If the average perimeter is above the predetermined threshold, the range of area for foreground/background correlation is expanded. The average perimeter is computed on a per-frame basis, while the threshold remains static.

LRT removal, like Physical shadow removal, uses a weak detector to retrieve candidate (shadow) pixels. The candidate shadow pixels must fit within a certain range of Hue (H), Saturation (S), and Value (V)(or Brightness) when compared against the background

model, i.e., the foreground HSV values subtracted from the corresponding background HSV values, referred to as ΔHSV , must fall within a specified range. There are two definitions of this acceptable range: $\Delta\text{HSV}_1 \in \{[0, 76], [0, 36], [0.6, 1.0]\}$, and $\Delta\text{HSV}_2 \in \{[0, 62], [0, 93], [0.21, 0.99]\}$. If the average saturation of all identified foreground pixels exceeds a predetermined threshold (average saturation = 35), ΔHS_2 ($\Delta H=[0, 62]$, $\Delta S=[0, 93]$) is used as the acceptable range. Similarly, if the average attenuation of the foreground pixels (compared to corresponding background pixels) exceeds its threshold (average attenuation = 1.58), the latter range of ΔV_2 ([0.21, 0.99]) is used for evaluating brightness.

This coarse-grained approach enables the LRT algorithm to switch between two presets for multiple parameters, based on observed environmental properties. However, the two presets (ΔHSV_1 , ΔHSV_2), and the thresholds that govern them, require empirical knowledge about the scenes in which they are deployed. The preset-switching fails to adapt to environmental properties in a scalable manner. Applied to a 24-hour video feed, the preset-switching model certainly fares better than the naive fully hard-coded approach, but compromises shadow removal with its rigidity. We seek to adapt parameter values on a per-frame basis, with the scalability necessary to create a continuous function of environmental properties to parameter values.

This need for adaptability underscores the motivation of this research to discover a scalable and portable solution for parameterization. In the case of Physical shadow removal, foreground object perimeter has no bearing on the accuracy of shadow removal, because Physical removal utilizes a wholly pixel-based approach. However, both average saturation of foreground objects and average attenuation are examined further in this study, as described in the next section.

3.2.2 Attenuation and Saturation

Attenuation (α) represents the loss of intensity from foreground pixel to background pixel in a frame. Traditionally, brightness attenuation is represented mathematically in decibels

(dB) as the ratio of background and foreground brightness (Eqn. 3.3). The *brightness()* function used here is the HSV brightness function (Eqn. 3.5), which defines brightness as the maximum value between the R,G,B channels of a pixel.

$$\alpha_{dB} = \frac{brightness(\vec{bg}(p))}{brightness(\vec{fg}(p))} \quad (3.3)$$

p represents pixel coordinates. In an effort to better capture shadow pixels, we discard any pixel where $\alpha < 1.0$, implying it is brighter than its corresponding background. While the α_{dB} representation adheres most closely to the physical definition of light attenuation within a shadow, we consider the reciprocal of this model ($1/\alpha_{dB}$) of attenuation for correlation. As all considered pixels have an α_{dB} of at least 1.0, the reciprocal bounds the value between 0.0 and 1.0. This range is more suitable for correlation calculations, as the covariance between data points is easily affected by large changes in value. More information regarding correlation is found in section 4.1.

Alternatively, we consider the *percentage change* ($\% \Delta$) model of light attenuation. This model is defined in Eqn. 3.4.

$$\alpha_{\% \Delta} = \frac{brightness(\vec{bg}(p) - \vec{fg}(p))}{brightness(\vec{bg}(p))} \quad (3.4)$$

$(1 - \alpha_{\% \Delta})$ is considered for correlation, which indicates the percentage of a background pixel's intensity the foreground represents.

Saturation is the measurement of “depth of hue” in a pixel, e.g., a lower saturation means the base hue is less expressed, while a higher saturation means the color of a pixel more closely matches the base hue. The saturation level of a background pixel affects the intensity attenuation a shadow pixel experiences. Saturation properties are discussed in greater detail in section 3.2.5.

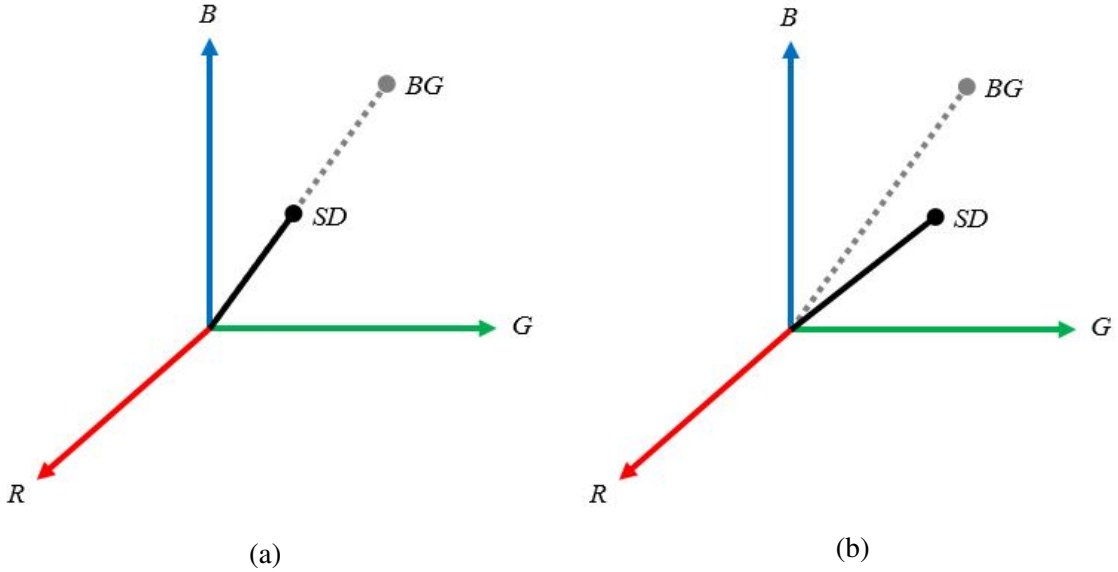


Figure 3.18: (a) Shadow pixel SD is attenuated linearly from background pixel BG . (b) SD is attenuated non-linearly.

3.2.3 Non-linear Attenuation and Spectral Properties of Light

In the ideal case, the attenuation of light is an entirely linear function, i.e., a shadow pixel lies along the vector drawn from the background pixel to the origin within the three dimensional RGB space [27]. Figure 3.18 illustrates attenuation of a pixel linearly and non-linearly.

Due to physical properties of illumination and reflectance, this linearity does not always hold true; cast shadows in real-world scenes are caused by more than one illumination source. In an outdoor scene, a shadow may be the product of direct sunlight, blue light refracted from the sky, and diffuse light scattering from nearby objects or surfaces. Any of these factors contribute to color bleed [27], influencing the attenuation of shadow pixels. These disparate light sources are said to have different *spectral power distributions*, different illumination characterized by varying concentrations of constituent wavelengths. This non-linear attenuation model is the primary motivator behind using GMM to learn a shadow's color model in [27].

Observed Spectral Properties in Outdoor Scenes

Since the spectral properties of an illumination source cannot always be predicted, this study attempts to observe trends across datasets to properly characterize shadows. By visualizing the magnitude of color shift due to shadows, we can clearly partition datasets into outdoor and indoor images. Outdoor datasets experience change disproportionately in each channel of an RGB image, while indoor datasets are characterized by equal and predictable shifts in each channel.

This disproportionate discrepancy is most apparent during periods of large illumination change, found prominently in datasets PETS1 and PETS2. Examining the outdoor datasets, we can see that the red and green channels experience larger magnitude shifts than in the blue channel. Based on assumed spectral power distributions of the source illumination found in the outdoor scenes, we can deduce that outdoor scenes display an introduction of blue light scattered from the sky that is not present in indoor scenes. With a spectral power distribution skewed towards blue, the red and green channels experience greater perturbation than the blue channel due to cast shadows. This study attempts to utilize this observed multi-illuminant model to better characterize the attenuation model assumed by a scene.

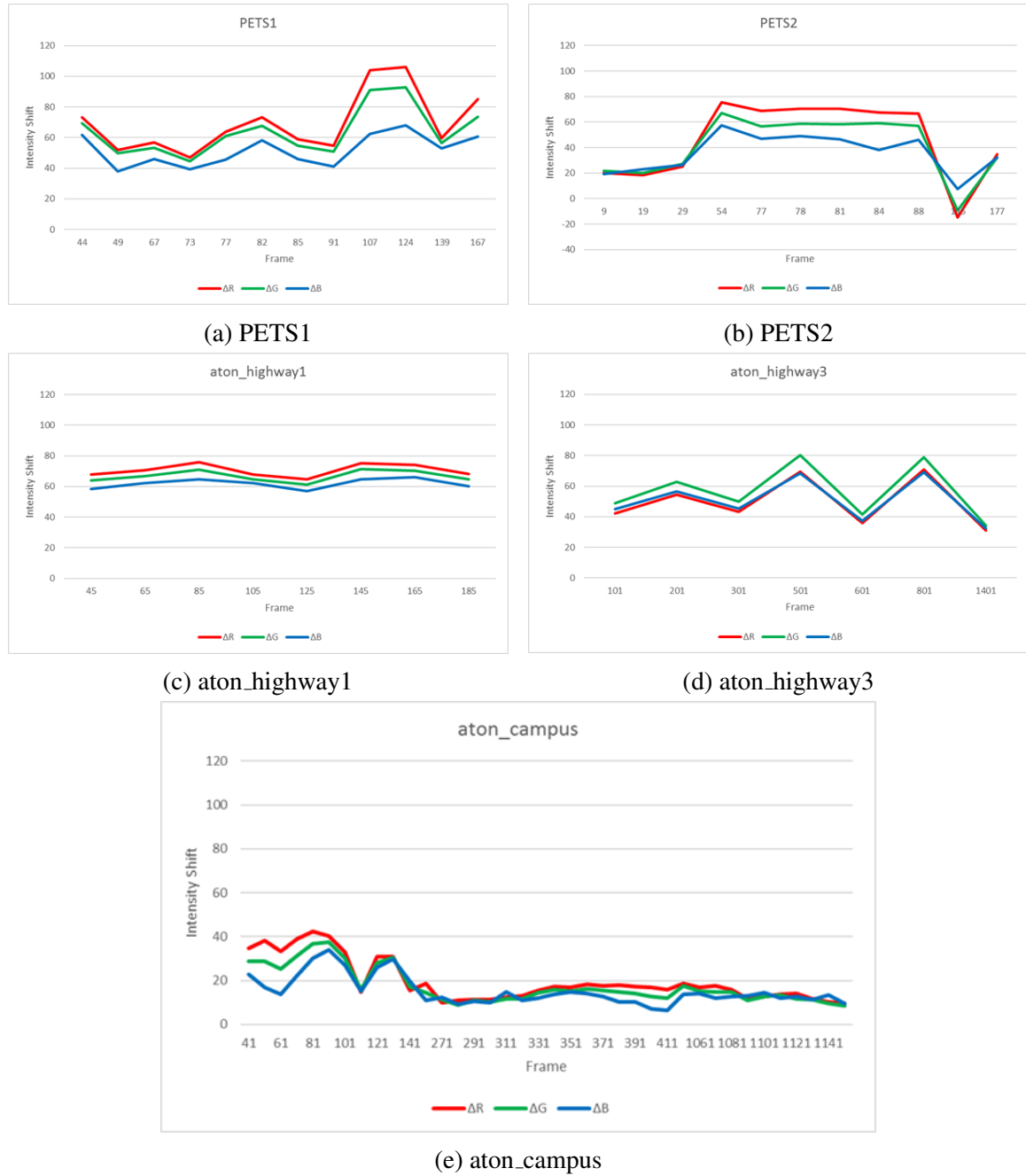


Figure 3.19: Outdoor datasets demonstrate consistently greater deviations in the red and green channels. During illumination changes (evident in PETS1 and PETS2), the red and green channels shift disproportionate to that of the blue channel, indicating scattered blue light is a primary component of the shadows' spectral illuminant ratio.

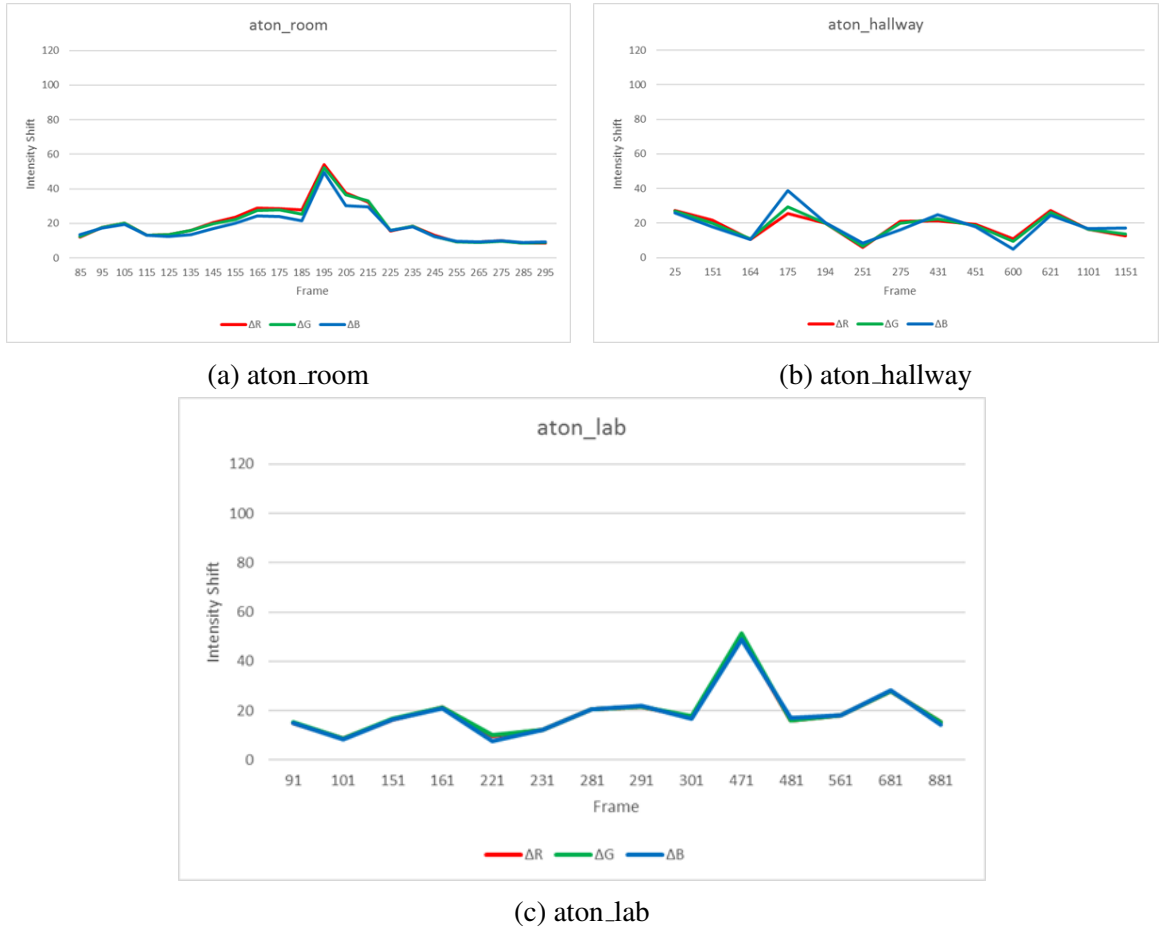


Figure 3.20: Indoor datasets demonstrate closer grouping of each channel's color shift. aton_hallway behaves most erratically of the indoor datasets. This is due to color-bleed from nearby objects, making aton_hallway the most diverse spectral ratio of the indoor sets. aton_lab behaves linearly, as expected.

3.2.4 Brightness Models

Since attenuation is a function of brightness, we attempt to utilize multiple methods of calculating brightness to improve attenuation modeling. We use different brightness functions in the calculation of α for each dataset, hypothesizing that correlation between α and $coneRI^*$ can be improved using different brightness functions. We conduct a sensitivity analysis to determine the effect that different brightness models can have on attenuation.

Below is a short taxonomy of popular brightness models studied. Each of the brightness models included are tested and analyzed for its affect on the α model.

HSV

Described as a ‘hexcone’ model, [36], brightness in an HSV representation is defined as the maximum value of the pixel represented in the red, green, and blue channels ($R\vec{G}B(p)$).

$$V = \max(R, G, B) \quad (3.5)$$

HSV can lead to misrepresentation of brightness as it is perceived by the human eye. This is because, as noted in Rec. 709/601 [37, 38], the same intensity of green appears brighter than that of red, which, in turn, appears brighter than the same intensity of blue. In the HSV scheme, green at full intensity ($R\hat{G}B = (0, 1, 0)$) matches the brightness of blue at full intensity ($R\hat{G}B = (0, 0, 1)$). It also minimizes contributions from channels other than the dominant channel, e.g., $R\hat{G}B(0, 1, 0) = R\hat{G}B(.9, 1, .9)$. HSV therefore is best suited for environments characterized by abnormally low saturation, where light attenuation due to shadows is most linear. Environments most likely to benefit from using HSV are scenes with a single illuminant source, such as indoor scenes.

HSI

HSI represents the most basic understanding of brightness, as *Intensity*.

$$I = \frac{R + G + B}{3} \quad (3.6)$$

This understanding of brightness serves most environments properly, as it caters to each channel equally. However, HSI still suffers from the inherent luminance of certain colors, and fails to compensate for them.

HSL

HSL, a brightness representation called *Lightness*, is called a ‘bi-hexcone’ model [36]. Lightness is an average of the primary and tertiary color components:

$$L = \frac{\max(R, G, B) + \min(R, G, B)}{2} \quad (3.7)$$

Excluding the secondary color component has the effect of translating the brightness plane described by HSI. While perceptually similar to other brightness models, HSL provides more balanced values when one channel’s value is in extrema.

Relative Luminance (Y)

Originally issued in 1982, Rec. 601 [38] defines one of the first standards for converting analog signal into digital video. *Relative Luminance (Y)*, or, when gamma-corrected, *Luma (Y')* is the simplest extrapolation of perceptually-relevant brightness. Luminance is defined as a coefficient-weighted linear combination:

$$Y = 0.299R + 0.587G + 0.114B \quad (3.8)$$

Rec. 709 later modified the coefficients to 0.21, 0.72, and 0.07, respectively. For this

study's experimental purposes, Rec. 601 coefficients were used. This brightness model highlights the human eye's sensitivity to green hues, and is therefore particularly relevant when observing outdoor scenes.

Euclidean Norm

Taking the Euclidean norm of an $R\vec{G}B$ vector is measuring the three-dimensional distance from absolute black, $R\vec{G}B = (0, 0, 0)$.

$$Norm = \sqrt{\Delta R^2 + \Delta G^2 + \Delta B^2} \quad (3.9)$$

While the Euclidean norm does not weight the channels perceptually, as Luminance does, it does represent the most accurate way to determine the color difference between two $R\vec{G}B$ vectors, and therefore proves valuable when comparing foreground pixels to background pixels.

HSP

HSP, or *Perceived Brightness*, combines the three dimensional distance of Euclidean norm, and the perceptually weighted coefficients of Luminance. HSP was introduced by Darel Rex Finley in 2006 [39].

$$P = \sqrt{0.299\Delta R^2 + 0.587\Delta G^2 + 0.114\Delta B^2} \quad (3.10)$$

Ideally, HSP provides the most accurate perceptually conscious brightness. Environments that experience large saturation shifts due to shadows benefit primarily, as both color distance and weighted coefficients are considered.

3.2.5 Low-contrast SIFT Keypoints

A scene typically contains a large set of low-level textural features unique to it. These low-level features have been characterized and quantified in many ways, such as the SIFT, SURF, or FAST feature descriptors [40, 41, 42]. These feature descriptors are used for image recognition and retrieval, and are robust to varying scales, rotations, and translations. These algorithms are traditionally performed on intensity images, i.e., grayscale images. However, hue and saturation play a large role in scene characterization. Therefore, SIFT implementations were developed to incorporate color information. Popular implementations of a color-SIFT method are HSV-SIFT, RGB-SIFT, HueSIFT, and others [43, 44, 45, 46, 47, 48].

Intensity images, while discarding chromatic information, often retain structural and textural information, due to image gradients' invariant basis in intensity. We assume a cast shadow similarly has minimal impact on underlying structures and textures, due to the success of textural shadow removal methods. As a result, SIFT keypoints remain largely invariant between a frame and its background model in intensity images. Since cast shadows do not modify the underlying textural structure, they do not affect the detection of SIFT keypoints.

In a traditional understanding of shadow attenuation as a linear process, both the hue and saturation of a pixel remain constant, as the intensity attenuates in a shadow region. Since this study assumes a different, non-linear understanding of light attenuation, we sought for representative changes that shadows bring to the hue and saturation channels of an HSV image. By detecting and displaying SIFT keypoints in the saturation channel alone, we observe qualitatively small localized structure changes within these shadowed regions (Figure 3.21).

We attempt to characterize these localized changes in structure using HSV-SIFT, by detecting SIFT keypoints using only the saturation channels of both a frame and its corresponding background model. It is apparent that foreground objects introduce significant

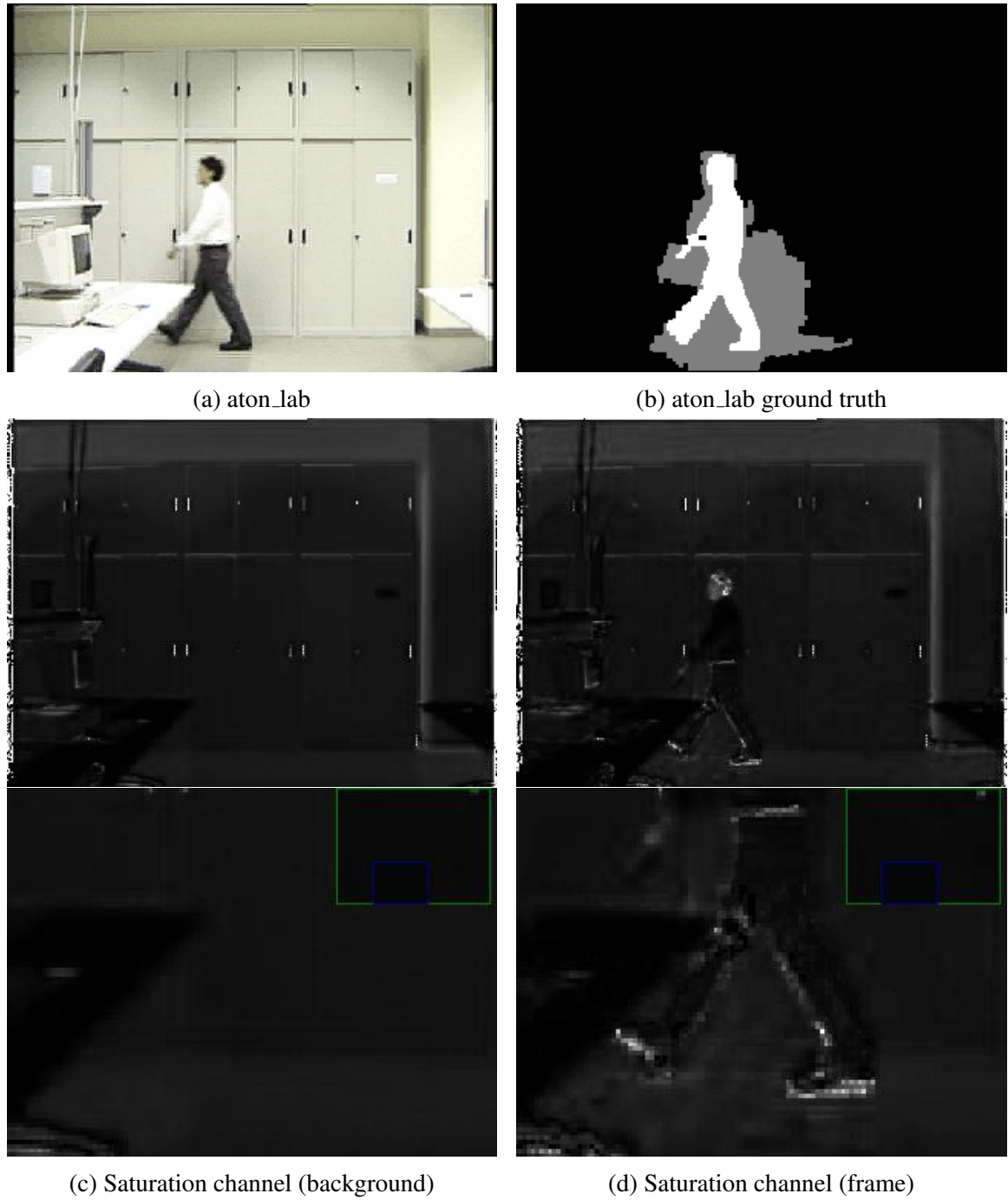


Figure 3.21: The limited structural effects of cast shadows in the saturation channel (d).

structural changes in any of the three channels, therefore the collection of SIFT descriptors is limited to only those considered *low contrast*. The SIFT algorithm operates in four major stages: scale-space extrema extraction, elimination of low-contrast keypoints, elimination of strong edge responses, and the assignment of orientations. Finally, low-contrast detections are eliminated due to their susceptibility to noise [40]. In our study, we instead preserve low-contrast SIFT keypoints, to characterize the small structural changes found in shadow regions. We build two matrices: the first containing keypoints of low and normal contrast (still excluding edge responses), and the second containing only normal contrast keypoints. We then extract low-contrast keypoints using an exclusive-or operation. The non-linearity of light attenuation, paired with previously observed structural changes, make shadowed regions in the saturation channel ripe regions for low-contrast SIFT keypoints. When drawn onto the source frame, we can see that low-contrast SIFT keypoints align loosely with shadowed regions (Figure 3.22).

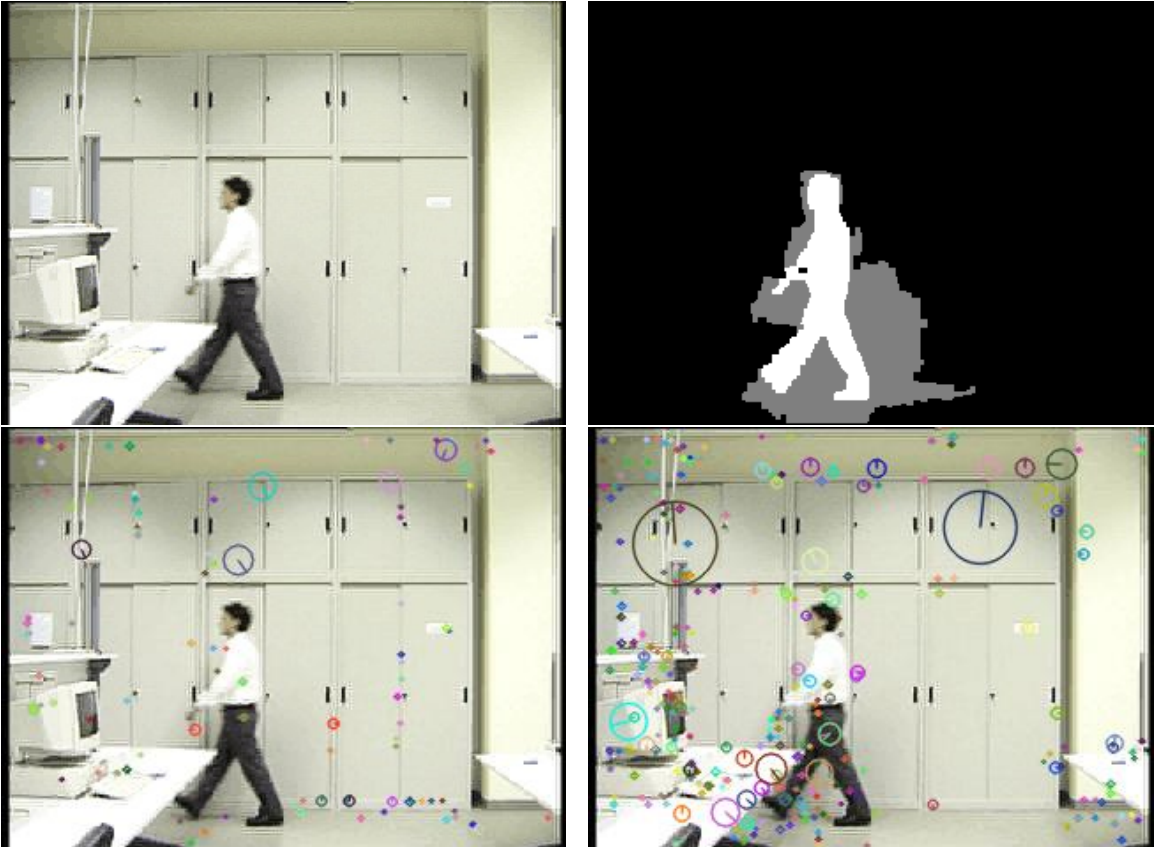
With shadows partially characterized by low-contrast SIFT keypoints, this study utilizes this insight by modeling the approximate proportion of shadows introduced in a given frame. The quantity of detected SIFT features in a frame f is represented as $SIFT_c(f)$, where c represents the contrast ratio parameter used. The ratio of total low contrast SIFT features to normal SIFT features is calculated for a single frame in Eqn. 3.11.

$$SIFT_{\%C}(f) = 1 - \frac{SIFT_{0.04}(f)}{SIFT_{0.01}(f)} \quad (3.11)$$

$SIFT_{0.04}$ represents features captured using the default contrast threshold (0.04), and $SIFT_{0.01}$ represents features captured using a lower contrast threshold. We then compare the $SIFT_{\%C}(f)$ ratios of the foreground and background frames, as defined in Eqn. 3.12.

$$SIFT_{fg/bg} = \frac{SIFT_{\%C}(fg)}{SIFT_{\%C}(bg)} \quad (3.12)$$

The resultant $SIFT_{fg/bg}$ estimates the percentage change of the number of detected



(a) Low-contrast SIFT keypoints detected using the intensity channel.

(b) Low-contrast SIFT keypoints detected in the saturation channel.

Figure 3.22: Detecting low-contrast SIFT keypoints in the saturation channel more effectively captures structural changes than in the intensity channel, due to cast shadows.

low contrast SIFT features from the background to the current frame. We assume a greater presence of low contrast SIFT features loosely indicates a greater quantity of shadows in a frame. In order to boost correlation between a parameter and a primary environmental property, $SIFT_{fg/bg}$ is multiplied against the value of an observed environmental property (in our case, α), serving as a scaling factor. We use this scaling factor to perform sensitivity analysis using the parameter $coneRI^*$ and the environmental property α . Results of this analysis are found in section 4.1.2.

3.3 Weak Detector Estimation - Creating a Model

With $coneRI^*$ calculated for a wide variety of datasets, we can begin to model a difference between environmental properties and the optimal parameter. While the attenuation from the foreground to the background displays a correlative relationship to $coneRI^*$, this correlation does not indicate a relationship to the magnitude of $coneRI^*$. This is due to the nature of the properties of attenuation. The attenuation calculation utilized is a function of brightness shift as a percentage of a background value, e.g., a pair of foreground/background pixels with a value of 50 and 100 produces the same attenuation as a pair valued at 25 and 50. Normalizing correlative environmental properties, we model an optimal shift from observed properties to the optimal value of the weak detector, i.e., the shift is modeled as $shift_{req.} = (coneRI^* - \alpha)$.

$shift_{req.}$ can be extrapolated from the magnitude of color shift (ΔRGB) found from foreground to background. By plotting ΔRGB against $shift_{req.}$, we produce a general relationship. Using data points from each frame in each dataset, we can produce a best-fit polynomial to generalize a model of attenuation and brightness magnitude shift into a function dictating the required shift of attenuation (shown in Figure 3.23). This required shift is defined as $shift_\alpha$. To avoid over-fitting, a parametrized logarithm was chosen to represent the required magnitude shift (ΔRGB). The logarithm used to calculate $shift_\alpha$,

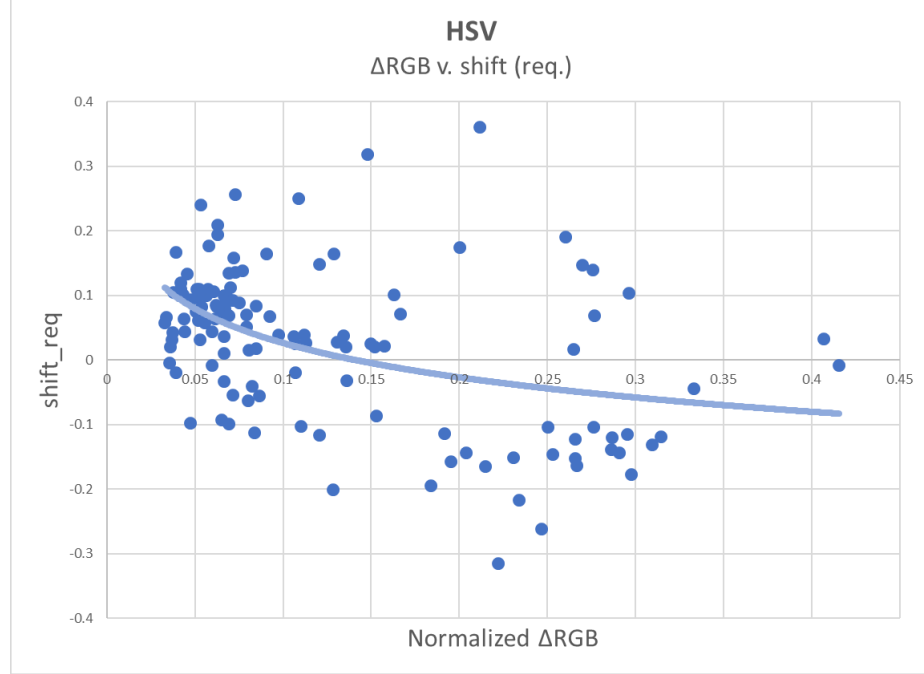


Figure 3.23: Regression performed on RGB shift found per frame, vs. required magnitude shift to optimal.

derived from Figure 3.23, is defined in Eqn. 3.13.

$$shift_{\alpha} = -0.11307 * \ln(\Delta RGB) - 0.1884 \quad (3.13)$$

We are now able to calculate a new algorithmic parameter, $coneRI'$. $coneRI'$ is calculated per frame, based on $\alpha_{\% \Delta}$. Calculating $coneRI'$ is shown in Eqn. 3.14.

$$coneRI' = (1 - \Delta RGB) * (1 - \alpha_{\% \Delta}) + shift_{\alpha} \quad (3.14)$$

CHAPTER 4

RESULTS

This chapter contains results for the correlation of algorithm parameter $coneRI^*$ and environmental property α , improvements to this correlation, and resulting calculated parameter $coneRI'$. Section 4.1 describes the correlations (ρ_α) found between $coneRI^*$ and both models of average attenuation (α_{dB} and $\alpha\%_\Delta$). The correlations are compared based on their fit to $coneRI^*$. Section 4.1.2 contains results regarding two indirect environmental properties ($SIFT_{fg/bg}$ and brightness calculation method) and how they affect correlations (ρ_α). The parameter $coneRI'$ is calculated, and its effect on the detection and discrimination of Physical shadow removal is shown in section 4.2. The resultant detection and discrimination rates are compared to those generated by the default parameter value.

4.1 Correlation of Parameters

We observe correlation between two parameters using the statistical definition of the correlation coefficient ($\rho_{X,Y}$), defined in Eqn. 4.1.

$$\rho_{X,Y} = \frac{cov(X, Y)}{\sigma_X \sigma_Y} \quad (4.1)$$

cov represents covariance, and σ_S represents the standard deviation of a set S . The correlation coefficient is unitless, and measured from $-1.0 < \rho_{X,Y} < 1.0$. A correlation coefficient of 0 indicates the variables X and Y are uncorrelated, while -1.0 indicates the variables are perfectly inversely correlated; likewise, a correlation coefficient of 1.0 means X and Y are perfectly correlated. Correlation coefficient is used to estimate an environmental parameter's potential usefulness for calculating a new $coneRI$ for use in an arbitrary environment. We represent the correlation between $coneRI^*$ and α as ρ_α .

Table 4.1: Datasets and their α_{dB} correlations to $coneRI^*$.

Dataset	ρ_α
PETS1	0.199
PETS2	0.671
aton_highway1	0.684
aton_highway3	0.742
aton_room	0.548
aton_campus	0.360
aton_hallway	0.656
aton_lab	0.695

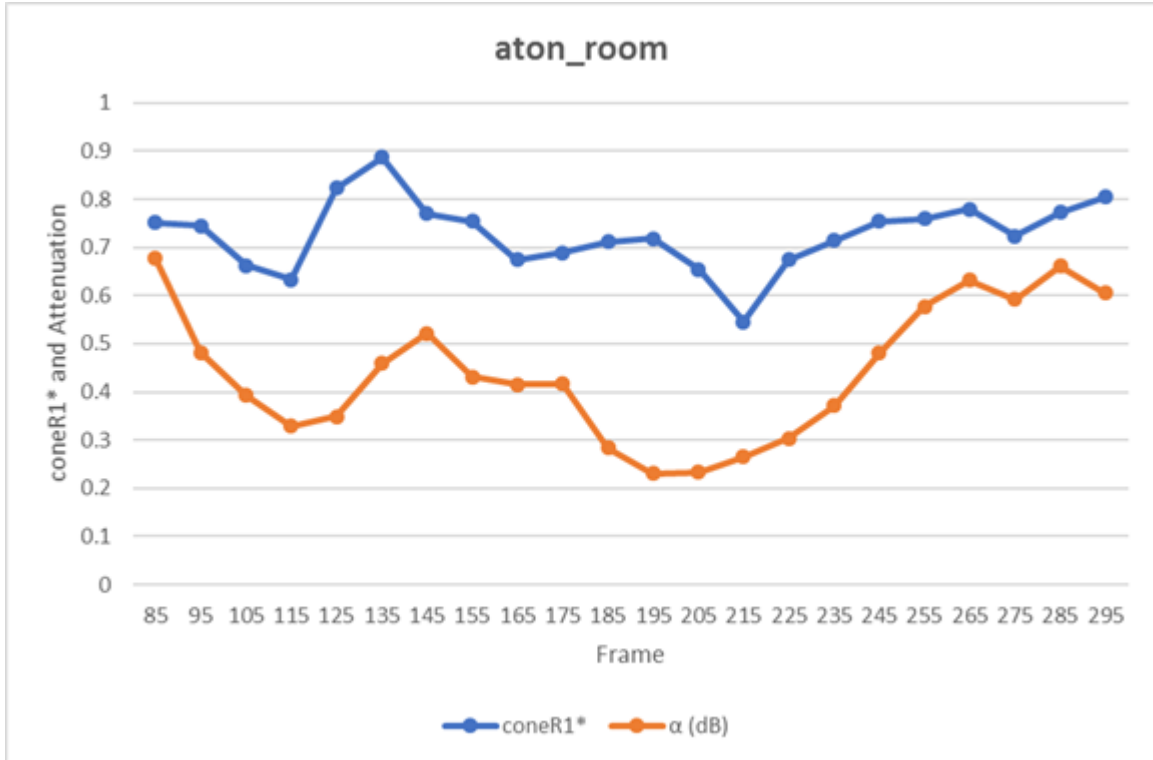
Table 4.2: Datasets and their $\alpha\%_\Delta$ correlations to $coneRI^*$.

Dataset	$\rho\%_\Delta$
PETS1	0.184
PETS2	0.743
aton_highway1	0.592
aton_highway3	0.801
aton_room	0.623
aton_campus	0.564
aton_hallway	0.690
aton_lab	0.551

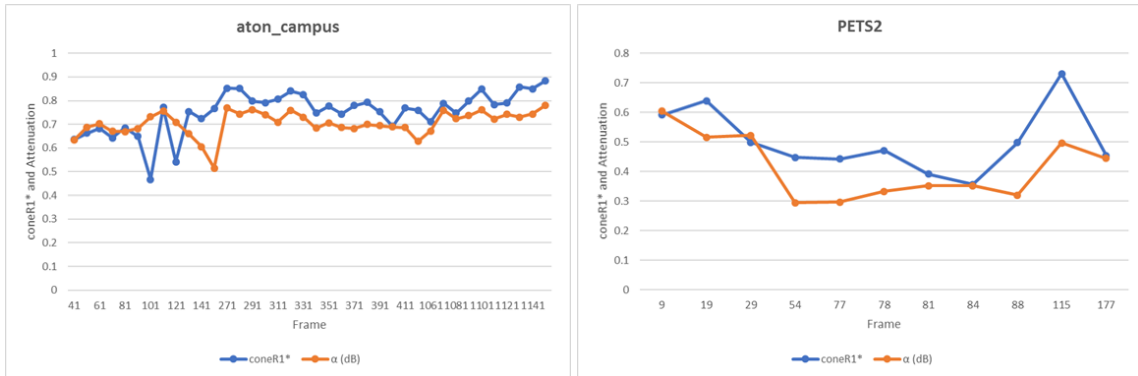
4.1.1 $coneRI^*$ and Average Attenuation

Both attenuation models (α_{dB} and $\alpha\%_\Delta$) were considered for correlation against the $coneRI^*$ values of a dataset. Correlation ρ_α is represented for both attenuation models as ρ_{dB} and $\rho\%_\Delta$ respectively. Results for both are illustrated in Figure 4.1 and Figure 4.2. Tables 4.1 and 4.2 present correlation coefficients for each dataset for α_{dB} and $\alpha\%_\Delta$.

Both Tables 4.1 and 4.2 demonstrate significant correlation between $coneRI^*$ and α , consistent across all datasets. To provide contrast, an arbitrary variable (number of normal SIFT features detected) has been correlated against $coneRI^*$ (Table 4.3). In Table 4.3, we observe positive and negative correlations, as well as strong and weak correlations. Significant correlations are observed, but are inconsistent. These tables show consistent positive α correlations across datasets. Strong and consistent correlation between the two sets implies that both α_{dB} and $\alpha\%_\Delta$ will provide a $coneRI'$ that will improve shadow removal across the



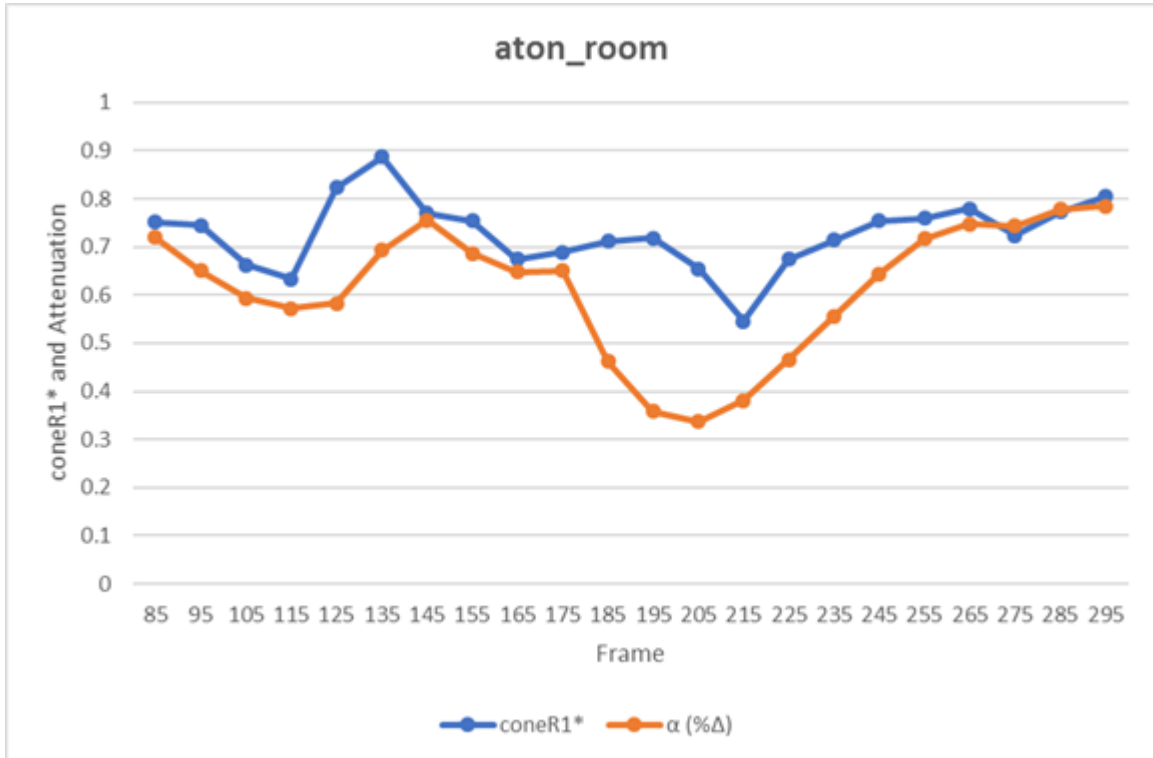
(a) aton_room



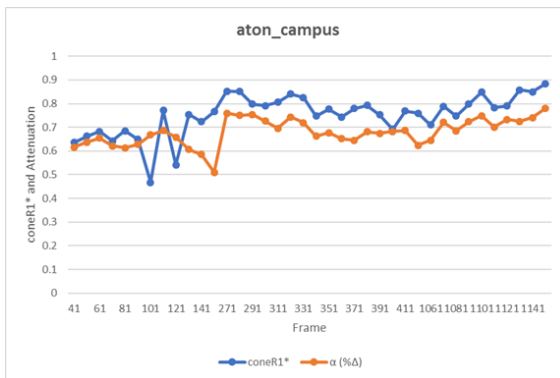
(b) aton_campus

(c) PETS2

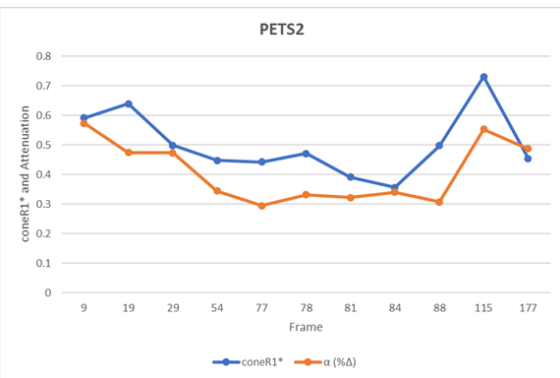
Figure 4.1: Correlation of α_{dB} (orange) and *coneR1** (blue) is observed across all datasets. Three are shown here. (All results can be found in the appendix)



(a) aton_room



(b) aton_campus



(c) PET2

Figure 4.2: Likewise, correlation of $\alpha_{\% \Delta}$ (orange) and *coneR1** (blue) is observed across all datasets with three shown here. (All results can be found in the appendix)

Table 4.3: Datasets and their *SIFT* correlations to *coneRI**.

Dataset	ρ_{SIFT}
PETS1	-0.057
PETS2	-0.727
aton_highway1	0.009
aton_highway3	0.350
aton_room	-0.079
aton_campus	0.218
aton_hallway	-0.201
aton_lab	0.046

selected datasets.

PETS1 is the primary outlier with a correlation coefficient of approximately 19% for both attenuation models. While both PETS2 and PETS1 experience illumination change within the extracted samples, PETS2 and *coneRI** have a correlation coefficient of approximately 74%. During the illumination change in PETS2, in which the average brightness of the entire scene decreases by 23%, observed attenuation proportionally decreases by 28%. We observe *coneRI** decreases by 37%. PETS1 experiences a similar illumination change (21%), and an attenuation change of 32%, but no significant corresponding fluctuation in *coneRI**. Illumination and parametric fluctuation was obtained by measuring these values at the beginning and end of the illumination change within the dataset, a range of 22 frames for PETS2, and 45 frames for PETS1. One possible explanation for this discrepancy is that because every pixel is darkened by roughly the same amount due to the illumination shift, the attenuation changes, while the normalized value *coneRI** does not. However, since this behavior is not evident in PETS2 as well, there are likely undiscovered factors influencing PETS1's poor correlation coefficient.

The results in Tables 4.1 and 4.2 indicate that some datasets benefit more from the α_{dB} model, while others have greater benefit from the $\alpha\%_{\Delta}$ model. While the correlation found using the two models are comparable, we use the $\alpha\%_{\Delta}$ model in Eqn. 3.14, when calculating the parameter *coneRI*'. This is because the $\alpha\%_{\Delta}$ model provides a closer fit to *coneRI**, in terms of the magnitude shift required , which is covered in detail in section

3.3.

4.1.2 Correlation Improvements

In sections 3.2.4 and 3.2.5, we discuss two indirect environmental properties that may be used to improve correlation: low-contrast SIFT keypoints and brightness calculation methods. We conduct sensitivity analysis on the two properties.

Low-contrast SIFT keypoints are analyzed within a frame and are used to produce a scaling factor that is applied to observed attenuation $\alpha_{\% \Delta}$. From this analysis we determine that the low-contrast scaling factor provides boosts to correlation in select datasets, while proving detrimental to others.

We also demonstrate that correlation (both ρ_{dB} and $\rho_{\% \Delta}$) are sensitive to varying brightness models, by contrasting their effects across datasets. We show quantifiable and predictable effects on the α_{dB} attenuation model, that indicate the HSP and Luma brightness models are most appropriate for outdoor datasets, while indoor datasets are not sensitive to varying brightness models. Similar analysis is performed regarding $\rho_{\% \Delta}$; however, the same trends (outdoor/indoor) are not observed, due to differences intrinsic to attenuation calculation.

Low-contrast SIFT Keypoints

Using Eqn. 3.12 defined in section 3.2.5, $SIFT_{fg/bg}$ is calculated per frame and multiplied against the observed average attenuation. $SIFT_{\%C}(f)$ represents the ratio of total low contrast SIFT features to normal SIFT features within a frame f .

$$SIFT_{fg/bg} = \frac{SIFT_{\%C}(fg)}{SIFT_{\%C}(bg)} \quad (4.2)$$

The result of the multiplication is stored in the variable α_{SIFT} , and a new correlation is calculated (ρ_{SIFT}). Figure 4.3 shows the multiplication's effect on the aton_highway1 dataset. Figure 4.4 and Table 4.4 detail the effects on correlation ($\rho_{\% \Delta}$) for each dataset.

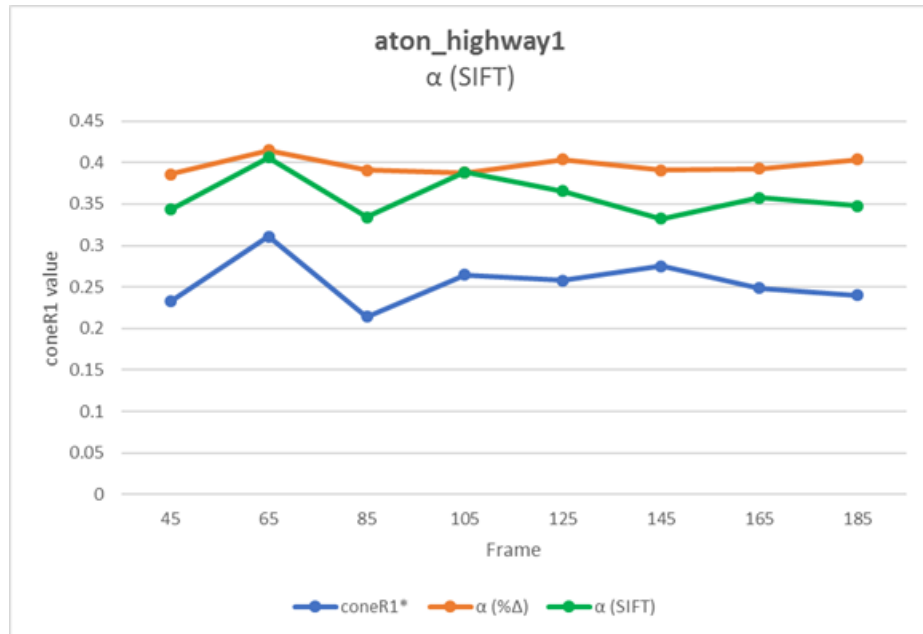


Figure 4.3: $SIFT_{fg/bg}$ multiplication's effect on correlation for the dataset aton_highway1. The observed attenuation $\alpha\%_{\Delta}$ (orange), is multiplied by the calculated $SIFT_{fg/bg}$ on a per frame basis. The resultant (α_{SIFT}), shown in green, represents a closer fit to $coneR1^*$ (blue).

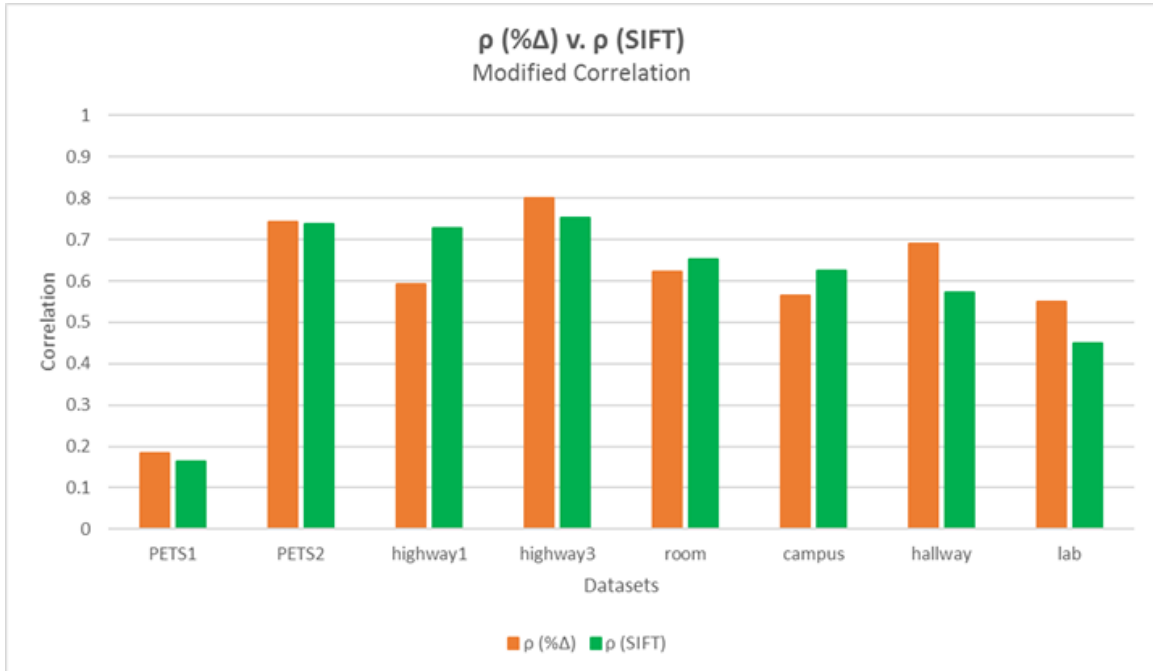


Figure 4.4: Original correlations, $\rho\%_{\Delta}$, (orange) are plotted against newly calculated correlations ρ_{SIFT} (green).

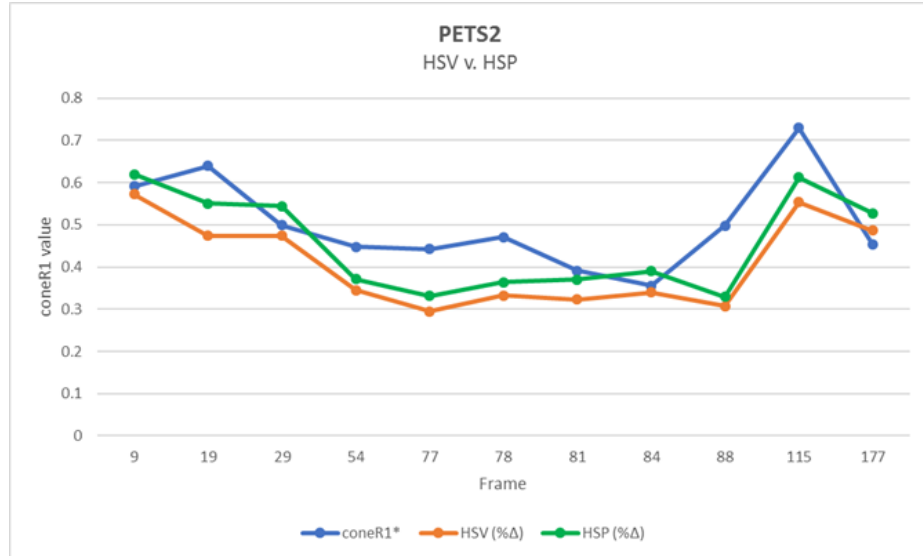
Table 4.4: Correlation shifts ($\rho_{\% \Delta}$) when $SIFT_{fg/bg}$ is multiplied against observed attenuation $\alpha_{\% \Delta}$.

Dataset	$\rho_{\% \Delta}$ Shift (%)
PETS1	-2.06
PETS2	-0.58
aton_highway1	+13.62
aton_highway3	-4.76
aton_room	+3.087
aton_campus	+6.06
aton_hallway	-11.78
aton_lab	-10.17

Table 4.4 shows that modulating $\alpha_{\% \Delta}$ by $SIFT_{fg/bg}$ produces inconsistent results. For aton_highway1, aton_room, and aton_campus, the operation produced favorable results. However, for all other datasets it produced unfavorable or negligible results. The datasets that had the greatest improvements, aton_highway1 and aton_campus, contain the darkest shadows. Similarly, the most negatively affected datasets, aton_hallway and aton_lab, have the faintest shadows. From this observation, we posit that there is a range of shadow brightness in which the saturation channel is affected enough (detailed in section 3.2.5) to be detectable as a low-contrast SIFT keypoint, and therefore that range benefits from analyzing low-contrast SIFT keypoints. This validates the assumption that low-contrast SIFT features, while not in direct correlation with *coneRI**, can provide indirect benefits by improving the existing correlation ($\rho_{\% \Delta}$), depending on the environment. Future work using low-contrast SIFT keypoints begins with determining this threshold.

Brightness Models - ρ_{dB} Attenuation Model

In addition to differing responses to attenuation models, datasets also respond uniquely to varying brightness models. Figure 4.5 illustrates how differing brightness models affect the correlation coefficient of attenuation. Table 4.5 enumerates the correlative changes experienced by each dataset when subjected to a range of brightness models. These results are illustrated in Figure 4.6.



(a) PETS2



(b) aton_lab

Figure 4.5: Example contrasting correlation improvements of the HSP model (green) against HSV (orange) and *coneR1** (blue).

Figure 4.6: Datasets and their correlations (y-axis) to $coneRI^*$ (α_{dB}) against Brightness models (x-axis).

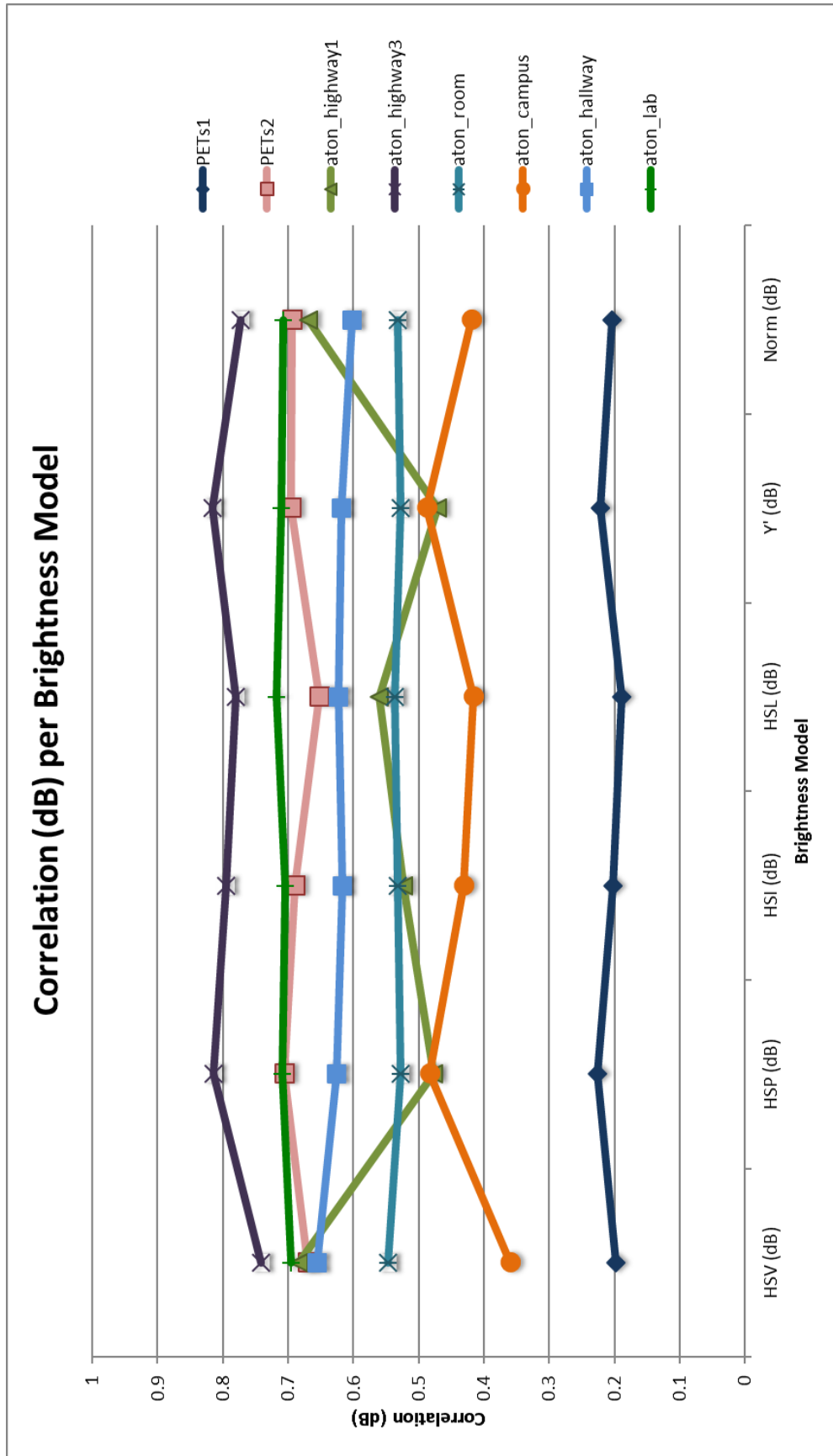
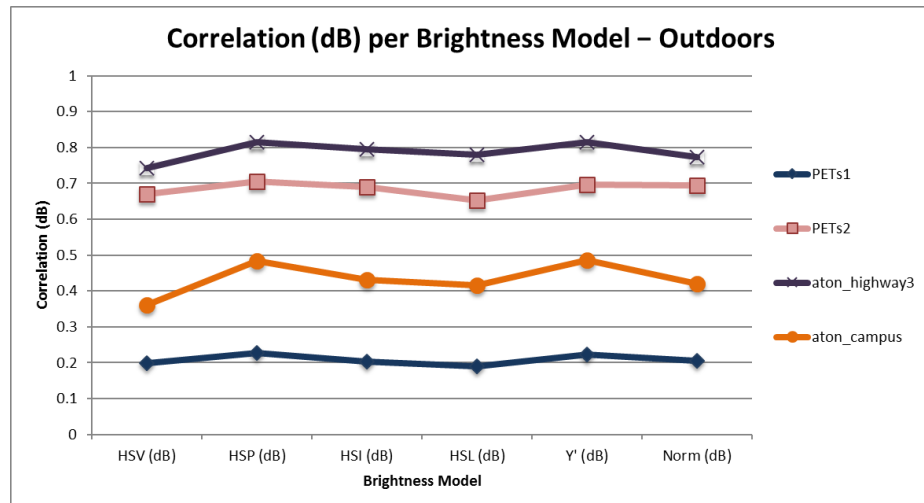


Table 4.5: Datasets and their correlations to $coneRI^*$ (α_{dB}) against Brightness models. Outdoor (top) and Indoor (bottom) scenes are grouped appropriately.

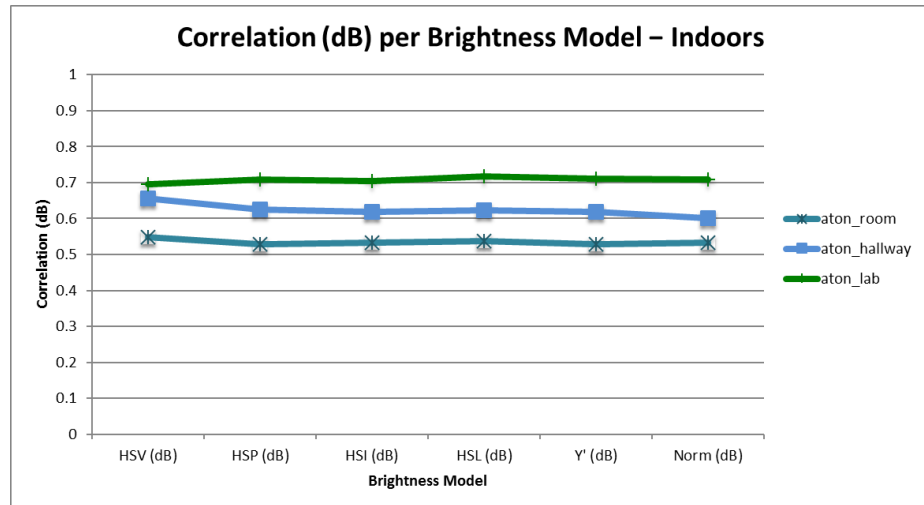
Dataset	HSV ρ_{dB}	HSP ρ_{dB}	HSI ρ_{dB}	HSL ρ_{dB}	Y' ρ_{dB}	Norm ρ_{dB}
PETS1	0.199	0.227	0.202	0.190	0.222	0.205
PETS2	0.671	0.710	0.690	0.653	0.696	0.695
aton_highway1	0.684	0.477	0.524	0.560	0.471	0.669
aton_highway3	0.742	0.814	0.795	0.780	0.816	0.773
aton_campus	0.359	0.483	0.430	0.416	0.487	0.420
aton_room	0.548	0.528	0.532	0.536	0.527	0.532
aton_hallway	0.656	0.625	0.617	0.622	0.618	0.601
aton_lab	0.695	0.710	0.705	0.717	0.710	0.708

Two distinct response trends are observed in Figure 4.6. These trends are shown in Figure 4.7: outdoor datasets (PETS1, PETS2, aton_highway3, and aton_campus) share a similar response to the various brightness models, while indoor datasets (aton_room, aton_hallway, and aton_lab) also share a similar response. Table 4.5 indicates that ρ_{dB} is sensitive to change in brightness models among outdoor datasets (Figure 4.7(a)), with HSP and Luma (Y') consistently providing the highest correlations. Indoor datasets (Figure 4.7(b)) exhibit negligible sensitivity to brightness model change for ρ_{dB} attenuation. From this indication, we deduce that utilizing either the HSP or Luma brightness model improves correlation (ρ_{dB}) for outdoor scenes.

Furthermore, we can predict when to utilize the HSP/Luma models for better (dB) correlation, by measuring the *red-green color bias* (defined below) corresponding to shadow regions in a dataset. The difference in brightness models can be primarily characterized by their individual treatments of color content in a pixel, i.e., both Y' and HSP weight the channels of an RGB image by scaling factors relevant to human perception, while HSV simply takes the largest color channel value as the brightness. We differentiate between the datasets by measuring the average red-green color bias (β_p^{RG} , for pixel p) present in shadow pixels. To determine color bias, we use the color shift (Δ_{RGB}) from a foreground shadow pixel to an illuminated background pixel. We define the red-green color bias as



(a)



(b)

Figure 4.7: Outdoor datasets (a) share a common response to varying brightness models. In contrast, indoor datasets (b) share a insensitivity to varying brightness models

Table 4.6: Red-green bias for each dataset. β^{RG} represents the average of the β_f^{RG} for each frame in a dataset. Outdoor (top) and Indoor (bottom) scenes are grouped together.

Dataset	β^{RG}
PETS1	15.03
PETS2	7.57
aton_highway1	6.69
aton_highway3	2.56
aton_campus	3.32
aton_room	1.64
aton_hallway	-0.26
aton_lab	0.35

the observed blue color shift of a foreground shadow pixel p subtracted from the mean of observed red and green color shifts (Eqn. 4.3).

$$\beta_p^{RG} = \frac{\Delta R_p + \Delta G_p}{2} - \Delta B_p \quad (4.3)$$

This operation is performed on each foreground pixel that is darker than its corresponding background pixel, and averaged into β_{RG}^f , the average red-green color bias per frame. The values of β^{RG} are contingent on the representation of the RGB channels in an image. In our study, each channel has a range of (0, 255). As seen in Table 4.6, outdoor datasets display consistently higher β^{RG} values.

The exception to this grouping of outdoor and indoor datasets is aton_highway1, an outdoor dataset that has a response reciprocal to that of most outdoor environments. Figure 4.8 illustrates the mirrored nature of aton_highway1's response. aton_highway1 contains the darkest cast shadows in relation to its background model. The relative low points, HSP and Luma, both attempt to weight brightness according to color information. The applied weights are the only differing factor in the HSP and Norm methods. Therefore, we conclude that the consideration of color shift is a detriment to aton_highway1's ρ_{dB} correlations.

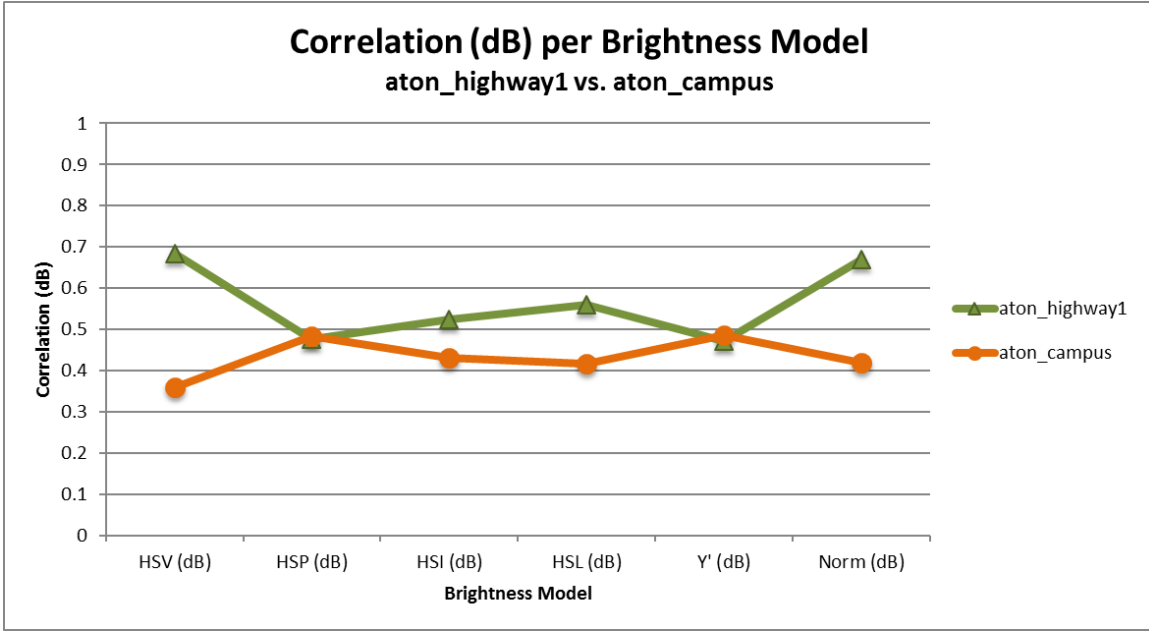


Figure 4.8: aton_highway1's response to various brightness models behaves opposite to other outdoor datasets.

Brightness Models - $\rho_{\% \Delta}$ Attenuation Model

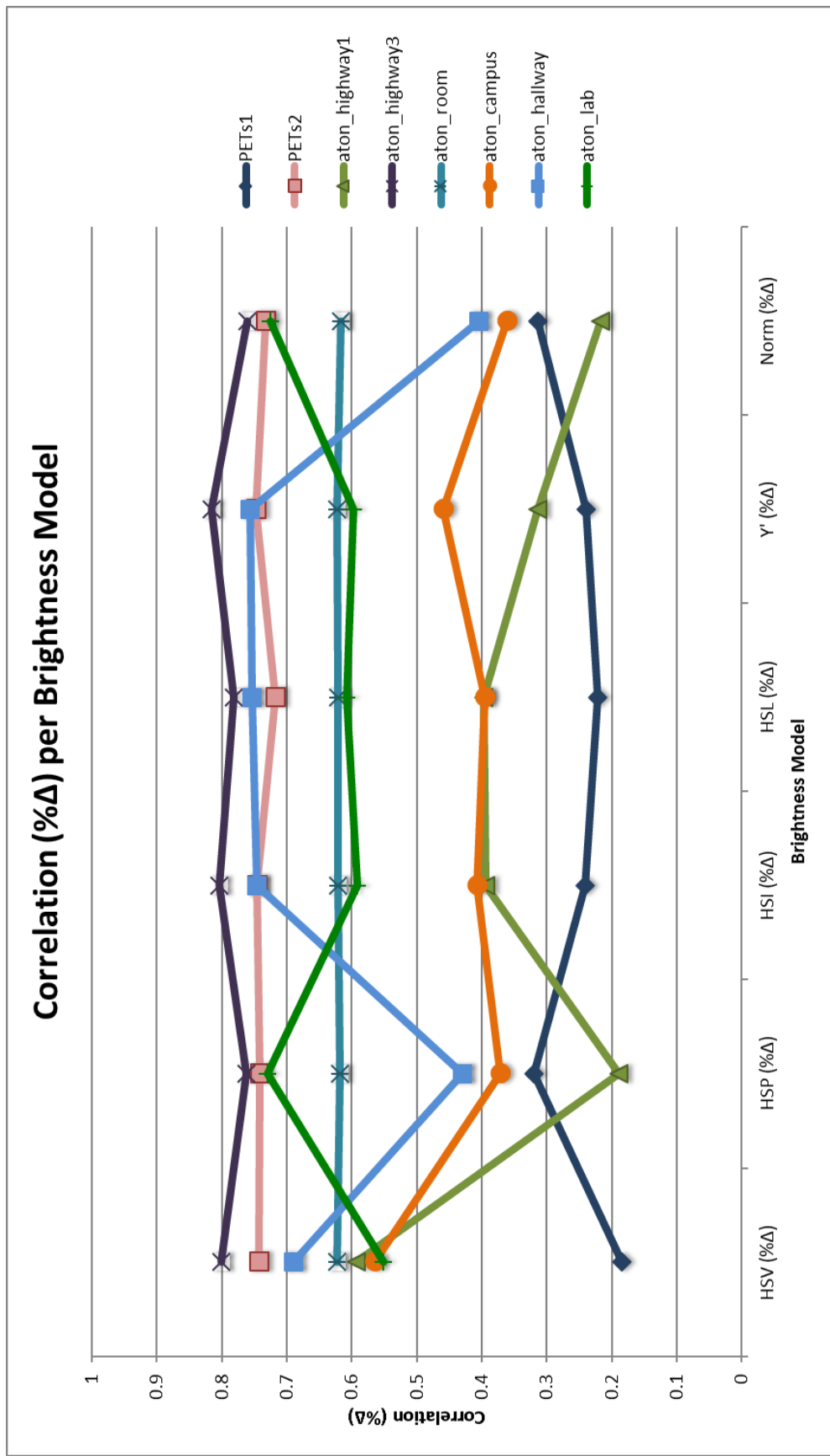
Results indicating correlations ($\rho_{\% \Delta}$) per brightness model are enumerated in Table 4.7. These results are illustrated in Figure 4.9.

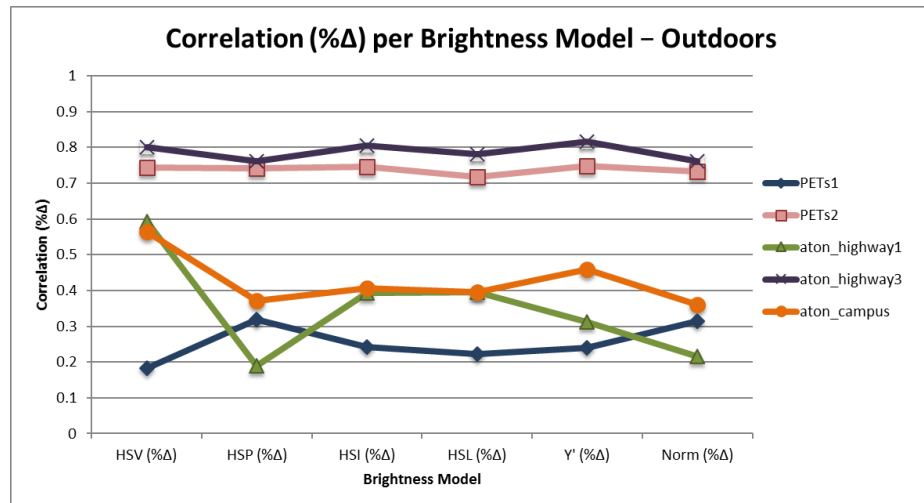
It is important to note that Figure 4.9 does not exhibit the trends indicated by the α_{dB} model in Figure 4.6. The datasets are separated into outdoor/indoor datasets in Figure

Table 4.7: Datasets and their correlations to *coneRI** ($\rho_{\% \Delta}$) against Brightness models. Outdoor (top) and Indoor (bottom) scenes are grouped appropriately.

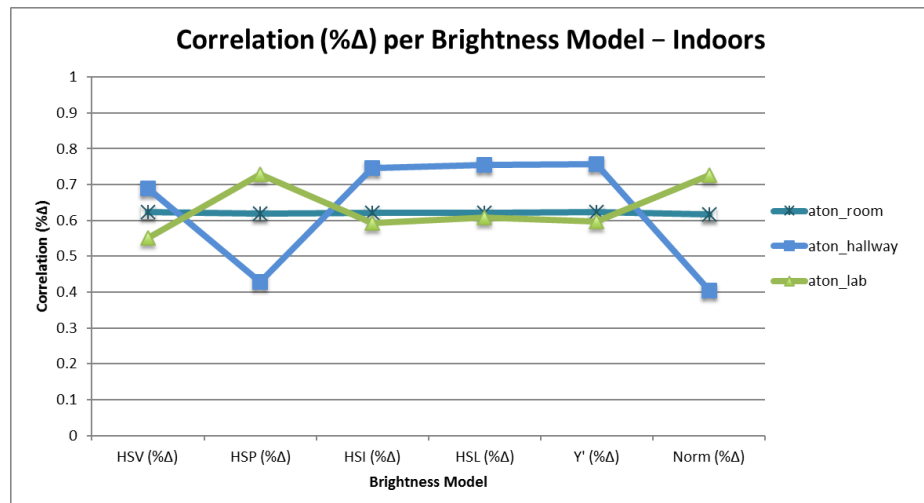
Dataset	HSV $\rho_{\% \Delta}$	HSP $\rho_{\% \Delta}$	HSI $\rho_{\% \Delta}$	HSL $\rho_{\% \Delta}$	Y' $\rho_{\% \Delta}$	Norm $\rho_{\% \Delta}$
PETS1	0.183	0.320	0.241	0.222	0.239	0.314
PETS2	0.743	0.741	0.746	0.717	0.747	0.732
aton_highway1	0.592	0.189	0.393	0.396	0.313	0.216
aton_highway3	0.801	0.761	0.804	0.781	0.815	0.760
aton_campus	0.564	0.371	0.407	0.395	0.459	0.361
aton_room	0.622	0.618	0.621	0.621	0.623	0.616
aton_hallway	0.689	0.429	0.746	0.754	0.756	0.404
aton_lab	0.551	0.729	0.592	0.608	0.597	0.725

Figure 4.9: Datasets and their correlations (y-axis) to $coneRJ^*$ ($\alpha_{\% \Delta}$) against Brightness models (x-axis).





(a)



(b)

Figure 4.10: (a) Outdoor datasets. (b) Indoor datasets.

4.10. Some datasets, such as PETS1, PETS2, aton_highway3, and aton_room, demonstrate similar responses to those observed in Figure 4.6. However, aton_lab, aton_hallway, and aton_campus behave erratically in comparison to their corresponding α_{dB} responses. The disparity between the two brightness responses can be attributed to the vectorization of the $\alpha\%_\Delta$ model, which calculates the brightness of the vector between a foreground and background pixel. For example, a pixel p_1 is represented by the RGB values (25, 50, 75), and a second pixel p_2 is (75, 50, 25). Using the HSV brightness model, we calculate the brightness of each pixel to be 75. The α_{dB} model results in 1.0, or no attenuation. The $\alpha\%_\Delta$ model calculates the brightness change of the difference, $p_2 - p_1 = (50, 0, -50)$. Using the HSV model, $\alpha\%_\Delta$ reports a brightness shift of 50 units, with a resulting attenuation of $50/75 = 0.66$. We conclude the attenuation model $\alpha\%_\Delta$ is not predictably sensitive to a change in brightness model.

4.2 Parameter Model Results

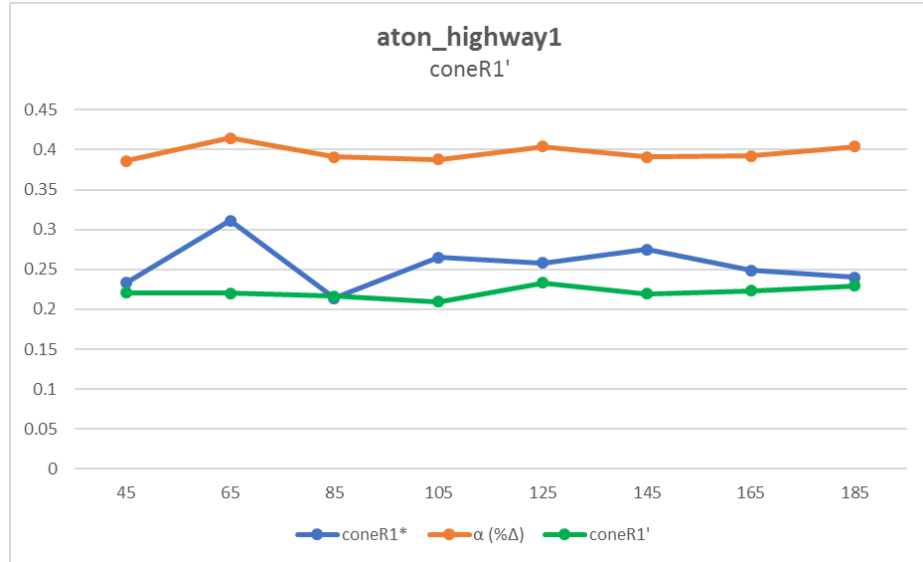
The primary challenge in adapting observed average attenuation into an arbitrary model for shadow removal improvement lies in understanding the necessary translation between observed attenuation and $coneRI^*$. Utilizing the formulae specified in section 3.3, a coarse-grained model is developed.

Applied to an arbitrary frame, attenuation ($\alpha\%_\Delta$) and color magnitude shift (Δ RGB) are analyzed and used to create the necessary translation ($shift_\alpha$). This analysis is performed on each brightness model, seen in Figure 4.11.

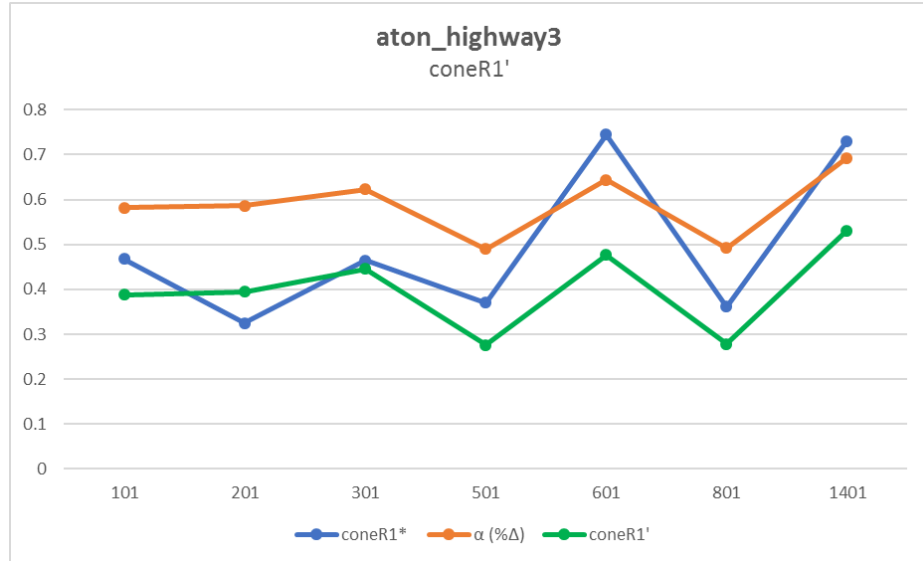
Using Δ RGB, $\alpha\%_\Delta$, and $shift_\alpha$, we calculate the adapted variable $coneRI'$. Illustrated results of this model are displayed in Figure 4.12 for the datasets aton_highway1 and aton_highway3. The resultant of the model ($coneRI'$), shown in orange, retains correlative properties observed prior while providing a reasonable estimate for required translation.



Figure 4.11: For each brightness model, ΔRGB is plotted against $\text{shift}_{\text{req.}}$. The general model for each brightness calculation is formed through a best-fit logarithm.



(a) aton_highway1



(b) aton_highway3

Figure 4.12: Adaptively tuned *coneR1'* parameter (green) charted against *coneR1** (blue) and average attenuation ($\alpha_{\% \Delta}$) (orange). All results can be found in the appendix.

4.2.1 Analysis

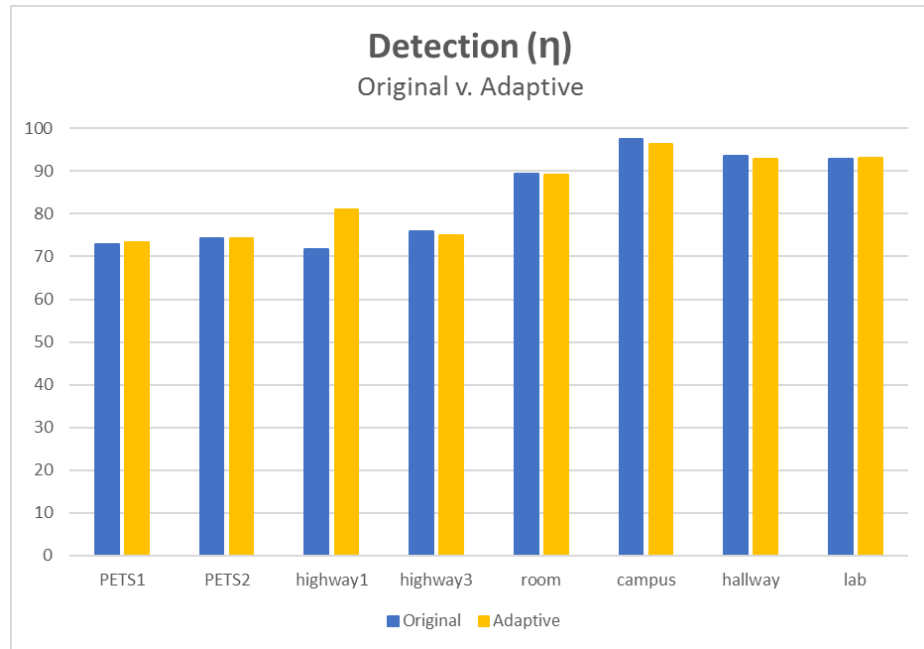
Figure 4.13 illustrates the resulting detection and discrimination rates of shadow removal using the adapted parameter $coneRI'$, contrasting the generated results (orange) with detection/discrimination determined via the original naive method (blue). Detection and discrimination are averaged per frame for each dataset. Quantitative results are shown in Tables 4.8 and 4.9.

Results indicate that for a majority of datasets, small amounts of shadow detection accuracy is sacrificed for disproportionate increases in shadow discrimination. Figure 4.14 qualitatively illustrates shadow removal improvements using the adaptive method for datasets aton_campus and aton_room.

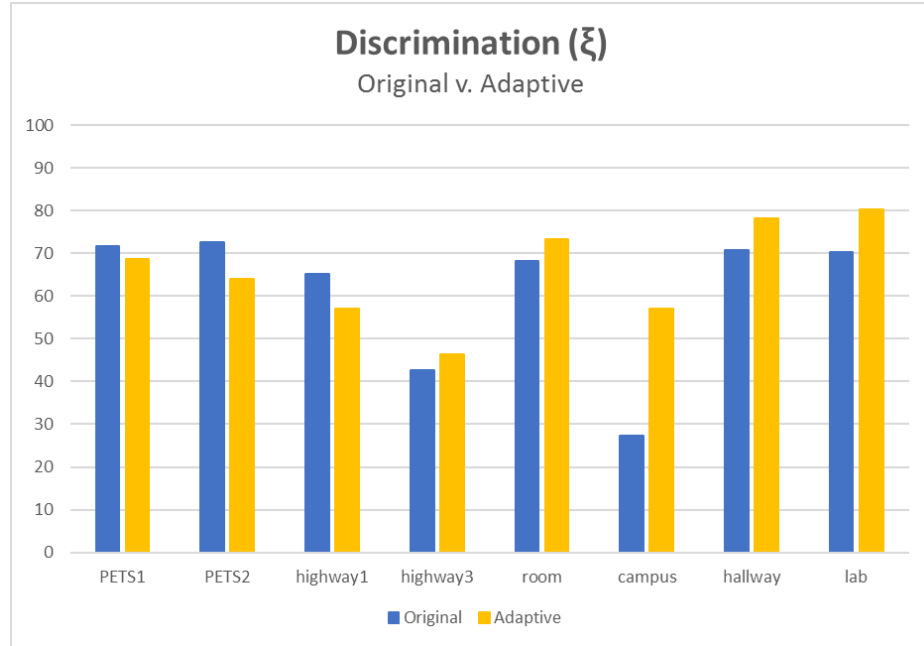
aton_highway1 proved anomalous, trading in nearly equal part detection for discrimination, arriving at a net modest positive of 1.2%. We hypothesize that is because aton_highway1 has the darkest cast shadows. Furthermore, aton_highway1 attenuates non-linearly (as expected of an outdoor scene), yet appears desaturated. The combination of the strong shadows and the low saturation of the frame allows a larger population of candidate shadows pixels to be gathered. Due to these conditions, foreground *object* pixels are more likely to appear identical to shadow pixels, in both color information and relative distance from its background pixel. The confluence of these scene characteristics renders aton_highway1

Table 4.8: Average detection (η) calculated from the adapted $coneRI'$ (left). η is compared against original naive detection ($coneRI = 0.3$). The difference (right) is represented as a percentage.

Dataset	η (%)	+/- (%)
PETS1	73.28	+0.459
PETS2	74.34	+0.056
aton_highway1	80.99	+9.353
aton_highway3	74.88	-1.154
aton_room	89.10	-0.264
aton_campus	96.46	-0.976
aton_hallway	92.91	-0.660
aton_lab	93.12	+0.192



(a)



(b)

Figure 4.13: Average detection (a) and average discrimination (b) calculated using the adaptive parameter model, for each dataset.

Figure 4.14: Qualitative shadow removal improvement. (a - c) feature the atom_campus dataset, and (d - f) feature the atom_room datasets.

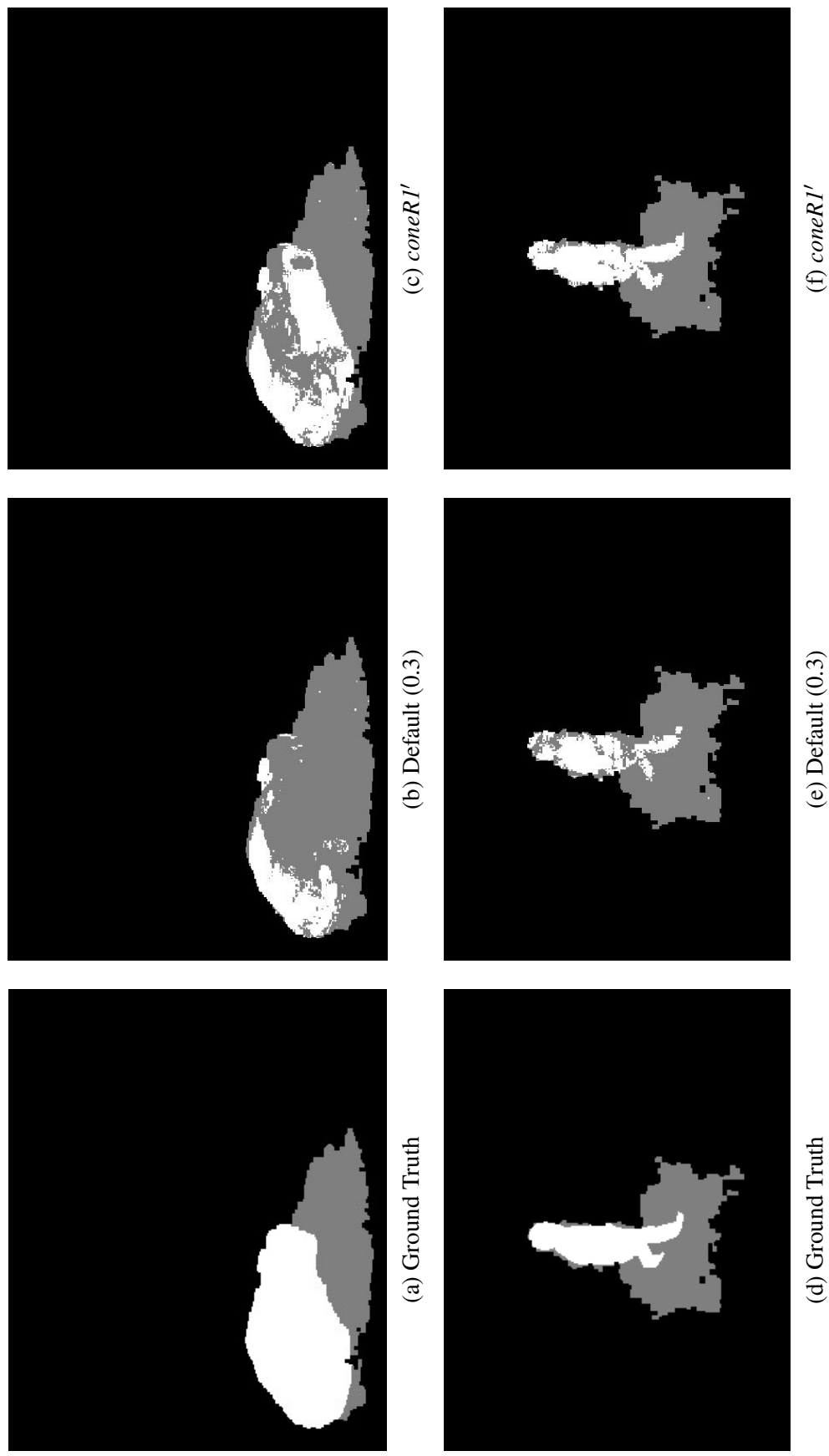


Table 4.9: Average discrimination (ξ) calculated from the adapted $coneRI'$ (left). ξ is compared against original naive discrimination ($coneRI = 0.3$). The difference (right) is represented as a percentage.

Dataset	ξ (%)	+/- (%)
PETS1	68.61	-3.176
PETS2	64.04	-8.458
aton_highway1	57.05	-8.172
aton_highway3	46.35	+3.802
aton_room	73.36	+5.278
aton_campus	57.05	+29.67
aton_hallway	78.22	+7.549
aton_lab	80.16	+9.787

less predictable than other datasets.

PETS1 and PETS2 also do not conform to the upward trends seen in the majority of datasets. In the case of PETS1, the low correlation coefficient infers the poor detection/discrimination observed. More interestingly, PETS2 experiences the same degradation of performance as PETS1, but has a much stronger correlation coefficient, seen in Table 4.2. This decoupling of correlation and accuracy stems from the necessary translation of the observed average attenuation by the generalized adaptation model. This is illustrated in Figure 4.15. The model overcompensates for observed color shift (ΔRGB) in PETS2, because of the illumination change in the dataset. The misrepresentation of attenuation (and thereby ΔRGB) of cast shadows in PETS2 results in the unnecessary ‘downward’translation, impacting PETS2’s shadow discrimination accuracy. This may be solved using techniques for rapid illumination change compensation [49], explained in section 5.1.

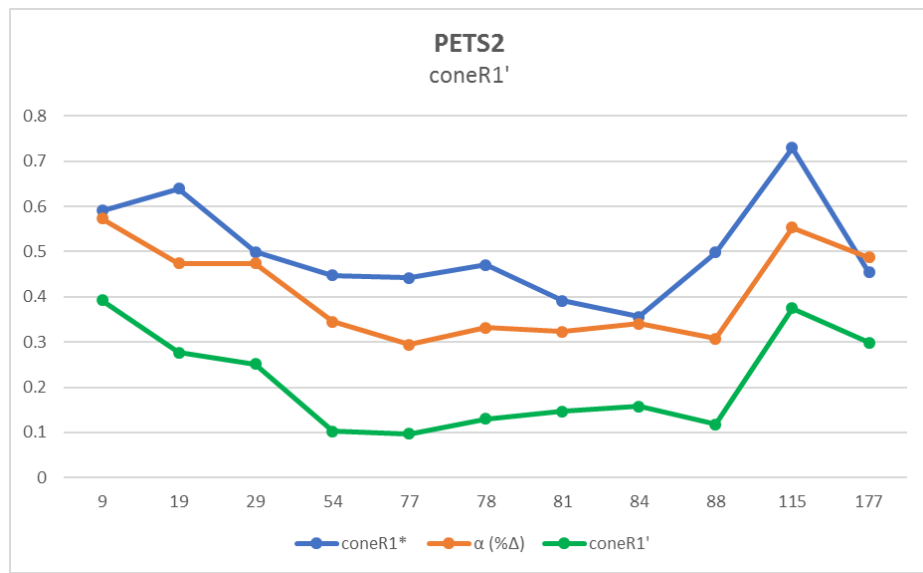


Figure 4.15: For PETS2, the adapted parameter *coneR1'* (green) is erroneously shifted downwards. The originally observed attenuation ($\alpha\% \Delta$) is shown in orange.

CHAPTER 5

CONCLUSION AND FUTURE WORK

We have demonstrated the capability of an adaptive model to intelligently adapt the parameters of a shadow removal algorithm, using observed environmental features. This was completed through the construction of a proof-of-concept which adapted the parameter *coneRI* of the Physical shadow removal algorithm, according to the average brightness attenuation (α) observed between a shadow region and its corresponding background. The adaptive model was shown to positively affect the discrimination (ξ) of foreground object pixels from shadow pixels for 6 out of the 8 datasets, with average improvements ranging from 4% to 29% greater accuracy (when compared to the naive model). The adaptive model was shown to behave poorly with regards to rapid illumination change (PETS1, PETS2), decreasing the shadow discrimination by 3% and 8% during these periods. The adaptive model marginally increases shadow detection (η) in three datasets (PETS1, PETS2, aton_highway1) by 0.5% to 9%, while the remaining datasets trade fractional amounts (< 0.5%) of shadow detection for the previously observed increases in discrimination.

We have developed tools to facilitate the construction of the adaptive model, including a graphical interface for rapidly modifying a shadow removal algorithm's parameters, and an iterative process designed to automatically calculate the optimal value of a given parameter, i.e., the value that yields the highest combination of shadow detection and discrimination for a frame. Using this framework, we provided the ability to quickly assess an algorithm's sensitivity to its mutable parameters, both qualitatively, using the interactive graphical tools, and quantitatively, using the iterative process.

In order to construct the adaptive model for Physical shadow removal (and *coneRI*), we correlated shadow brightness attenuation (α) to the optimal parameter value *coneRI**¹, determined empirically through the interactive parameter exploration. The correlation (ρ_α)

ranges from 18% to 80%. We improve correlation by evaluating two models of attenuation, α_{dB} and $\alpha\%_\Delta$. The adaptive model is based on the $\alpha\%_\Delta$ model, because it provides a better fit to *coneR1**.

We also presented two methods to affect the correlation ($\rho\%_\Delta$). The first of these, the measurement of low-contrast SIFT features in a scene, demonstrates changes in correlation (ρ_α) ranging from -12% to 13%. Varying the brightness model (HSV, HSP, HSI, HSL, Y', and Norm) used in calculating attenuation produced a wide range of correlation changes for both $\alpha\%_\Delta$ and α_{dB} . For α_{dB} , we demonstrate the ability to select the best-suited brightness model based on the red-green bias we calculate for dark pixels in a scene, which divide the datasets into outdoor and indoor environments. Variation of brightness calculation methods did not produce similar patterns for $\alpha\%_\Delta$.

We show (by way of proof-of-concept) that an adaptive model based on environmental properties can increase the portability of shadow removal algorithms, by automatically calibrating an algorithm to an environment. The implemented proof-of-concept is performed on the Physical model for shadow removal, a method that employs unsupervised machine-learning to learn the appearance of a shadow pixel over time. We demonstrate that an adaptive model can still increase the efficacy of shadow removal by tuning the parameters, for even an inherently adaptive shadow removal algorithm. The adaptive model is flexible enough to continuously adapt an algorithm over long periods of time, providing a scalable solution without relying on hard-coding thresholds and parameters.

5.1 Future Work

5.1.1 Modeling Low-contrast SIFT Keypoints

Given the correlation sensitivity shown with regard to $SIFT_{fg/bg}$, it is apparent that a more sophisticated model is required for the representation of low-contrast SIFT features in an image. We believe there are improvements to be made to properly model the low-contrast structural changes seen in shadow regions. One such improvement would be restricting

the observed low-contrast features to those found within identified foreground objects, eliminating false positives, i.e., low-contrast features existing outside of shadow regions (primarily caused by pixel-level noise).

5.1.2 Rapid Illumination Change Compensation

The presented adaptive model overcompensates for rapid illumination change, hampering shadow detection and discrimination. The problematic illumination changes are exaggerated by a background model that has not adapted to properly represent the new scene brightness. Bales et al.'s BigBackground is a process for illumination compensation that utilizes stable background features to locally estimate illumination changes for an entire scene. By utilizing BigBackground, we can compensate for the sluggish background model, and realistically represent the exaggerated attenuation between shadow and background.

5.1.3 Classifying Indoor/Outdoor Scenes

While implementing various brightness calculation methods, we found (for the α_{dB} model of attenuation) that we could assign an ideal brightness model to a scene based on whether or not it was an indoor or outdoor environment. We quantified the red-green bias of possible shadow pixels, and used the measured bias to classify a scene as outdoor or indoor. Further verification is required for this claim. Repeating these bias calculations on a wide variety of datasets will validate the spectral-illuminant theory supported the supposition. Further work in this area allows us to study the multi-illuminant properties of outdoor shadows vs. indoor shadows in more depth, which can in turn provide more accurate classification.

Appendices

APPENDIX A
DEFAULT DETECTION AND DISCRIMINATION

Table A.1: PETS1
 Detection (η) and Discrimination (ξ) for each shadow removal method (default parameters)

frame	C - η	C - ξ	P - η	P - ξ	G - η	G - ξ	SRT - η	SRT - ξ	LRT - η	LRT - ξ
44	82.3629	75.7402	69.2827	75.9517	76.8776	91.0876	14.0084	92.9003	32.6582	98.4592
49	67.6524	70.5788	53.1080	83.4889	80.9897	91.5978	3.3796	99.7866	11.5269	100.0000
67	77.9240	67.8265	65.6433	67.6909	90.3509	89.2454	8.3333	90.8269	0.0000	96.2494
73	98.0328	61.8231	66.2295	64.7059	66.2295	52.2400	25.2459	81.3011	0.0000	97.4289
77	72.4427	69.9954	79.6947	76.0390	61.6031	82.1130	5.4198	97.5186	57.9389	94.1848
82	75.2788	69.7977	78.6989	73.8816	75.7993	59.8849	39.7026	82.6434	50.3346	93.9391
85	71.4528	63.2595	68.8791	66.9706	63.0545	59.8664	84.1856	50.4082	32.3061	95.5784
91	84.2899	64.9629	71.5467	68.4584	64.3482	89.5301	32.9280	87.0404	30.7393	87.0899
107	25.1656	83.2055	63.1347	80.6748	51.8764	97.3160	52.3179	81.8252	0.0000	100.0000
124	28.0528	78.8076	79.3729	66.0321	65.8416	95.2405	17.3267	81.9639	45.3795	78.7074
139	93.5268	60.4111	89.7321	57.1618	94.1964	91.1141	2.9018	98.9390	52.4554	79.5756
167	15.1067	89.4986	88.5057	80.3523	80.6240	91.6667	58.9491	85.9756	60.4269	80.6911

Table A.2: PETS2
 Detection (η) and Discrimination (ξ) for each shadow removal method (default parameters)

frame	C - η	C - ξ	P - η	P - ξ	G - η	G - ξ	SRT - η	SRT - ξ	LRT - η	LRT - ξ
00009	72.8181	78.0194	68.2878	52.6612	72.5516	94.5496	70.0866	76.5609	26.5823	100.0000
00019	37.3047	75.5725	46.8750	67.0760	0.0000	100.0000	44.7266	78.2609	0.0000	93.7604
00029	50.7905	63.9494	44.2688	66.8265	0.0000	100.0000	64.2292	84.9172	3.1621	84.0453
00054	77.8761	69.7446	99.1150	66.1100	0.0000	100.0000	69.0265	94.9902	0.0000	100.0000
00077	57.9767	77.3554	99.3515	68.5402	0.2594	34.0477	74.8379	91.9127	83.5279	89.1225
00078	74.1440	77.3310	100.0000	63.8533	0.0000	100.0000	8.9728	99.0278	93.5065	96.9951
00081	74.2164	75.8822	99.0900	56.3435	0.0000	94.7242	7.7856	96.6769	91.4055	76.2019
00084	78.4682	75.8360	99.2052	53.9914	0.0000	100.0000	69.0751	83.8008	89.3064	90.3452
00088	21.7105	70.8188	100.0000	58.9431	0.0000	83.7398	0.0000	100.0000	78.2895	78.7747
00115	15.1329	56.5330	25.7669	61.8370	0.0000	100.0000	23.9264	85.4463	0.0000	100.0000
00177	84.5038	66.9796	73.6506	63.6037	0.0000	100.0000	45.6761	95.9648	27.7423	85.6173

Table A.3: aton_highway1
 Detection (η) and Discrimination (ξ) for each shadow removal method (default parameters)

frame	C - η	C - ξ	P - η	P - ξ	G - η	G - ξ	SRT - η	SRT - ξ	LRT - η	LRT - ξ
0045	75.4613	69.9373	75.5500	68.9675	79.0454	87.1192	27.7857	88.2145	83.5167	93.0405
0065	87.0106	66.1312	67.1580	65.4284	63.5191	78.4137	0.2303	98.3936	68.5398	91.8340
0085	75.3393	71.7385	73.1796	57.4586	68.6852	80.9808	4.9759	98.7355	77.4259	92.8961
0105	89.2308	76.0680	82.7473	69.9272	60.4396	78.6650	1.0989	94.0777	84.0659	84.7087
0125	77.3199	62.2002	69.1618	63.3436	61.4522	85.8059	24.3622	96.1517	80.2635	82.1528
0145	78.5626	57.9551	72.2989	64.8861	51.7468	59.1013	16.8586	91.7851	81.8087	89.3398
0165	75.0502	73.0680	67.2983	63.0572	68.1883	64.7848	15.9345	94.7709	74.6483	90.2977
0185	70.3516	69.2308	65.7503	67.0521	71.5381	75.5757	15.4536	93.6742	72.9706	91.1992

Table A.4: aton_highway3
 Detection (η) and Discrimination (ξ) for each shadow removal method (default parameters)

frame	C - η	C - ξ	P - η	P - ξ	G - η	G - ξ	SRT - η	SRT - ξ	LRT - η	LRT - ξ
0101	76.2500	53.0201	79.3750	24.1611	38.7500	95.3020	1.8750	95.5257	21.2500	80.3132
0201	62.7848	57.9273	74.9367	31.5545	46.3291	92.7301	0.0000	90.6419	45.0633	89.2498
0301	84.8361	55.9625	75.4098	35.4344	10.6557	98.0409	13.9344	81.6865	0.0000	98.0409
0501	26.6756	83.3521	86.5952	16.4976	77.7480	49.5303	2.1448	95.3025	68.2306	87.9369
0601	93.6441	41.8327	85.5932	31.4741	19.4915	80.8765	5.5085	90.8367	0.0000	100.0000
0801	34.2745	62.7775	81.7255	21.2777	33.5686	76.9626	8.6275	87.6827	68.3922	76.6919
1401	97.7778	25.1748	80.0000	40.5594	0.0000	100.0000	0.0000	98.6014	0.0000	100.0000

Table A.5: aton_room
 Detection (η) and Discrimination (ξ) for each shadow removal method (default parameters)

frame	C - η	C - ξ	P - η	P - ξ	G - η	G - ξ	SRT - η	SRT - ξ	LRT - η	LRT - ξ
0085	92.4157	54.0123	98.3146	40.4321	75.5618	8.0247	75.2809	84.2593	84.8315	96.9136
0095	93.9813	73.1268	96.2506	65.4899	55.2047	15.7061	93.1919	38.2565	86.7785	96.4697
0105	91.3198	72.2555	91.7626	73.9521	69.8849	78.9421	88.4854	64.6707	70.5049	96.8064
0115	92.3288	76.0705	93.0137	82.3678	56.4384	100.0000	88.6301	94.3325	72.7397	100.0000
0125	94.1653	71.5789	89.9514	77.7444	45.3809	74.5865	81.0373	85.4135	74.8784	99.5489
0135	97.5723	60.6419	96.4162	63.5135	66.0116	48.3108	87.6301	82.9392	86.8208	96.2838
0145	97.2332	59.8446	96.8379	65.8031	68.2806	92.7461	87.3518	95.8549	94.0711	89.8964
0155	96.1783	69.6538	94.9045	73.3198	53.1847	10.7943	82.5902	98.1670	93.3121	95.1120
0165	97.6216	62.2951	93.8378	69.0015	49.0811	19.6721	80.4324	92.5484	87.6757	89.4188
0175	96.0133	65.3451	93.6877	70.1909	85.6035	59.6182	81.0631	93.9794	89.3688	97.5037
0185	93.8095	65.6307	82.3810	73.4918	56.6667	39.3053	53.3333	95.0640	51.9048	98.5375
0195	81.4815	63.3010	61.1111	70.6796	53.7037	51.0680	29.6296	99.8058	16.6667	86.4078
0205	77.4194	65.9091	54.8387	70.8333	0.0000	100.0000	0.0000	96.0227	0.0000	100.0000
0215	70.6522	66.4908	52.1739	69.1293	33.6957	82.5858	45.6522	77.0449	60.8696	65.8311
0225	87.1875	67.6622	86.2500	63.3368	35.6250	100.0000	87.8125	70.1339	83.1250	75.4892
0235	95.5649	80.9748	95.0370	72.4843	31.8902	100.0000	92.9250	56.7610	90.9187	96.0692
0245	97.6648	75.2018	97.5610	64.5329	36.0664	13.9562	96.5750	41.5802	93.0462	97.6932
0255	98.1132	65.1961	99.0716	64.8039	86.5229	88.1373	98.6822	69.7059	98.1731	96.0294
0265	98.7066	56.8959	99.3193	59.8428	61.3569	83.8114	99.0243	42.4361	96.4148	95.1670
0275	97.5761	60.7713	98.8947	63.1206	88.7919	56.9592	97.2659	55.6738	93.5621	98.5372
0285	99.3210	62.9472	99.4989	67.3765	49.5797	87.7342	99.1917	60.4770	97.3327	96.8484
0295	92.6645	63.8510	99.0235	62.1911	23.5178	95.9425	93.8503	38.6942	89.3048	92.6226

Table A.6: aton_campus (pt. 1 of 2)

Detection (η) and Discrimination (ξ) for each shadow removal method (default parameters)

frame	C - η	C - ξ	P - η	P - ξ	G - η	G - ξ	SRT - η	SRT - ξ	LRT - η	LRT - ξ
0041	47.7791	48.8414	100.0000	21.1390	84.9940	82.4421	80.3121	99.9109	91.4766	99.5544
0051	8.7943	45.1419	99.9291	11.5025	9.4563	82.0701	58.5579	94.1235	89.3617	96.9115
0061	10.8374	60.7709	99.9034	28.2903	52.3671	36.3931	33.4944	94.9531	89.6296	95.6708
0071	31.4183	58.8547	99.0625	27.6341	81.9231	15.6750	26.5865	93.4619	41.9471	50.0235
0081	52.0435	56.4906	96.9347	27.0500	70.4351	20.7626	71.3579	66.7822	60.6460	44.3701
0091	87.6254	59.4496	98.6622	34.2341	63.0769	46.2865	79.1304	62.5166	77.2575	71.2202
0101	90.8602	66.2142	100.0000	39.3414	47.3118	16.2142	68.9964	67.6722	84.0502	76.2192
0111	83.6096	75.3583	97.0534	52.3762	60.2210	37.1637	73.1123	77.2944	93.0018	79.0546
0121	85.8058	59.0061	97.5454	35.4503	37.2465	21.9950	87.1932	61.6075	80.2561	75.1346
0131	87.7241	63.5907	97.1034	30.8977	64.5517	10.2513	93.5172	58.9048	79.8621	63.4650
0141	80.8786	59.4675	90.6977	44.4157	19.8966	97.0044	29.1990	97.1154	35.6589	75.6287
0151	84.7458	61.9905	72.8814	38.3412	0.0000	79.8578	0.0000	99.3839	0.0000	51.1848
0271	100.0000	45.3416	100.0000	49.2236	0.0000	70.3416	1.4706	98.7578	87.2549	97.5155
0281	100.0000	29.4527	100.0000	40.5970	83.1909	79.6020	0.0000	99.5025	100.0000	98.8060
0291	100.0000	27.6596	100.0000	39.1304	81.1475	72.5254	91.8033	98.0574	97.9508	99.9075
0301	99.4709	35.8446	99.4709	44.2506	75.6614	75.7335	99.4709	92.3870	100.0000	98.7312
0311	100.0000	30.5837	100.0000	41.1673	71.4286	83.6576	100.0000	96.2646	0.0000	100.0000
0321	100.0000	34.5906	100.0000	40.3864	48.4241	87.7645	85.1003	99.6320	94.8424	99.7240
0331	98.5632	44.9367	100.0000	28.9030	0.0000	85.5485	16.0920	94.7257	95.1149	99.5781
0341	99.5595	38.7906	99.3392	21.3919	84.5815	68.9675	62.7753	94.1814	79.2952	95.2082
0351	99.4674	23.1688	99.3342	16.0519	90.5459	94.0260	82.9561	93.3506	87.3502	98.3377
0361	99.7290	36.2542	99.7290	18.6912	82.1138	94.0203	87.2629	89.8082	93.9024	96.6905
0371	91.3472	31.9804	95.6188	13.4861	67.7985	92.2422	86.6375	85.3028	74.0416	98.0360
0381	78.4605	39.7071	99.3644	20.6265	82.6271	82.8723	83.1215	92.1481	93.2203	97.8438
0391	81.6327	33.7166	92.4701	21.9302	82.2660	78.7269	51.6538	84.6407	75.0176	99.6715
0401	53.5172	28.9544	94.5976	22.5201	73.6072	94.6764	76.7586	88.8548	79.1784	98.8893
0411	56.7218	42.6749	92.4520	23.6516	70.7905	76.3484	64.1804	98.1050	79.6338	99.8178
0421	87.2888	54.5154	92.1158	25.9178	83.5881	90.8590	25.2615	97.7239	75.9453	99.9633

Table A.7: aton_campus (pt. 2 of 2)
 Detection (η) and Discrimination (ξ) for each shadow removal method (default parameters)

frame	C - η	C - ξ	P - η	P - ξ	G - η	G - ξ	SRT - η	SRT - ξ	LRT - η	LRT - ξ
1061	100.0000	27.8261	100.0000	14.4099	78.4615	88.3230	89.2308	87.0807	0.0000	100.0000
1071	92.6282	26.1473	100.0000	15.9018	55.4487	100.0000	99.6795	85.0587	100.0000	70.1174
1081	100.0000	32.9322	100.0000	28.5558	91.8919	7.4398	56.7568	97.1554	0.0000	100.0000
1091	100.0000	28.5118	98.2456	24.4784	73.6842	4.8679	98.2456	80.8067	0.0000	71.4882
1101	100.0000	5.8824	100.0000	10.1961	0.0000	20.9804	30.2158	85.8824	90.6475	99.0196
1111	99.3671	13.8012	96.2025	12.0468	99.3671	57.4269	17.0886	63.8596	86.0759	97.1930
1121	100.0000	6.7938	98.7500	17.6400	0.0000	100.0000	36.2500	97.4970	84.3750	98.9273
1131	99.4792	10.6405	97.9167	18.5950	81.7708	97.6240	9.3750	98.8636	67.1875	99.8967
1141	100.0000	7.8014	98.3871	15.9574	82.9032	91.8440	0.0000	100.0000	56.7742	99.1726
1151	99.4723	8.1040	99.4723	6.2691	81.2665	90.6728	0.0000	100.0000	94.1953	94.0367

Table A.8: aton_hallway
 Detection (η) and Discrimination (ξ) for each shadow removal method (default parameters)

frame	C - η	C - ξ	P - η	P - ξ	G - η	G - ξ	SRT - η	SRT - ξ	LRT - η	LRT - ξ
0025	79.9183	76.9398	24.1681	97.3956	26.3865	95.1167	91.4769	68.6923	83.8879	96.1476
0151	93.7595	85.9546	34.5688	99.2863	71.2935	24.6750	99.8109	83.3546	93.2300	99.6941
0164	94.2697	73.4476	22.3930	99.2838	35.7453	73.2952	96.4688	46.9257	96.2954	86.1943
0175	80.1485	78.5135	13.8420	98.2770	58.1364	23.8514	75.0169	81.1486	68.3322	99.9324
0194	95.9436	81.7539	43.2883	99.1648	61.2777	94.4427	99.0398	64.6161	98.2951	98.3296
0251	79.7990	80.1032	23.5176	99.7052	7.6382	100.0000	77.3869	96.8312	74.9749	99.1157
0275	84.1121	88.8078	9.6573	99.5134	42.9907	66.6667	48.2866	97.0803	91.5888	100.0000
0431	98.2749	77.1237	41.7251	99.1803	61.3477	47.9136	99.2453	75.2981	99.4070	99.0313
0451	97.2427	91.3690	45.6396	99.8103	36.1494	84.9036	99.2946	58.7733	97.9320	99.3361
0600	36.5385	91.6890	5.7692	99.1957	68.2692	24.1287	53.8462	94.9062	0.0000	100.0000
0621	98.9309	75.8829	38.2812	98.3204	23.4786	92.4849	96.9984	72.3084	97.8207	93.1740
1101	94.8959	88.4066	41.3183	99.8392	76.1077	97.4812	98.4187	80.0286	97.6358	99.9107
1151	93.6965	57.5575	14.0078	99.8905	66.7315	93.4830	98.2879	46.4403	97.3930	86.2541

Table A.9: aton_lab
 Detection (η) and Discrimination (ξ) for each shadow removal method (default parameters)

frame	C - η	C - ξ	P - η	P - ξ	G - η	G - ξ	SRT - η	SRT - ξ	LRT - η	LRT - ξ
0091	98.7633	61.2542	72.8661	95.3073	38.3608	28.8621	93.6227	71.0963	87.0757	94.4767
0101	98.9364	70.9606	87.2596	97.8268	46.0964	70.0472	93.8221	71.4331	86.8296	86.8031
0151	97.8528	69.6585	76.8071	97.1290	57.9905	50.9519	73.2995	99.2143	88.3134	98.9121
0161	97.1438	74.2217	72.0062	95.5168	41.3455	71.2951	87.0096	94.1469	84.6869	93.8045
0221	90.6459	82.9753	67.9287	99.0591	69.2650	87.4490	73.0512	92.0646	83.7416	99.8225
0231	96.6308	77.9151	78.1967	98.0355	86.6838	14.1952	91.9461	83.9037	88.2561	95.0887
0281	96.9956	71.1680	67.4601	96.2657	61.6825	42.0756	87.1967	93.9210	88.1442	95.2236
0291	99.5092	77.4809	66.5879	95.1018	45.3372	80.3753	82.1123	95.8015	87.7477	99.6819
0301	92.9468	82.6877	74.3425	98.1824	20.1584	55.2145	80.7980	97.8546	82.6210	99.0465
0471	85.9320	81.8064	44.1970	98.5657	78.0774	69.5309	52.5205	96.6145	45.7210	87.1560
0481	95.7592	79.9637	62.9772	98.6250	47.4565	88.7730	93.2590	89.1659	90.7299	97.5370
0561	97.8538	75.1721	69.2714	97.7179	27.3388	90.1239	92.9012	79.9921	87.7174	93.7439
0681	96.6113	70.9189	48.4831	96.7568	52.3526	76.2625	91.3795	74.8726	85.8615	93.5598
0881	90.5501	68.8213	57.5865	95.9261	60.6921	73.9815	4.7028	99.8914	60.0710	99.2395

APPENDIX B
PARAMETER EVALUATION

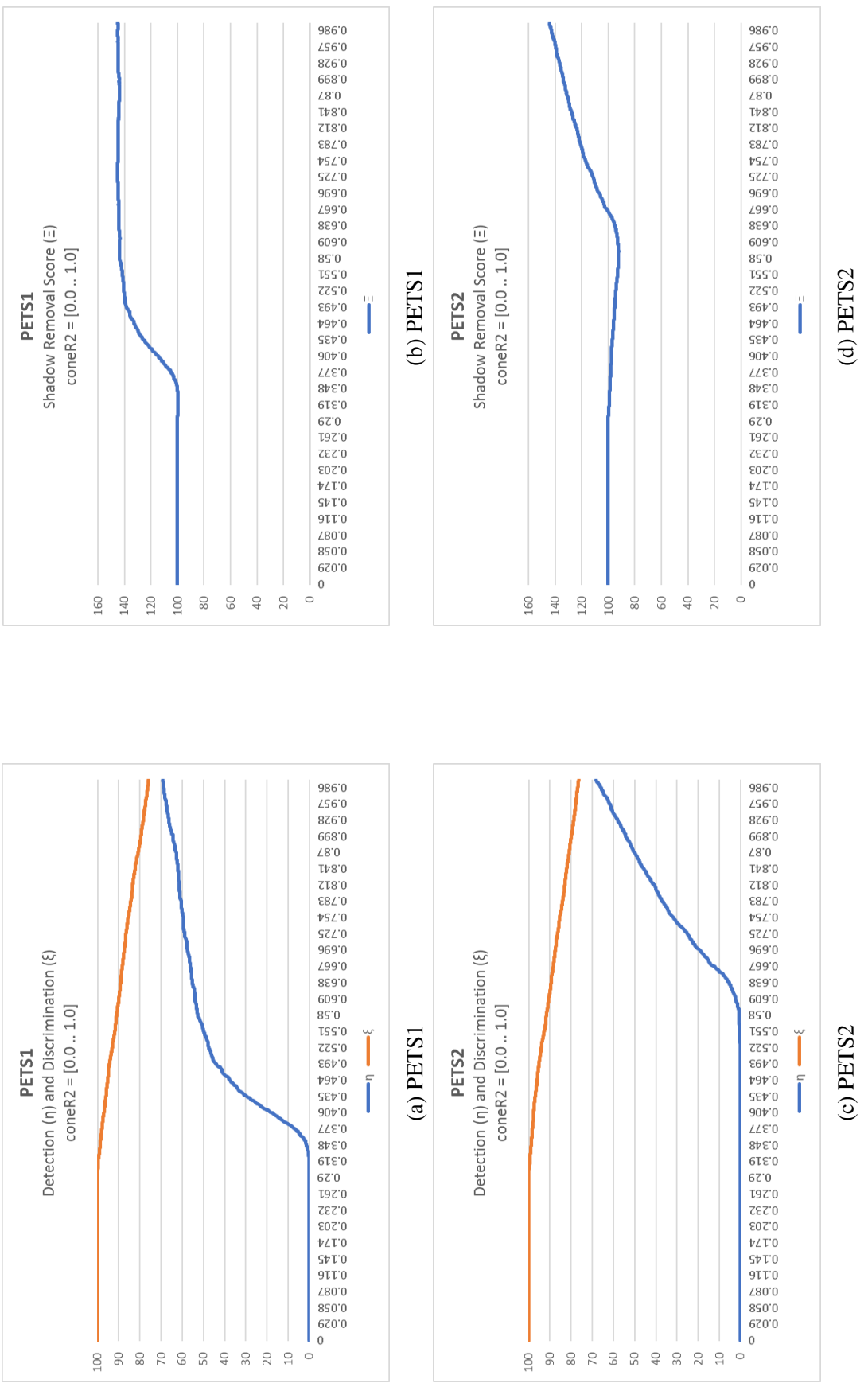


Figure B.1: Detection (blue) and discrimination (orange) rates are calculated as the value of $coneR2$ is varied from [0.0 .. 1.0]. (pt. 1 of 4)

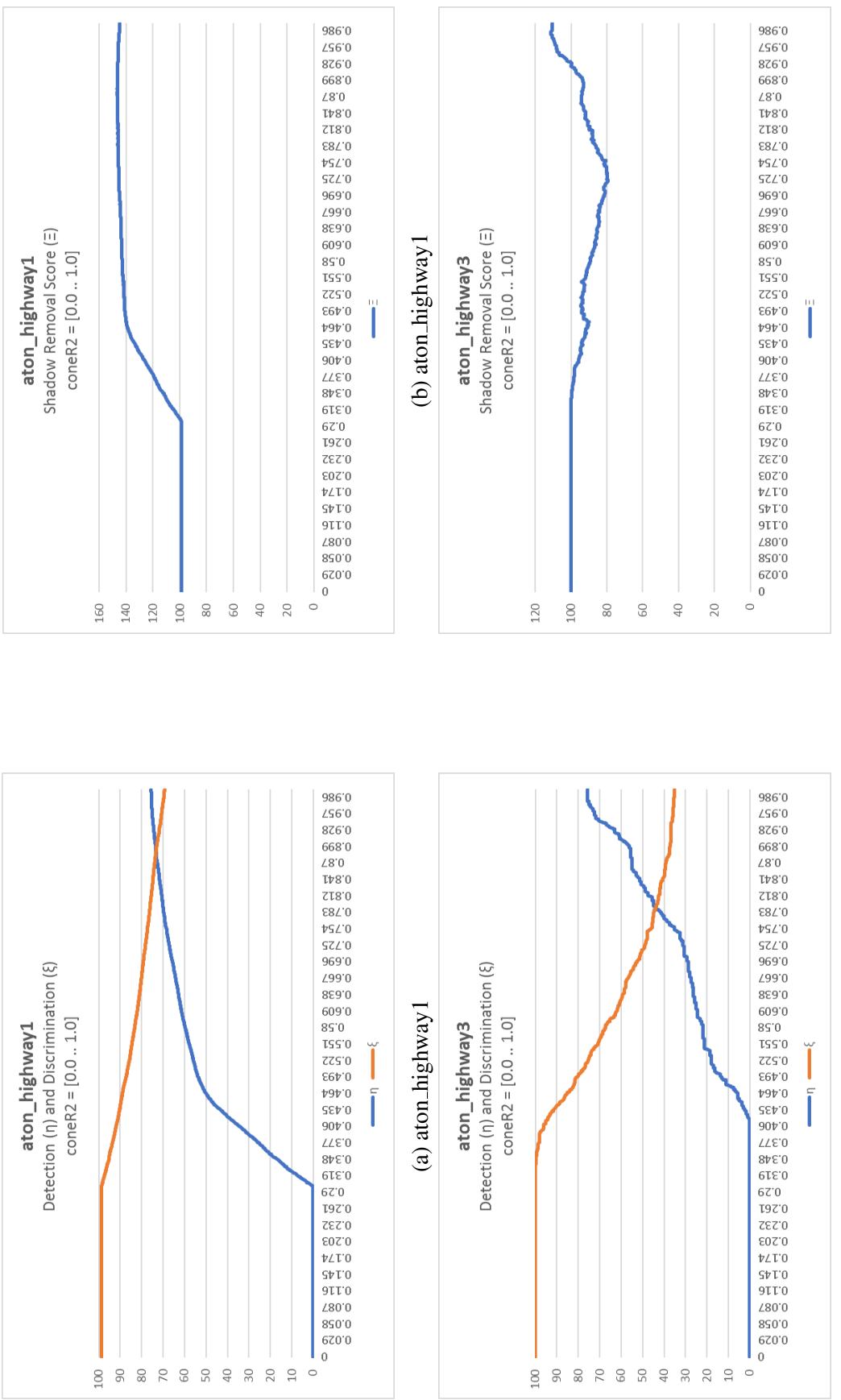


Figure B2: Detection (blue) and discrimination (orange) rates are calculated as the value of $coneR2$ is varied from [0.0 .. 1.0]. (pt. 2 of 4)

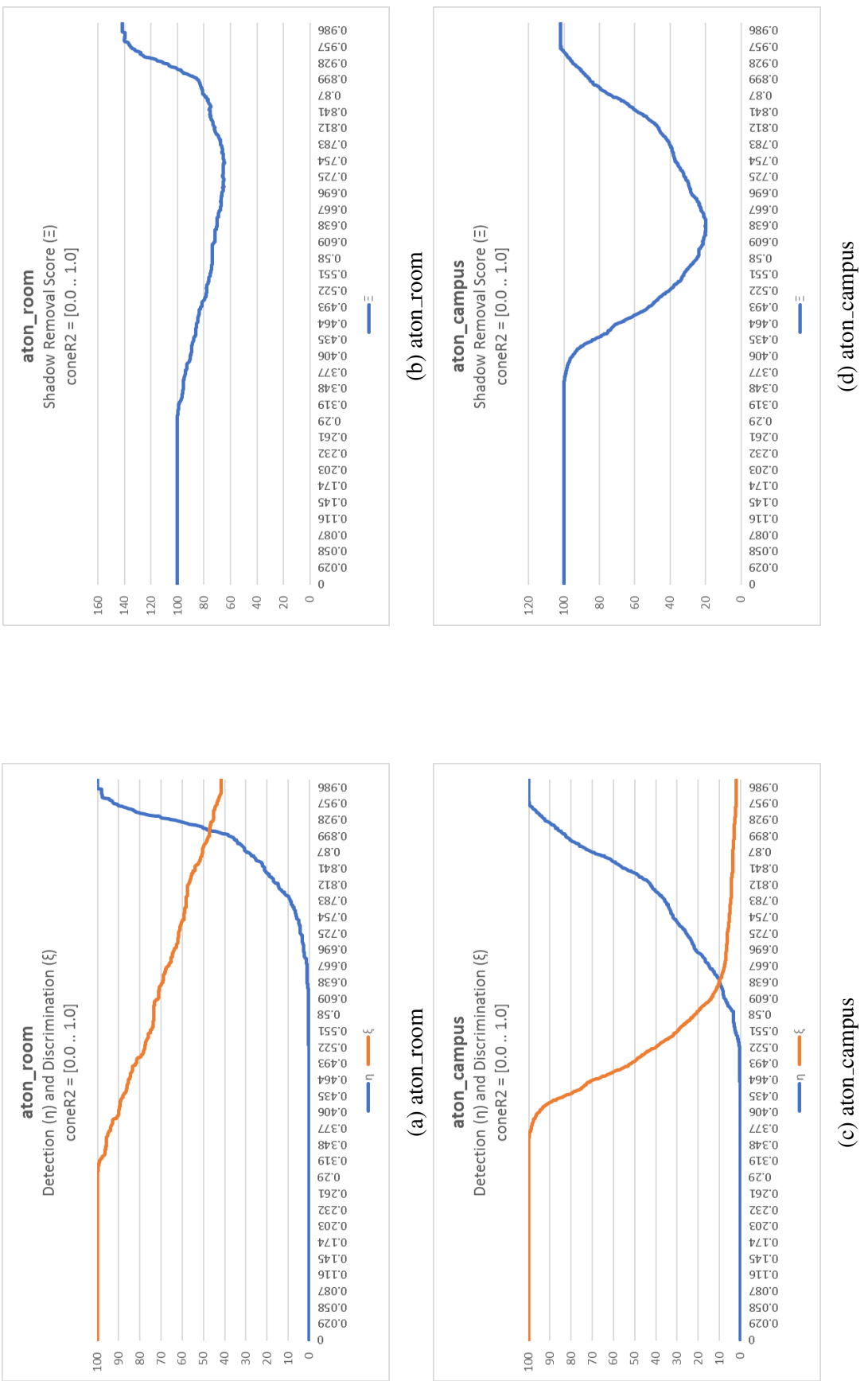


Figure B.3: Detection (blue) and discrimination (orange) rates are calculated as the value of $coneR2$ is varied from [0.0 .. 1.0]. (pt. 3 of 4)

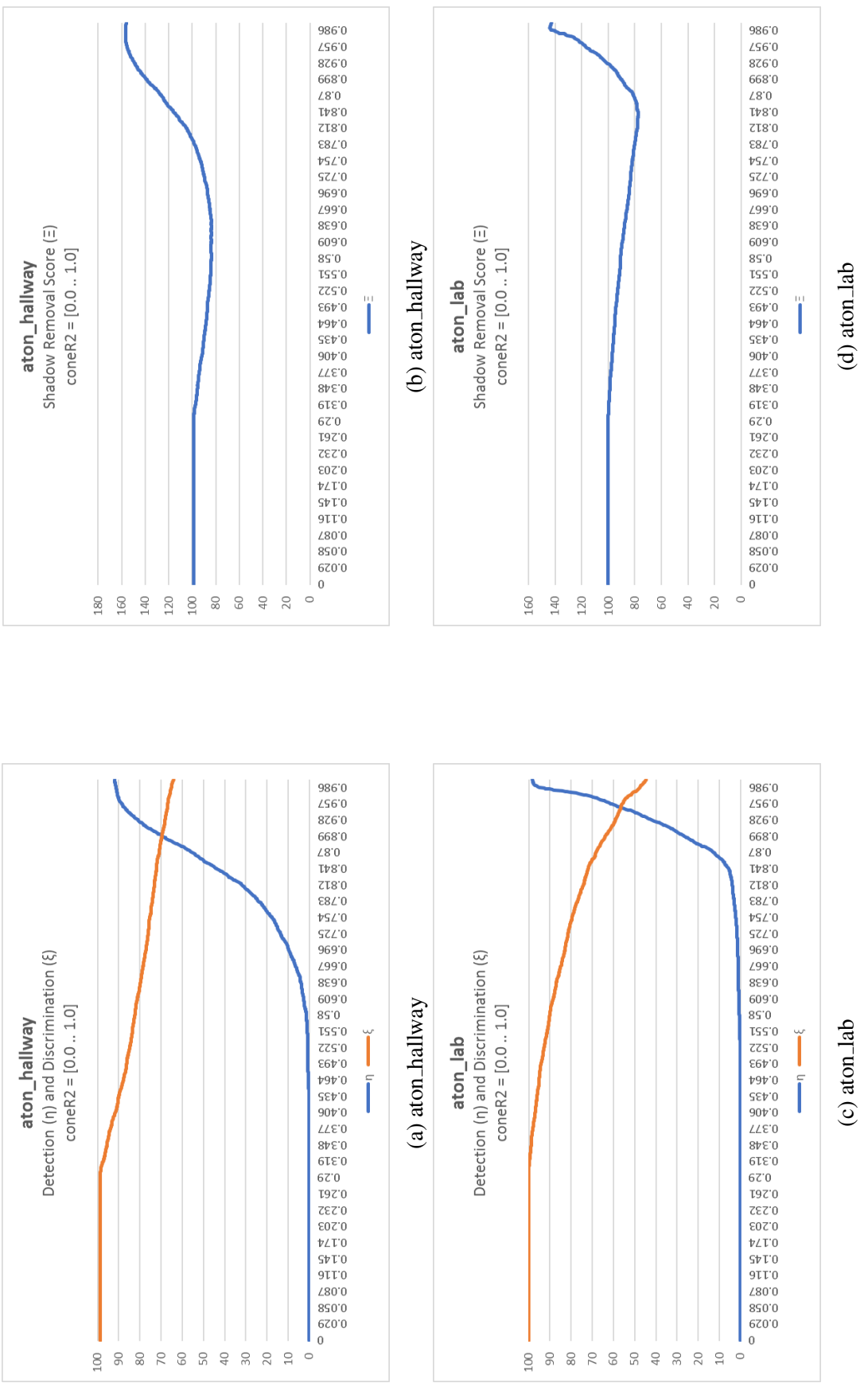


Figure B.4: Detection (blue) and discrimination (orange) rates are calculated as the value of $conerR2$ is varied from [0.0 .. 1.0]. (pt. 4 of 4)

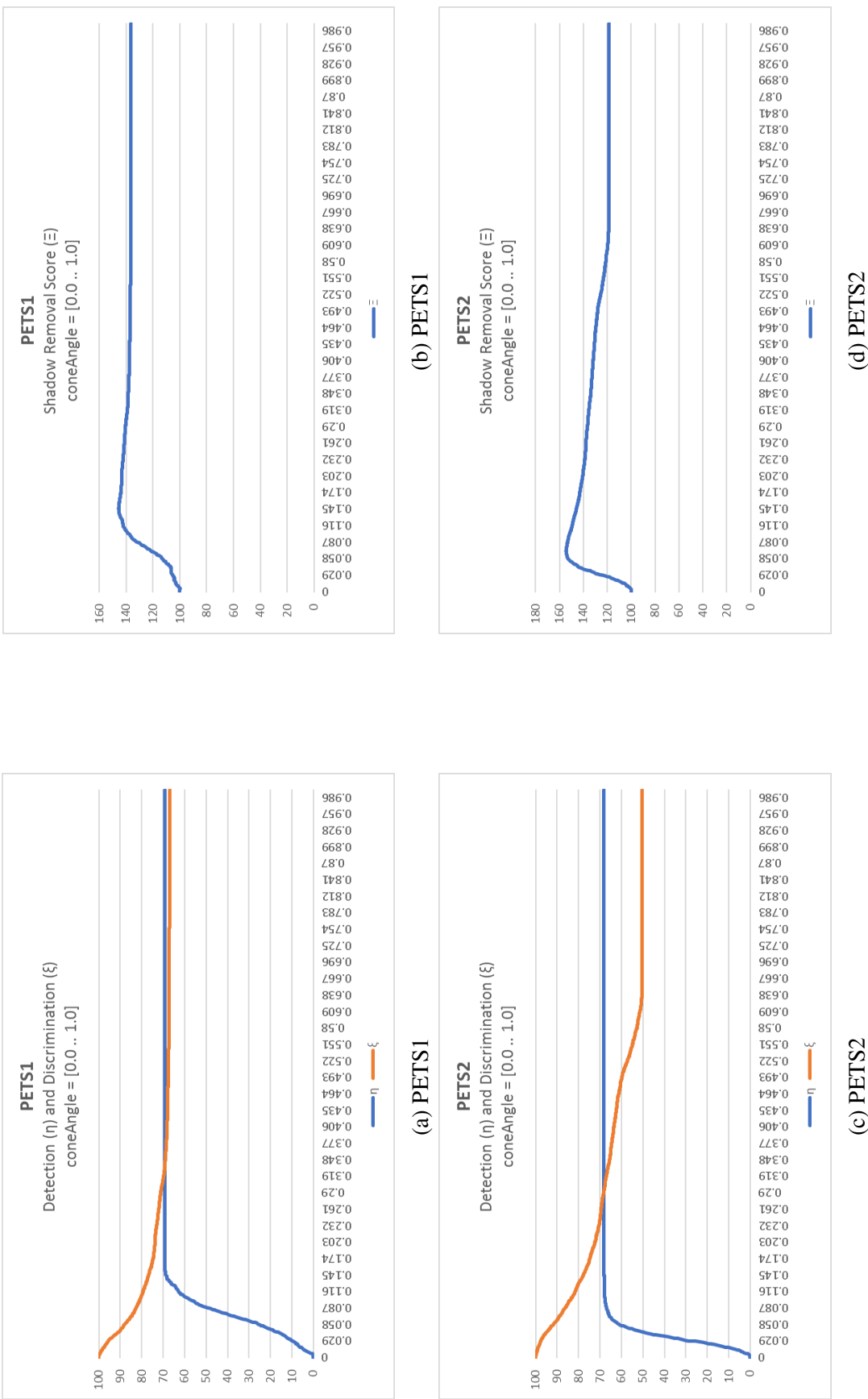


Figure B.5: Detection (blue) and discrimination (orange) rates are calculated as the value of $coneAngle$ is varied from [0.0 .. 1.0]. (pt. 1 of 4)

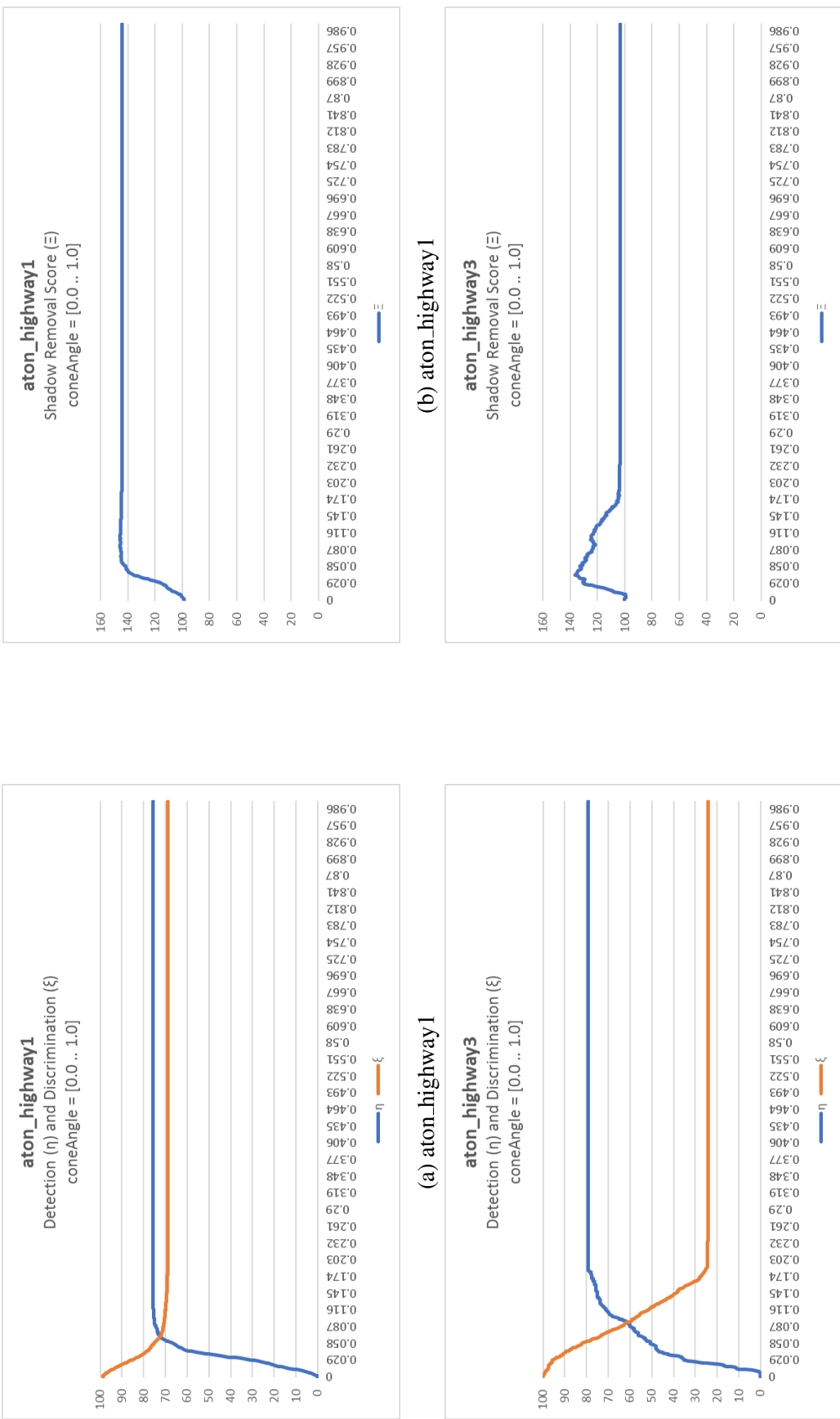


Figure B.6: Detection (blue) and discrimination (orange) rates are calculated as the value of $coneAngle$ is varied from [0.0 .. 1.0]. (pt. 2 of 4)

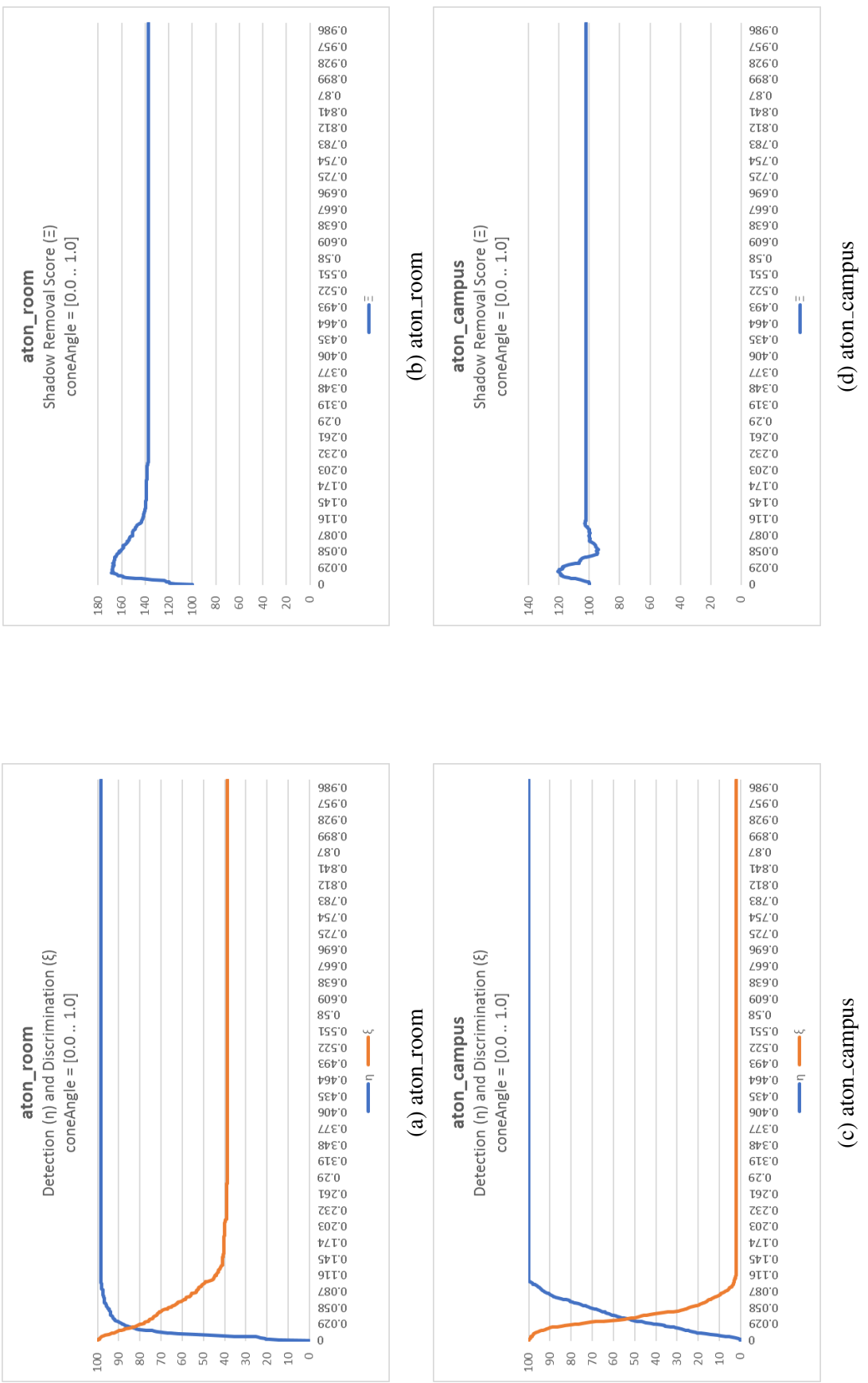


Figure B.7: Detection (blue) and discrimination (orange) rates are calculated as the value of $coneAngle$ is varied from [0.0 .. 1.0]. (pt. 3 of 4)

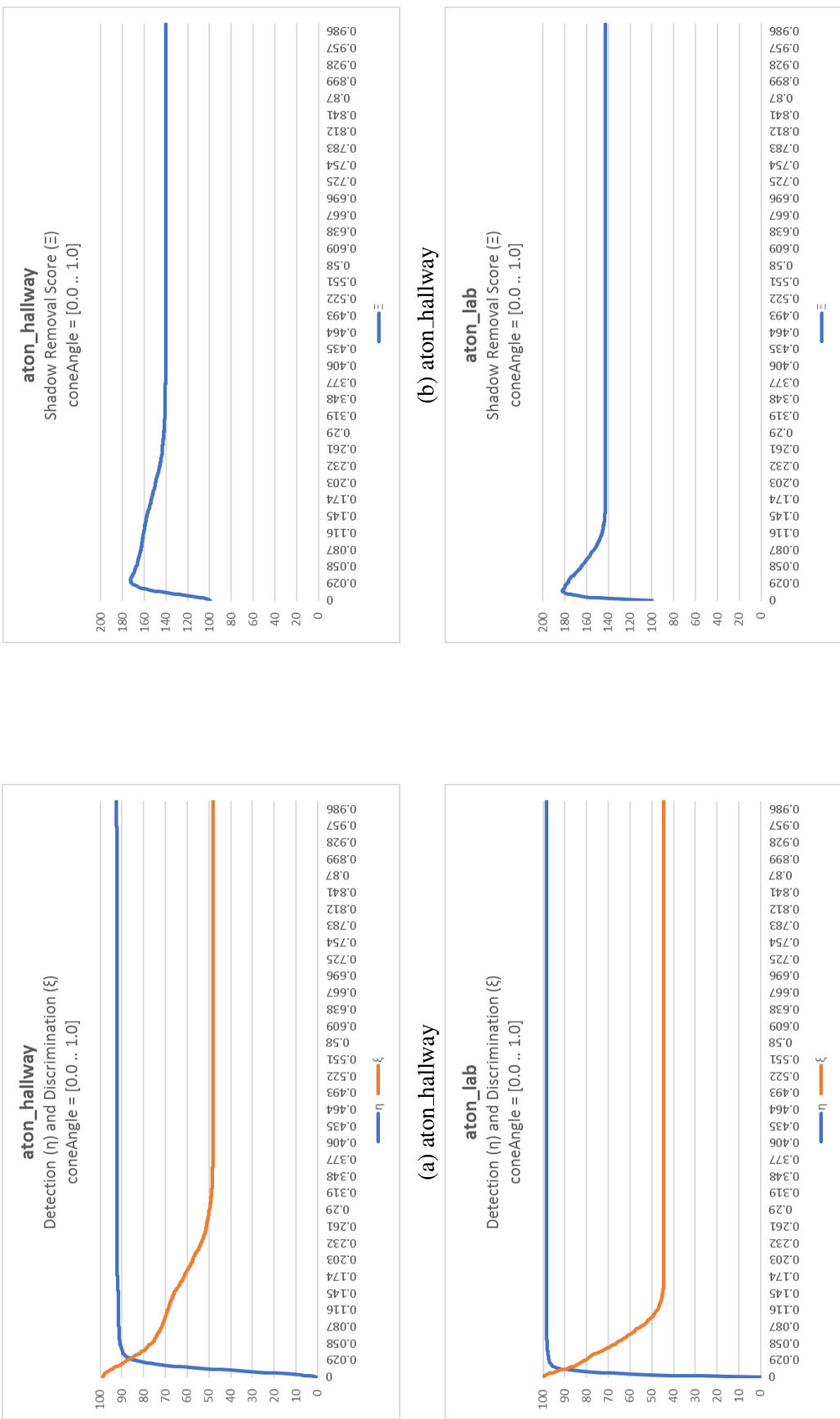


Figure B.8: Detection (blue) and discrimination (orange) rates are calculated as the value of $coneAngle$ is varied from [0.0 .. 1.0]. (pt. 4 of 4)

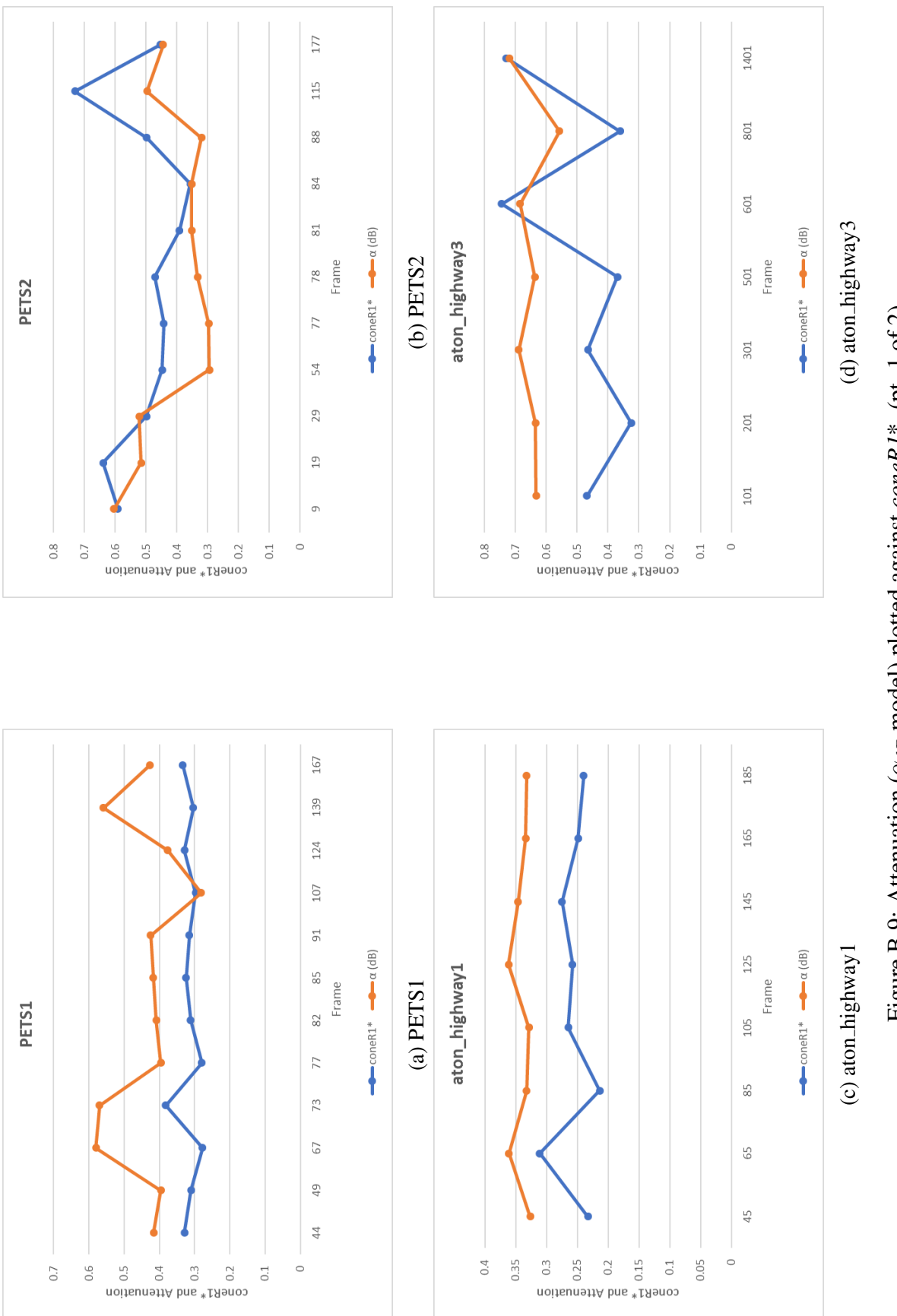


Figure B.9: Attenuation (α_{dB} model) plotted against $coneR1^*$. (pt. 1 of 2)

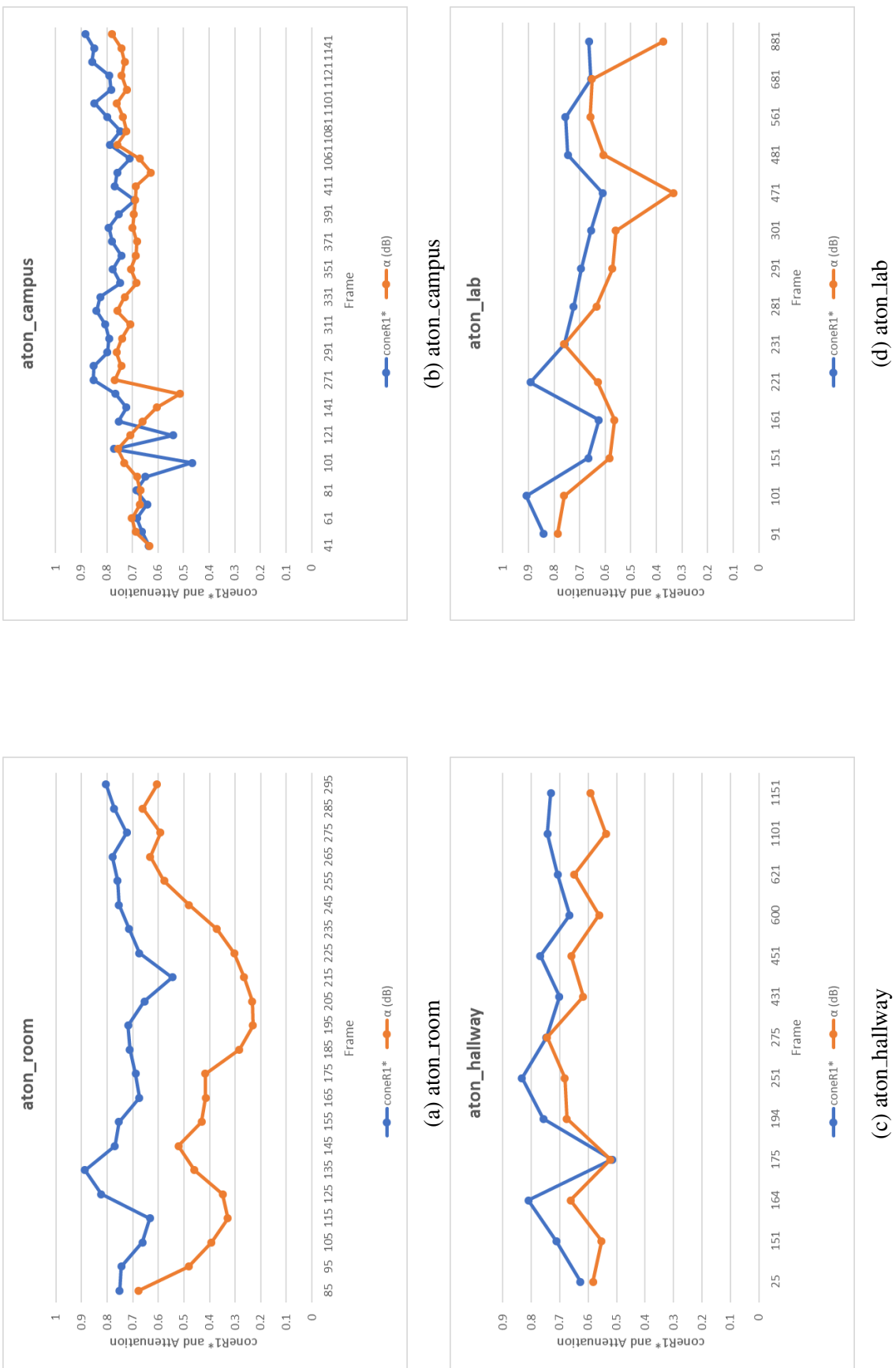


Figure B.10: Attenuation (α_{dB} model) plotted against coneRI^* . (pt. 2 of 2)

APPENDIX C

RESULTS

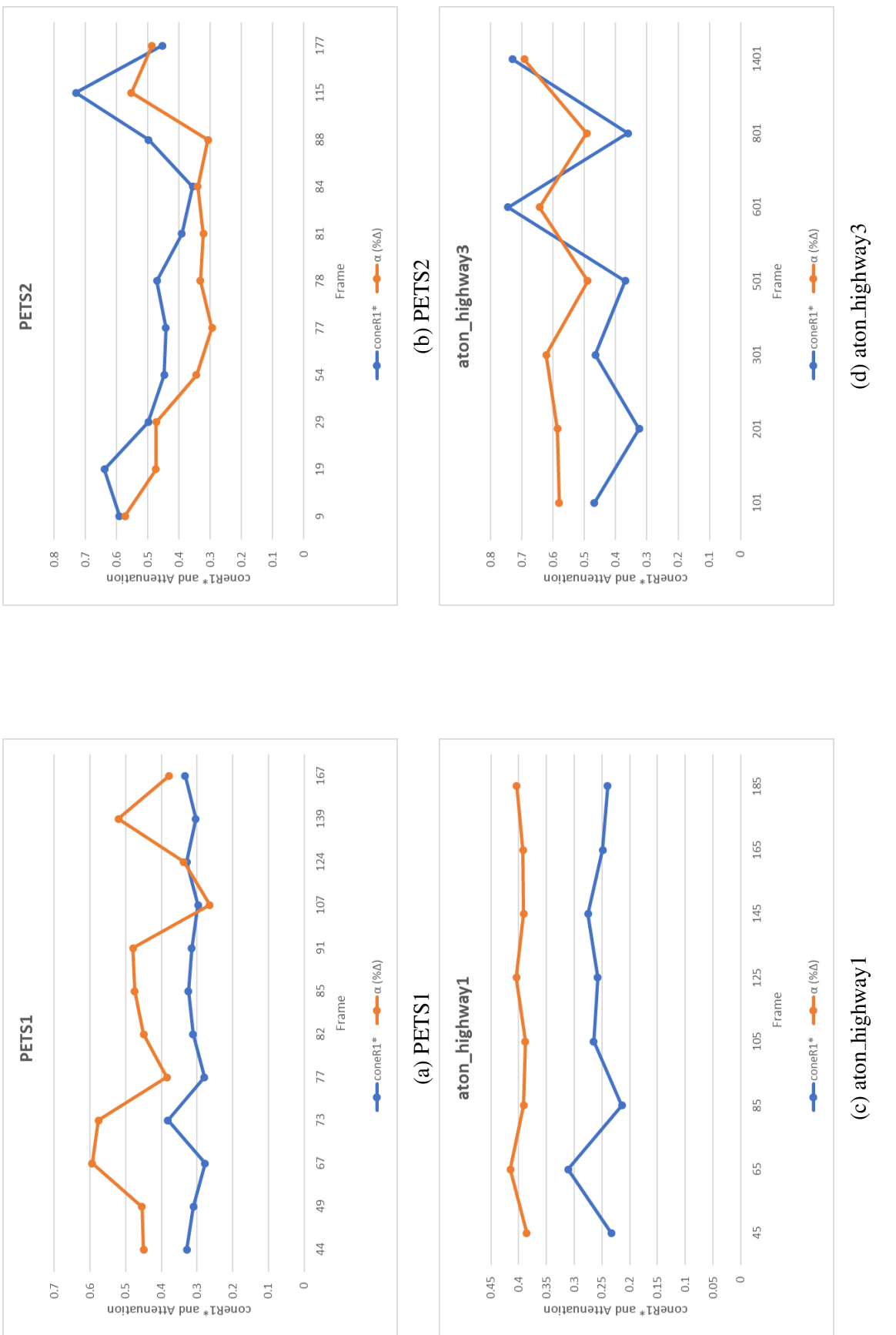


Figure C.1: Attenuation ($\alpha \% \Delta$ model) plotted against coneRI^* . (pt. 1 of 2)

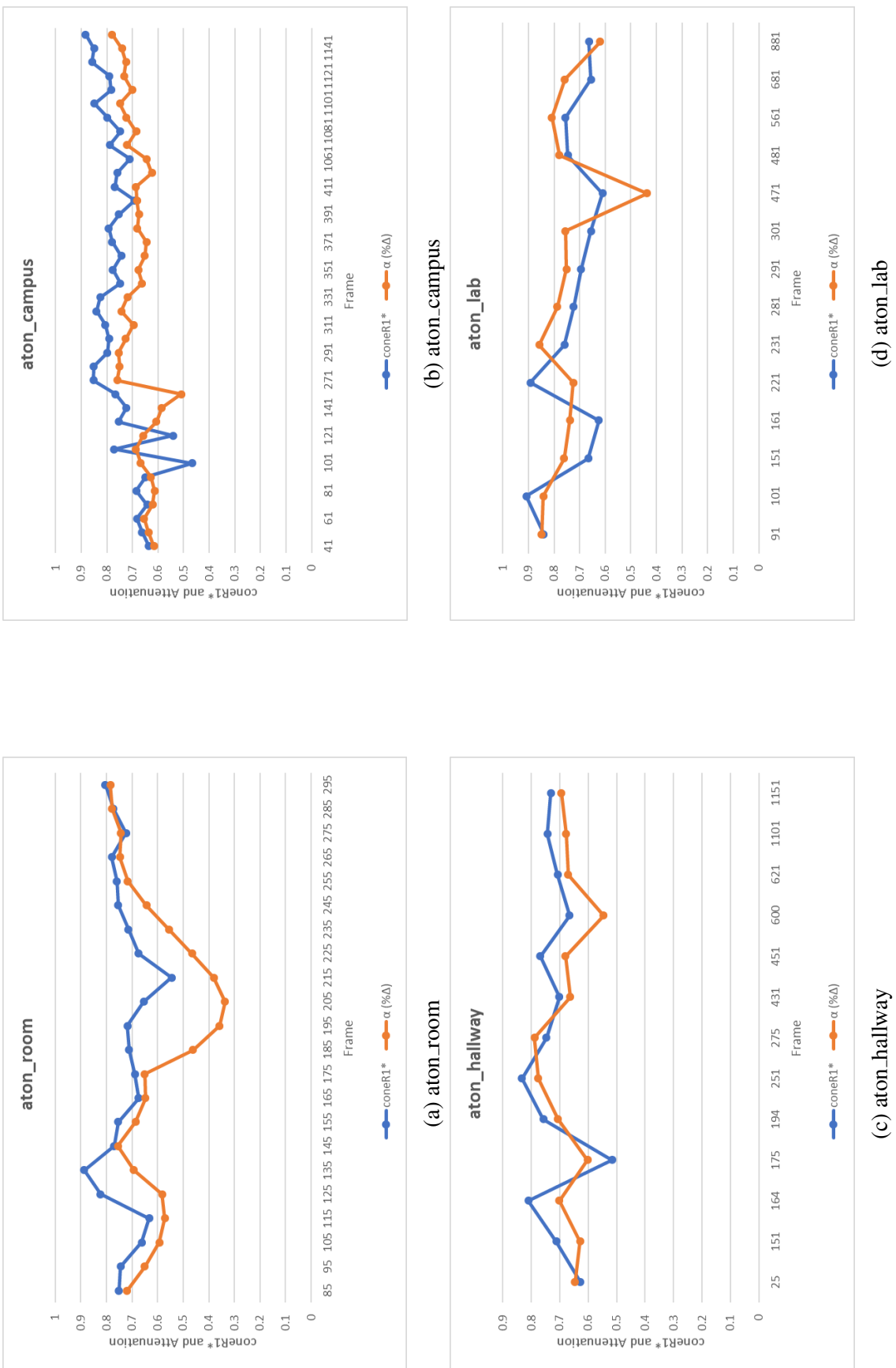
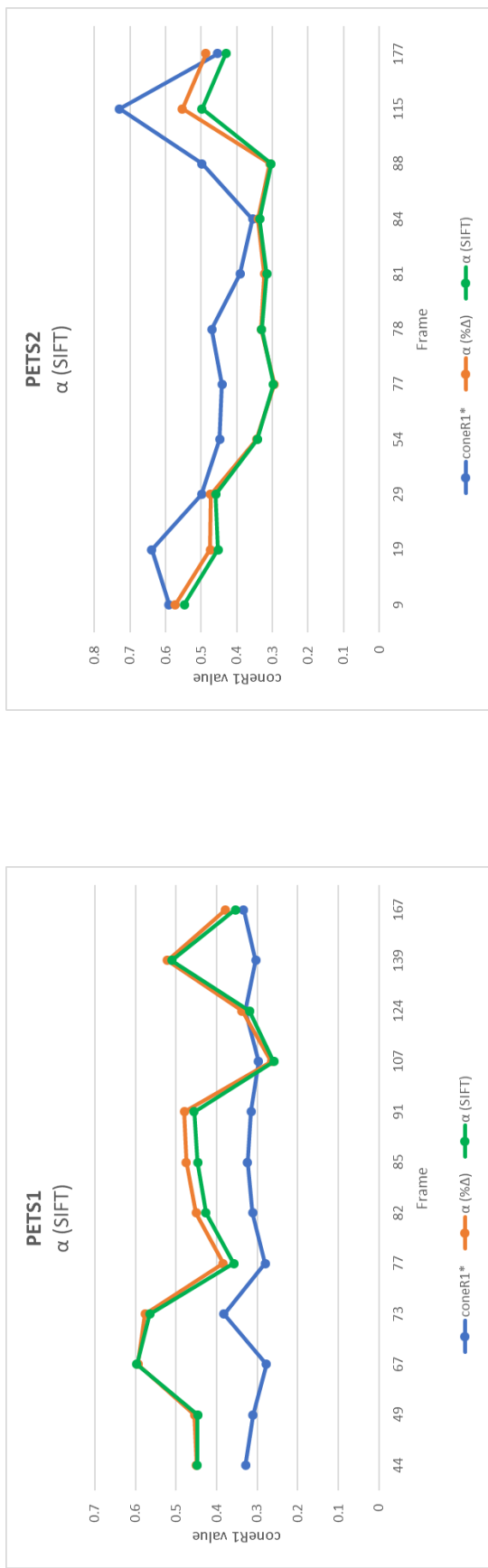
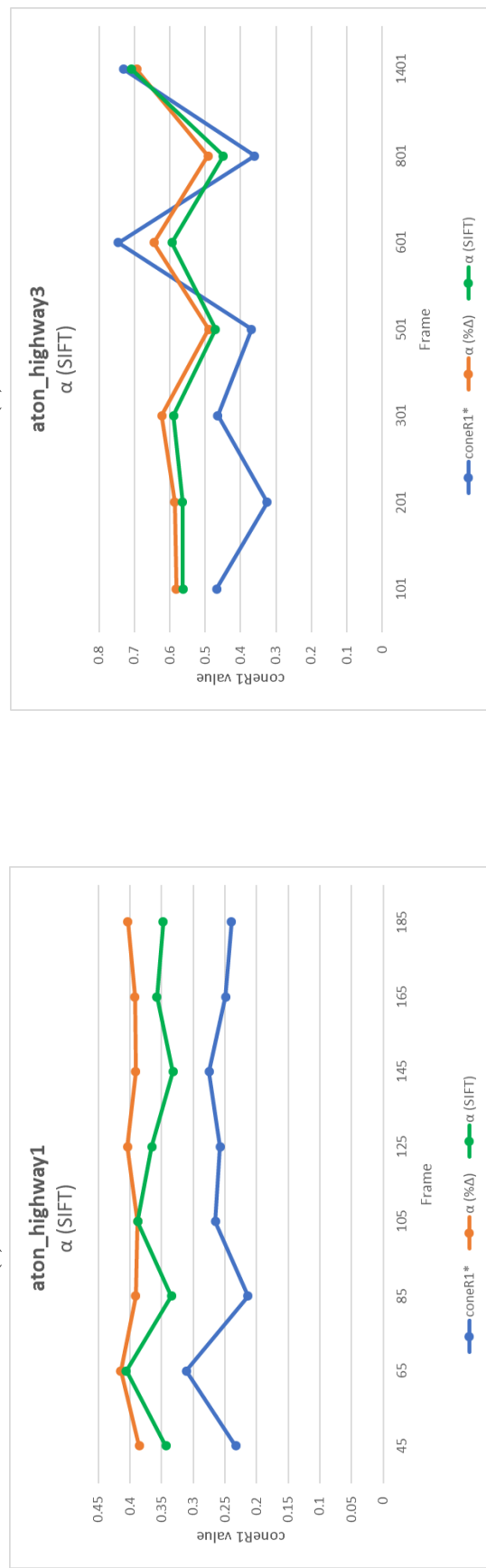


Figure C.2: Attenuation ($\alpha \% \Delta$ model) plotted against coneRI^* . (pt. 2 of 2)



(a) PETS1



(b) PETS2

(c) aton_highway1

(d) aton_highway3

Figure C.3: α_{SIFT} (green) is plotted against $coneR1^*$ and $\alpha\% \Delta$. (pt. 1 of 2)

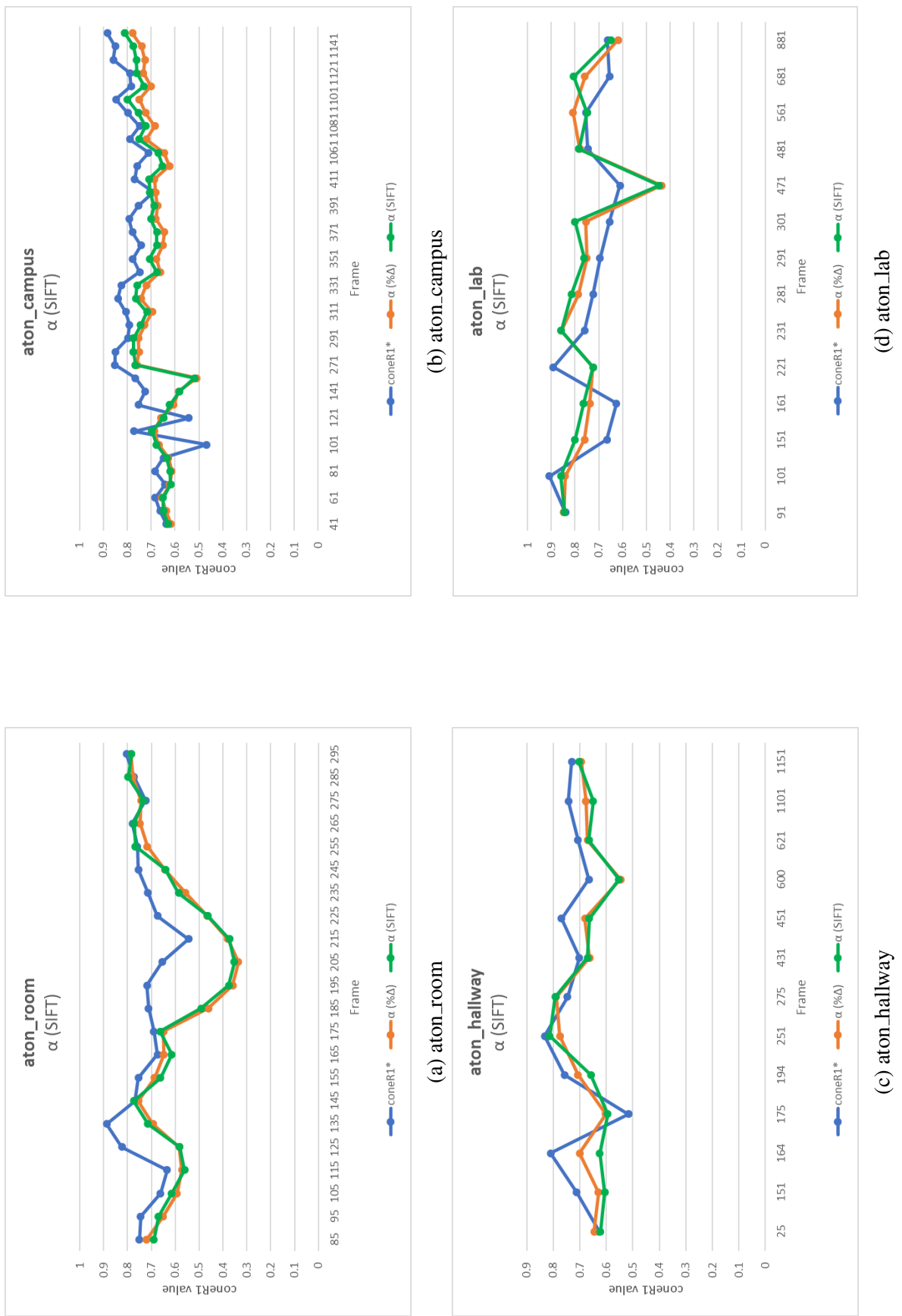


Figure C.4: coneRI' (green) is plotted against coneRI^* and $\alpha\% \Delta$. (pt. 2 of 2)

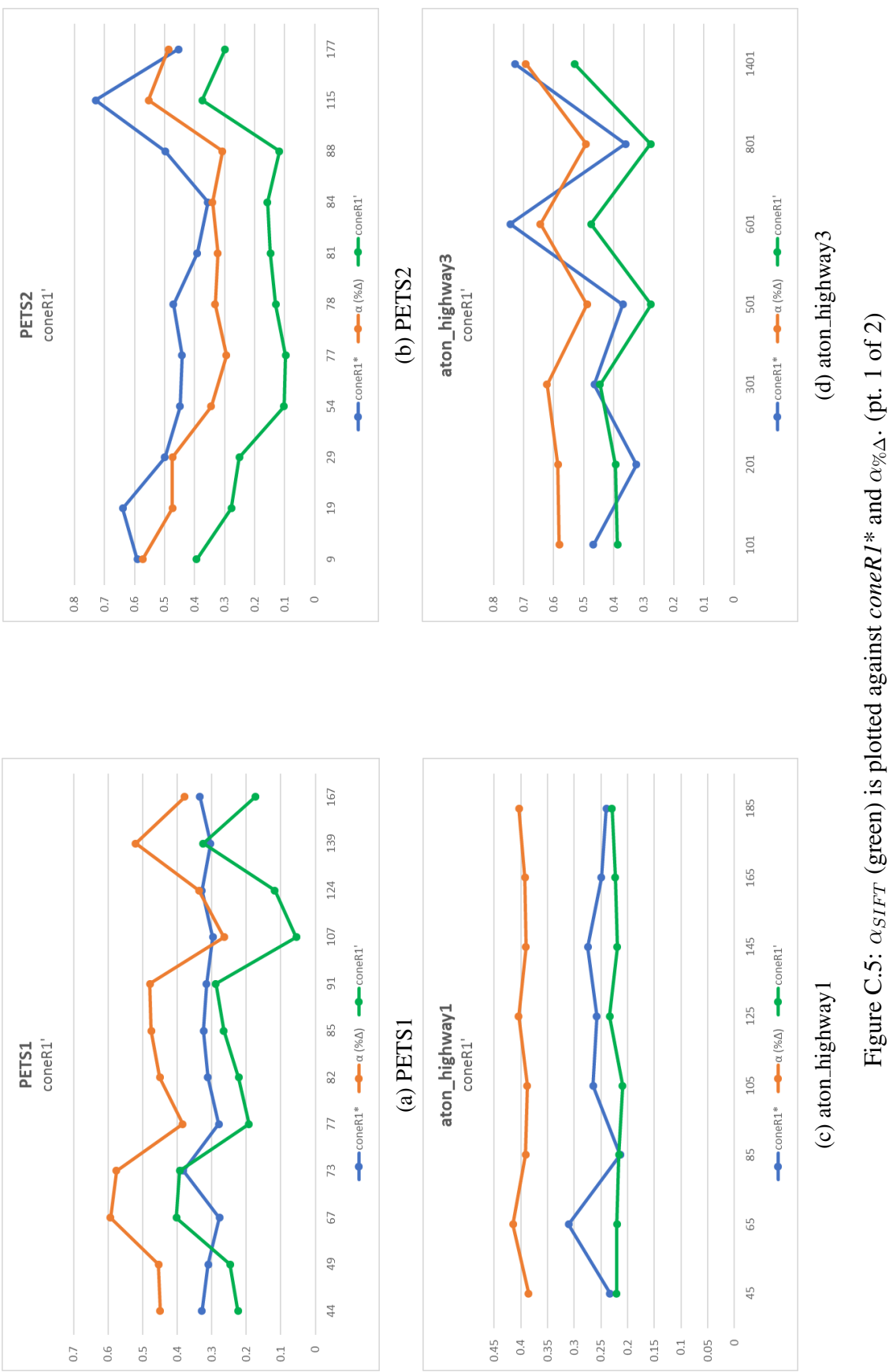


Figure C.5: α_{SIFT} (green) is plotted against coneR1^* and $\alpha_{\% \Delta}$. (pt. 1 of 2)

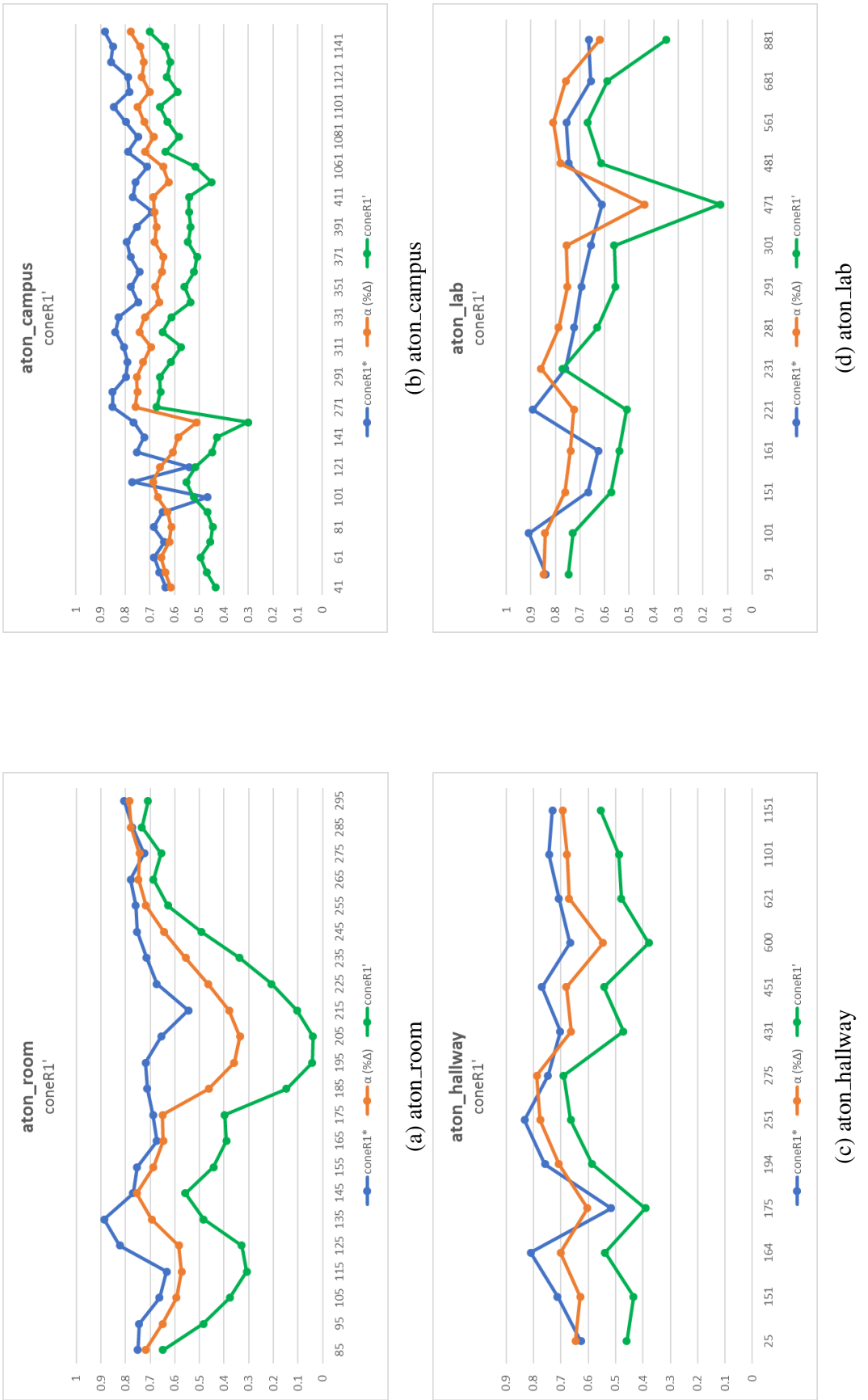


Figure C.6: $coneRI'$ (green) is plotted against $coneRI^*$ and $\alpha_{\% \Delta}$. (pt. 2 of 2)

Table C.1: PETS1

Detection and Discrimination rates calculated for both default coneR1 (Original) and coneR1' (Adaptive).

frame	coneR1*	coneR1'	Original η	Adaptive η	Original ξ	Adaptive ξ
44	0.329	0.223804	69.2827	69.9578	75.9517	73.8973
49	0.31	0.246728	53.108	53.6512	83.4889	81.4617
67	0.278	0.402792	65.6433	58.9181	67.6909	71.1704
73	0.382	0.393097	66.2295	63.9344	64.7059	68.0561
77	0.28	0.192245	79.6947	82.1374	76.039	72.5529
82	0.311	0.222533	78.6989	80.3717	73.8816	69.7234
85	0.324	0.265211	68.8791	69.5225	66.9706	64.903
91	0.315	0.288086	71.5467	72.0817	68.4584	68.0297
107	0.297	0.0550418	63.1347	64.4592	80.6748	71.3574
124	0.329	0.117233	79.3729	86.3036	66.0321	47.3447
139	0.304	0.324891	89.7321	88.8393	57.1618	57.4271
167	0.334	0.173734	88.5057	89.1626	80.3523	77.3713

Table C.2: PETS2

Detection and Discrimination rates calculated for both default coneR1 (Original) and coneR1' (Adaptive).

frame	coneR1*	coneR1'	Original η	Adaptive η	Original ξ	Adaptive ξ
9	0.591	0.392866	68.0879	68.0879	76.4585	78.5824
19	0.639	0.277102	33.5938	33.5938	84.7328	84.2682
29	0.499	0.251038	33.9921	33.9921	84.0453	83.1735
54	0.448	0.102197	99.115	99.115	66.7976	31.0413
77	0.442	0.0969234	99.2218	99.2218	70.5216	57.3393
78	0.471	0.129563	100	100	66.2837	49.4034
81	0.391	0.147082	96.9161	97.1689	76.2933	70.1039
84	0.356	0.157141	92.2688	92.6301	74.164	69.3635
88	0.498	0.11751	100	100	62.7468	43.525
115	0.73	0.374374	20.2454	20.2454	65.5239	67.8525
177	0.454	0.298634	73.6506	73.6506	69.8562	69.7363

Table C.3: aton_highway1

Detection and Discrimination rates calculated for both default coneR1 (Original) and coneR1' (Adaptive).

frame	coneR1*	coneR1'	Original η	Adaptive η	Original ξ	Adaptive ξ
45	0.233	0.220497	75.55	87.2782	69.2299	61.9624
65	0.311	0.220315	67.158	72.2248	65.4284	52.7443
85	0.214	0.216213	73.1796	84.2697	58.4456	51.8659
105	0.265	0.209683	82.7473	88.022	69.9272	62.7913
125	0.258	0.233547	69.1618	81.1887	63.6085	54.9916
145	0.275	0.219385	72.2989	80.6568	64.8861	56.0676
165	0.249	0.223016	67.2983	77.5194	63.1035	55.607
185	0.24	0.229775	65.7503	76.8051	67.1285	60.3536

Table C.4: aton_highway3

Detection and Discrimination rates calculated for both default coneR1 (Original) and coneR1' (Adaptive).

frame	coneR1*	coneR1'	Original η	Adaptive η	Original ξ	Adaptive ξ
101	0.468	0.387717	75.625	75.625	35.123	37.1365
201	0.325	0.394711	71.6456	67.3418	37.7417	39.9072
301	0.465	0.44571	72.1311	70.9016	45.23	50.0852
501	0.37	0.276136	73.5925	73.5925	67.1176	67.1176
601	0.745	0.476506	85.1695	82.6271	36.7862	45.6839
801	0.361	0.277987	74.0392	74.0392	34.5425	34.1364
1401	0.73	0.530566	80	80	41.2587	50.3497

Table C.5: aton_room

Detection and Discrimination rates calculated for both default coneR1 (Original) and coneR1' (Adaptive).

frame	coneR1*	coneR1'	Original η	Adaptive η	Original ξ	Adaptive ξ
85	0.751	0.649083	98.3146	97.191	40.4321	71.6049
95	0.745	0.484626	96.2506	95.8559	65.4899	80.2594
105	0.662	0.377712	91.674	91.054	74.0519	82.3353
115	0.634	0.30766	93.0137	93.0137	82.6196	82.8715
125	0.824	0.328275	89.6272	89.6272	78.0451	80.3008
135	0.887	0.483102	96.3006	95.6069	64.1892	78.5473
145	0.77	0.558232	96.7391	96.0474	65.8031	78.7565
155	0.754	0.443622	94.9045	94.6921	73.3198	80.8554
165	0.674	0.391485	93.8378	93.2973	69.0015	74.0686
175	0.689	0.397271	93.6877	93.3555	70.3377	75.7709
185	0.712	0.147542	82.381	83.3333	73.8574	57.7697
195	0.719	0.0423129	61.1111	64.8148	70.6796	34.3689
205	0.655	0.0391442	54.8387	54.8387	70.8333	42.6136
215	0.545	0.105035	48.913	50	70.3166	49.2084
225	0.674	0.20744	86.25	86.5625	63.7487	54.6859
235	0.715	0.337354	95.037	94.9314	73.5849	75.5503
245	0.754	0.492393	97.561	97.1458	65.1096	77.624
255	0.759	0.627669	99.0716	98.6822	65.9314	85.6863
265	0.779	0.687616	99.2512	97.6628	62.6719	85.8939
275	0.724	0.655212	98.8365	97.5761	66.711	89.0957
285	0.773	0.733917	99.4827	98.3026	68.1431	90.2896
295	0.805	0.709282	99.0119	96.6984	62.855	85.6879

Table C.6: aton_campus

Detection and Discrimination rates calculated for both default coneR1 (Original) and coneR1' (Adaptive).

frame	coneR1*	coneR1'	Original η	Adaptive η	Original ξ	Adaptive ξ
41	0.636	0.434367	100	100	2.139	17.9144
51	0.662	0.469132	99.9291	99.5272	11.5192	33.9065
61	0.683	0.495272	99.9034	95.9259	31.9713	59.868
71	0.642	0.454936	99.0625	93.3413	32.0908	54.5861
81	0.685	0.444833	96.8359	91.9249	29.5123	46.1152
91	0.649	0.466827	98.3946	94.7157	36.9529	51.9231
101	0.467	0.522102	100	93.3692	44.0171	55.6058
111	0.772	0.552027	97.0534	97.0534	58.1594	67.0103
121	0.542	0.514771	97.4386	91.1419	38.9846	55.8306
131	0.754	0.448236	96.8276	92.6897	32.298	46.3734
141	0.724	0.426879	90.6977	90.6977	52.2929	70.858
151	0.766	0.301711	72.8814	72.8814	38.3412	38.5308
271	0.852	0.671848	100	100	49.2236	78.5714
281	0.851	0.656997	100	100	40.597	73.8308
291	0.798	0.659748	100	100	39.1304	70.5828
301	0.791	0.616497	99.4709	99.4709	44.2506	72.7201
311	0.806	0.572523	100	100	41.1673	64.0467
321	0.84	0.649439	100	100	40.3864	73.5051
331	0.826	0.612811	100	100	28.903	64.346
341	0.748	0.53507	99.3392	99.3392	21.3919	53.3942
351	0.777	0.559359	99.3342	98.8016	16.0519	57.8182
361	0.743	0.521477	99.729	99.729	18.6912	47.6871
371	0.779	0.508699	95.6188	95.6188	13.4861	44.0589
381	0.793	0.545052	99.3644	99.3644	20.6265	69.3247
391	0.753	0.534082	92.4701	92.3997	21.9302	64.9692
401	0.692	0.541953	94.5976	94.4851	22.5201	73.4201
411	0.769	0.541069	92.452	92.452	23.6516	75
421	0.759	0.450694	92.1158	92.1158	25.9178	61.674
1061	0.711	0.515943	100	100	14.4099	40.6211
1071	0.789	0.636891	100	100	15.9018	50.4803
1081	0.748	0.583271	100	100	28.5558	49.2341
1091	0.798	0.628366	98.2456	98.2456	24.4784	48.1224
1101	0.848	0.65963	100	100	10.1961	46.6667
1111	0.784	0.586309	96.2025	95.5696	12.0468	52.6316
1121	0.79	0.631131	98.75	98.75	17.64	56.7342
1131	0.858	0.616672	97.9167	97.9167	18.595	58.6777
1141	0.85	0.63811	98.3871	98.3871	15.9574	63.2388
1151	0.883	0.700727	99.4723	99.4723	6.2691	57.9511

Table C.7: aton_hallway

Detection and Discrimination rates calculated for both default coneR1 (Original) and coneR1' (Adaptive).

frame	coneR1*	coneR1'	Original η	Adaptive η	Original ξ	Adaptive ξ
25	0.627	0.459744	91.8856	91.4769	64.1346	74.6609
151	0.712	0.434228	99.6218	99.5083	69.3347	78.6133
164	0.81	0.538867	97.5408	97.4856	55.5124	71.1619
175	0.516	0.391069	87.1708	82.9169	63.6149	67.8378
194	0.758	0.586353	99.3337	99.2945	76.1484	83.7938
251	0.833	0.664601	82.2111	81.3065	81.7981	86.5144
275	0.747	0.690587	98.7539	97.5078	78.8321	88.0779
431	0.702	0.471719	99.407	99.2453	59.2399	67.6975
451	0.769	0.54227	99.3588	99.2145	80.6987	86.1682
600	0.666	0.379226	63.4615	63.4615	73.7265	75.067
621	0.707	0.478939	99.6299	98.9309	48.4927	60.5728
1101	0.743	0.48757	98.4813	98.4343	83.9228	89.4248
1151	0.731	0.554371	99.572	99.0661	83.2968	87.2946

Table C.8: aton_lab

Detection and Discrimination rates calculated for both default coneR1 (Original) and coneR1' (Adaptive).

frame	coneR1*	coneR1'	Original η	Adaptive η	Original ξ	Adaptive ξ
91	0.84	0.747661	98.2784	96.1688	44.6844	64.6179
101	0.908	0.729663	97.5334	97.5107	39.4961	63.1496
151	0.667	0.573093	95.804	95.4925	82.9254	93.3515
161	0.626	0.540102	93.4618	93.1693	80.3861	89.7572
221	0.892	0.509917	87.9733	87.9733	66.7318	70.371
231	0.76	0.771263	95.973	94.2403	61.1534	81.9075
281	0.724	0.629486	94.8925	94.1761	79.6353	90.1867
291	0.695	0.555757	97.0733	97.0551	77.8626	92.2074
301	0.656	0.561814	88.5236	88.3742	85.6973	96.1859
471	0.611	0.129561	78.898	90.1524	83.0598	58.7802
481	0.746	0.615002	97.2113	96.9035	76.6697	86.9145
561	0.755	0.670057	97.4796	96.0158	60.1613	74.2868
681	0.656	0.589291	95.7642	94.3217	62.9807	75.444
881	0.664	0.350949	82.1207	82.1207	83.7588	85.0625

REFERENCES

- [1] J. Danner, L. Wills, E. M. Ruiz, and L. W. Lerner, “Rapid precedent-aware pedestrian and car classification on constrained iot platforms,” in *Proceedings of the 14th ACM/IEEE Symposium on Embedded Systems for Real-Time Multimedia*, ACM, 2016, pp. 29–36.
- [2] C. Stauffer and W. E. L. Grimson, “Adaptive background mixture models for real-time tracking,” in *Computer Vision and Pattern Recognition, 1999. IEEE Computer Society Conference on.*, IEEE, vol. 2, 1999, pp. 246–252.
- [3] S. Apewokin, B. Valentine, L. Wills, S. Wills, and A. Gentile, “Multimodal mean adaptive backgrounding for embedded real-time video surveillance,” in *Computer Vision and Pattern Recognition, 2007. CVPR’07. IEEE Conference on*, IEEE, 2007, pp. 1–6.
- [4] S. Nadimi and B. Bhanu, “Physical models for moving shadow and object detection in video,” *IEEE transactions on pattern analysis and machine intelligence*, vol. 26, no. 8, pp. 1079–1087, 2004.
- [5] *Shadow detection*, <http://cvrr.ucsd.edu/aton/shadow/>.
- [6] A. Sanin, C. Sanderson, and B. C. Lovell, “Shadow detection: a survey and comparative evaluation of recent methods,” *Pattern recognition*, vol. 45, no. 4, pp. 1684–1695, 2012.
- [7] B. K. Mitra, R. Young, and C. Chatwin, “On shadow elimination after moving region segmentation based on different threshold selection strategies,” *Optics and Lasers in Engineering*, vol. 45, no. 11, pp. 1088–1093, 2007.
- [8] R. Cucchiara, C. Grana, M. Piccardi, and A. Prati, “Detecting moving objects, ghosts, and shadows in video streams,” *IEEE transactions on pattern analysis and machine intelligence*, vol. 25, no. 10, pp. 1337–1342, 2003.
- [9] E. Salvador, A. Cavallaro, and T. Ebrahimi, “Cast shadow segmentation using invariant color features,” *Computer vision and image understanding*, vol. 95, no. 2, pp. 238–259, 2004.
- [10] A. Cavallaro, E. Salvador, and T. Ebrahimi, “Shadow-aware object-based video processing,” *IEE Proceedings-Vision, Image and Signal Processing*, vol. 152, no. 4, pp. 398–406, 2005.

- [11] C.-T. Chen, C.-Y. Su, and W.-C. Kao, “An enhanced segmentation on vision-based shadow removal for vehicle detection,” in *Green Circuits and Systems (ICGCS), 2010 International Conference on*, IEEE, 2010, pp. 679–682.
- [12] B. Sun and S. Li, “Moving cast shadow detection of vehicle using combined color models,” in *Chinese conference on pattern recognition*, 2010, pp. 1–5.
- [13] J.-W. Hsieh, W.-F. Hu, C.-J. Chang, and Y.-S. Chen, “Shadow elimination for effective moving object detection by gaussian shadow modeling,” *Image and Vision Computing*, vol. 21, no. 6, pp. 505–516, 2003.
- [14] A. Yoneyama, C. H. Yeh, and C.-C. Kuo, “Moving cast shadow elimination for robust vehicle extraction based on 2d joint vehicle/shadow models,” in *Advanced Video and Signal Based Surveillance, 2003. Proceedings. IEEE Conference on*, IEEE, 2003, pp. 229–236.
- [15] H. Nicolas and J.-M. Pinel, “Joint moving cast shadows segmentation and light source detection in video sequences,” *Signal processing: Image communication*, vol. 21, no. 1, pp. 22–43, 2006.
- [16] L. Z. Fang, W. Y. Qiong, and Y. Z. Sheng, “A method to segment moving vehicle cast shadow based on wavelet transform,” *Pattern Recognition Letters*, vol. 29, no. 16, pp. 2182–2188, 2008.
- [17] C.-C. Chen and J. K. Aggarwal, “Human shadow removal with unknown light source,” in *Pattern Recognition (ICPR), 2010 20th International Conference on*, IEEE, 2010, pp. 2407–2410.
- [18] O. Javed, K. Shafique, and M. Shah, “A hierarchical approach to robust background subtraction using color and gradient information,” in *Motion and Video Computing, 2002. Proceedings. Workshop on*, IEEE, 2002, pp. 22–27.
- [19] Y.-L. Tian, M. Lu, and A. Hampapur, “Robust and efficient foreground analysis for real-time video surveillance,” in *Computer Vision and Pattern Recognition, 2005. CVPR 2005. IEEE Computer Society Conference on*, IEEE, vol. 1, 2005, pp. 1182–1187.
- [20] A. Leone and C. Distante, “Shadow detection for moving objects based on texture analysis,” *Pattern Recognition*, vol. 40, no. 4, pp. 1222–1233, 2007.
- [21] W. Zhang, X. Z. Fang, X. K. Yang, and Q. J. Wu, “Moving cast shadows detection using ratio edge,” *IEEE Transactions on Multimedia*, vol. 9, no. 6, pp. 1202–1214, 2007.

- [22] A.-T. Nghiem, F. Bremond, and M. Thonnat, “Shadow removal in indoor scenes,” in *Advanced Video and Signal Based Surveillance, 2008. AVSS’08. IEEE Fifth International Conference on*, IEEE, 2008, pp. 291–298.
- [23] A. Sanin, C. Sanderson, and B. C. Lovell, “Improved shadow removal for robust person tracking in surveillance scenarios,” in *Pattern Recognition (ICPR), 2010 20th International Conference on*, IEEE, 2010, pp. 141–144.
- [24] Z. Liu, K. Huang, T. Tan, and L. Wang, “Cast shadow removal combining local and global features,” in *Computer Vision and Pattern Recognition, 2007. CVPR’07. IEEE Conference on*, IEEE, 2007, pp. 1–8.
- [25] N. Martel-Brisson and A. Zaccarin, “Learning and removing cast shadows through a multidistribution approach,” *IEEE Transactions on Pattern Analysis and Machine Intelligence*, vol. 29, no. 7, 2007.
- [26] A. J. Joshi and N. P. Papanikolopoulos, “Learning to detect moving shadows in dynamic environments,” *IEEE Transactions on Pattern Analysis and Machine Intelligence*, vol. 30, no. 11, pp. 2055–2063, 2008.
- [27] J.-B. Huang and C.-S. Chen, “Moving cast shadow detection using physics-based features,” in *Computer Vision and Pattern Recognition, 2009. CVPR 2009. IEEE Conference on*, IEEE, 2009, pp. 2310–2317.
- [28] A. Prati, I. Mikic, M. M. Trivedi, and R. Cucchiara, “Detecting moving shadows: algorithms and evaluation,” *IEEE transactions on pattern analysis and machine intelligence*, vol. 25, no. 7, pp. 918–923, 2003.
- [29] J. Ferryman, *Pets’2001 second ieee international workshop on performance evaluation of tracking and surveillance*, <http://www.cvg.reading.ac.uk/PETS2001/>.
- [30] L. Sanin Sanderson, *C++ source code and groud truth for shadow detection / removal*, <http://arma.sourceforge.net/shadows/>.
- [31] *Computer vision and robotics research laboratory - ucsd*, <http://cvrr.ucsd.edu/>.
- [32] brofield, *Cross-platform c++ library providing a simple api to read and write ini-style configuration files*, <https://github.com/brofield/simpleini>.
- [33] *Opencv*, <http://opencv.org/>.

- [34] A. Sato, M. Toda, and M. Tsukada, “Foreground detection robust against cast shadows in outdoor daytime environment,” in *International Conference on Image Analysis and Processing*, Springer, 2015, pp. 653–664.
- [35] G.-b. Lee, M.-j. Lee, W.-K. Lee, J.-h. Park, and T.-H. Kim, “Shadow detection based on regions of light sources for object extraction in nighttime video,” *Sensors*, vol. 17, no. 3, p. 659, 2017.
- [36] A. R. Smith, “Color gamut transform pairs,” *ACM Siggraph Computer Graphics*, vol. 12, no. 3, pp. 12–19, 1978.
- [37] *Recommendation bt.709-6 (06/2015)*, <http://www.itu.int/rec/R-REC-BT.709-6-201506-I/en>, 2015.
- [38] *Recommendation bt.601*, <http://www.itu.int/rec/R-REC-BT.601/>, 2011.
- [39] D. R. Finley, *Hsp color model alternative to hsv (hsb) and hsl*, <http://alienryderflex.com/hsp.html>, 2006.
- [40] D. G. Lowe, “Object recognition from local scale-invariant features,” in *Computer vision, 1999. The proceedings of the seventh IEEE international conference on*, Ieee, vol. 2, 1999, pp. 1150–1157.
- [41] H. Bay, A. Ess, T. Tuytelaars, and L. Van Gool, “Speeded-up robust features (surf),” *Computer vision and image understanding*, vol. 110, no. 3, pp. 346–359, 2008.
- [42] E. Rosten and T. Drummond, “Machine learning for high-speed corner detection,” *Computer vision–ECCV 2006*, pp. 430–443, 2006.
- [43] A. Bosch, A. Zisserman, and X. Muñoz, “Scene classification using a hybrid generative/discriminative approach,” *IEEE transactions on pattern analysis and machine intelligence*, vol. 30, no. 4, pp. 712–727, 2008.
- [44] J.-M. Geusebroek, R. Van den Boomgaard, A. W. M. Smeulders, and H. Geerts, “Color invariance,” *IEEE Transactions on Pattern Analysis and Machine Intelligence*, vol. 23, no. 12, pp. 1338–1350, 2001.
- [45] J. Van de Weijer, T. Gevers, and A. D. Bagdanov, “Boosting color saliency in image feature detection,” *IEEE transactions on pattern analysis and machine intelligence*, vol. 28, no. 1, pp. 150–156, 2006.
- [46] Y. HAN and S. HIRAI, “Color filter in sift matching,”

- [47] T. Tuytelaars, K. Mikolajczyk, *et al.*, “Local invariant feature detectors: a survey,” *Foundations and trends® in computer graphics and vision*, vol. 3, no. 3, pp. 177–280, 2008.
- [48] A. E. Abdel-Hakim and A. A. Farag, “Csift: a sift descriptor with color invariant characteristics,” in *Computer Vision and Pattern Recognition, 2006 IEEE Computer Society Conference on*, IEEE, vol. 2, 2006, pp. 1978–1983.
- [49] M. R. Bales, D. Forsthöefel, B. Valentine, D ScottWills, and L. M. Wills, “Bigbackground-based illumination compensation for surveillance video,” *Journal on Image and Video Processing*, vol. 2011, p. 8, 2011.